Title
In-situ Analysis of Zinc Electrodeposition within an Ionic Liquid Electrolyte

Author
Keist, Jayme

Publication Date
2013

In-situ Analysis of Zinc Electrodeposition within an Ionic Liquid Electrolyte

By

Jayme Scot Keist

A dissertation submitted in partial satisfaction of the

requirements for the degree of

Doctor of Philosophy

in

Engineering – Materials Science and Engineering

in the

Graduate Division

of the

University of California, Berkeley

Committee in charge:

Professor James W. Evans, Chair
Professor Paul K. Wright
Professor Fiona M. Doyle

Spring 2013

Auspices

Portions of this work were performed under the auspices of the U.S. Department of Energy by Lawrence Livermore National Laboratory under Contract DE-AC52-07NA27344. This project was supported by Lab directed Research and Development Grant 12-LW-030.

Abstract

In-situ Analysis of Zinc Electrodeposition within an Ionic Liquid Electrolyte

by

Jayme Scot Keist

Doctor of Philosophy in Materials Science and Engineering

University of California, Berkeley

Professor James W. Evans, Chair

Ionic liquids have received considerable attention as an alternative electrolyte for rechargeable battery systems. The goal of this investigation is to develop an understanding on the electrodeposition behavior of zinc within ionic liquid electrolytes and determine whether the unique properties of ionic liquids may allow for enhanced cyclability of the zinc electrode for rechargeable battery systems.

Three different analysis techniques are employed for the investigation of the zinc deposition behavior within an imidazolium based ionic liquid electrolyte. First, the electrochemical behavior of the electrodeposition behavior is analyzed by cyclic voltammetry and potential step methods. Second, in-situ atomic force microscopy (AFM) is conducted to investigate the morphological evolution of zinc during electrodeposition. Finally, in-situ ultra-small-angle X-ray scattering (USAXS) is conducted during the electrodeposition of zinc to understand how the electrode surface evolves during electrodeposition and help confirm the results obtained from the in-situ AFM analysis.

The ionic liquid electrolyte chosen for the investigation of zinc electrodeposition is an imidazolium based system consisting of zinc trifluoromethanesulfonate ($Zn(OTf)_2$) dissolved within 1-butyl-3-methyl-imidazolium trifluoromethanesulfonate (BMIm OTf), and electrodeposition analysis is conducted on a Pt disk electrode. The behavior of Zn/Zn(II) within the ionic liquid electrolyte is analyzed at various deposition overpotentials, $Zn(OTf)_2$ concentrations, and temperatures.

Three distinct morphological behaviors are observed during the in-situ AFM analysis: growth of boulder like morphology, growth dominated by favorably oriented grains, and the formation of surface instabilities that manifested as agglomerate islands. The electrodeposition growth of Zn dominated by favorably oriented grains obtains a steady state where the surface roughness remained constant despite continued growth. The in-situ USAXS analysis confirms the results observed by the in-situ AFM analysis. In addition, the USAXS data shows that the zinc deposition

behavior is hierarchical whereby the main scattering entities exhibited a sub-structure that remains constant in size with continued deposition.

The results of this research indicate that zinc deposition within an ionic liquid electrolyte can obtain a compact and dense morphology. Furthermore, the morphology can evolve under a steady state condition under certain deposition parameters identified by this research. The improved deposition morphology of zinc within ionic liquid electrolytes may help improve the cycling performance of the zinc electrode and help make zinc based rechargeable batteries a viable alternative for energy storage applications.

Acknowledgements

My stay at the University of California, Berkeley, was not only an academic experience but also a personal journey that has taught me many lessons and helped me grow intellectually as well as personally. I would like to thank people that were around me for teaching, mentoring, and guiding me in the right direction during this time of my life.

First, I would like to thank my mother for always being there and helping me out throughout my various academic, professional and personal endeavors. I would also like to thank my father who inspired me to believe that I can follow any path that I chose for my life's journey. I especially would like to thank my wife, Nasim, for her love and understanding that she gave to me throughout my academic pursuit. I would also like to thank my son, Faraz, who keeps reminding me of what are the truly important matters in life.

I would like to extend my appreciation to my advisor, Prof. James W. Evans, for allowing me to pursue my research in the direction that I chose. I would also like to thank him for guiding me in the right direction along my research path. I would like to thank my co-advisor, Prof. Paul K. Wright, for providing every possible resource needed for my research and for his guidance.

I would like to thank Dr. Christine Orme for being my scientific mentor and hosting me at Lawrence Livermore National Laboratories within the Lawrence Scholar Program. I would also like to thank her for teaching me how to become a better scientific researcher and working with Dr. Christine Orme gave me invaluable experience building a strong foundation for my future scientific pursuits.

I would like to thank the research staff that helped me throughout my research at Lawrence Livermore National Laboratory. Especially, I would like to thank Dr. Bassem El-Dasher and Sharron Torres for all their help with my investigation with the ultra-small-angle X-ray spectroscopy (USAXS).

I would like to thank the research staff of ChemMat CARS at the Advanced Photon Source at Argonne National Laboratories for helping me out with my research. I would especially like to thank Dr. Jan Ilavsky for his sponsorship and for his invaluable advice on analyzing the USAXS data.

My stay at the University of California, Berkeley, was a special experience because of many wonderful friends and collogues. I would like to thank my fellow group members for being there for me when I needed help with my research or coursework. I would like to thank Dr. Christine Ho for helping me out in the beginning of my research and for teaching me the basics of electrochemistry. I would also like to thank Zuoqian Wang and Rich Winslow for their help throughout my research and for the insight they gave me about working with ionic liquids. In addition, I would also like to thank all the students within the Printer Group for making the day-to-day research and the group meetings enjoyable.

I would like to finally thank the staff in the Materials Science Department for their support and particularly Dr. Chris Kumai for all his help in making the lab research work as safe as possible.

Table of Contents

List of Figures

List of Tables

1. Introduction

Reliable energy storage is becoming more important as we transition from fossil fuels to renewable energy sources. Chemical energy storage, e.g. rechargeable batteries, is considered as an ideal solution for our future energy storage needs [1, 2]. This technology, however, is not currently used to store and provide electrical energy at a scale large enough to support an electrical grid. In order to provide energy storage at larger scales, further development is needed to increase the cycle life and reduce the costs for chemical energy storage systems [3]. The goal of this research is to investigate the deposition and dissolution behavior of zinc as a model system for metal electrodes in rechargeable battery systems. This research aims to contribute to the larger predictive structure-property model for metal electrodes in rechargeable battery systems.

A battery is an electrochemical storage device where the electrical energy is stored in chemical bonds. An electrochemical cell of the battery consists of two electrodes connected in series by an ionically conductive electrolyte. When a battery discharges its stored energy, the metal of the negative electrode oxidizes releasing electrons. To restore the power in a rechargeable battery, the reactions at the electrodes are reversed by applying an external current leading to reduction at the negative electrode. As a result, the metal electrode in a rechargeable battery can be considered as cycling between crystal growth (during charging) and dissolution (during discharging).

Zinc is an attractive material for energy storage since it is energy dense (both gravimetrically and volumetrically), inexpensive, non-toxic and recyclable. Zinc based energy storage has already proven to exhibit high cyclability in excess of 1000 cycles in rechargeable zinc-flow batteries [4, 5] and has exhibited high energy densities in primary zinc-air batteries [5, 6]. Zinc based rechargeable batteries without a flowing electrolyte, however, currently can only achieve around 200 cycles prior to failure [7].

The zinc electrode is typically the limiting electrode in rechargeable systems due to its propensity to form detrimental morphologies such as dendrites, nodules, and filaments. During electrodeposition, detrimental morphologies can grow and penetrate through the electrolyte/separator region and short out the cell causing the battery to fail. Furthermore, such morphologies are fragile and can break off from the electrode during dissolution, effectively removing active material from the battery system. Therefore, it is essential to prevent the formation of these detrimental morphologies to assure that the zinc electrode can undergo multiple charge/discharge cycles.

Examples showing various dendritic zinc structures that were observed after electrodeposition are shown in Figure 1.1. Figures 1.1 (a) and (b) show SEM images of zinc dendritic structures after deposition within an alkaline electrolyte of 8 molar potassium hydroxide (KOH) and Figures 1.1 (c) and (d) show zinc dendritic structures observed after deposition within an ionic liquid based electrolyte. The morphology of the dendritic structures shown in Figures 1.1 (a) and (b) are the type that can grow and penetrate through the electrolyte/separator region resulting in shorting out the electrochemical cell. Figures 1.1 (c) and (d) show fragile dendritic structures. These fragile dendritic structures may not be able to penetrate a separator, but they may break off from the electrode during dissolution (during discharging of the battery) thus reducing the amount of active material within the cell. An example of how these fragile morphologies can break off from the electrode during dissolution is shown in Figure 1.2.

This work proposes to investigate the deposition and dissolution of the zinc electrode within an ionic liquid electrolyte. The aim of this investigation is to examine the crystal growth behavior of zinc within an ionic liquid electrolyte system and to learn how to avoid the formation of detrimental morphologies during electrodeposition.

This investigation is focused on in-situ analysis of an electrochemical cell to directly observe the zinc deposition behavior at various length scales during electrodeposition within an ionic liquid electrolyte. Electrochemical analysis by itself lacks the ability to directly observe the morphological evolution of the zinc deposition. To directly observe the morphological behavior of zinc during deposition, in-situ observations were conducted by atomic force microscopy (AFM) and ultra-small-angle X-ray scattering (USAXS). Combining the morphological behavior of Zn obtained with the AFM and USAXS analyses to the electrochemical behavior observed for the system allowed for a greater understanding of the deposition behavior of zinc.

This dissertation is organized as follows. First, the background of the zinc electrode and its behavior is given within Chapter 2. In addition, this chapter introduces ionic liquid electrolytes and discusses observations made by other investigations on the metal deposition behavior within ionic liquid electrolytes. Chapter 3 presents the electrochemical behavior of the ionic liquid electrolyte used for the in-situ analysis of this work. The morphological behavior of zinc as imaged by AFM is presented in Chapter 4. This chapter also discusses the statistical analysis obtained from in-situ AFM results of the electrodeposition of zinc within the ionic liquid electrolyte. Chapter 5 presents the in-situ USAXS investigation and the analysis of the scattering data. Each of the analysis techniques used in this investigation had overlapping areas of interest that are discussed in Chapter 6. Chapter 7 overviews the main conclusions obtained from this dissertation work. Finally, Chapter 8 discusses the future directions for this work.

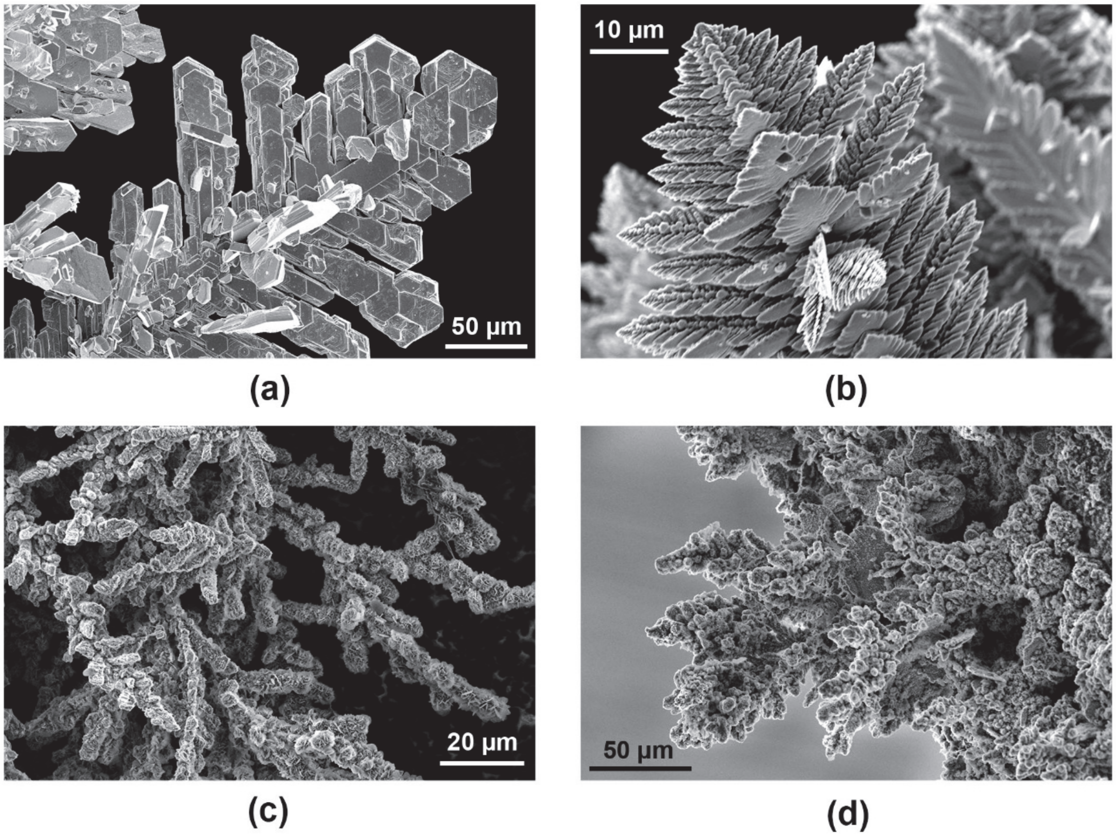

Figure 1.1. SEM images of dendritic structures observed after electrodeposition of Zn within (a) 8 M KOH with 0.3 M ZnO deposited galvanostatically at 50 mA cm^{-2}; (b) 8 M KOH with 0.3 M ZnO deposited galvanostatically at 100 mA cm^{-2}; and for (c) and (d), 0.31 mol kg^{-1} Zn(II) within an imidazolium based ionic liquid deposited potentiostatically at -1000 mV versus Zn/Zn(II).

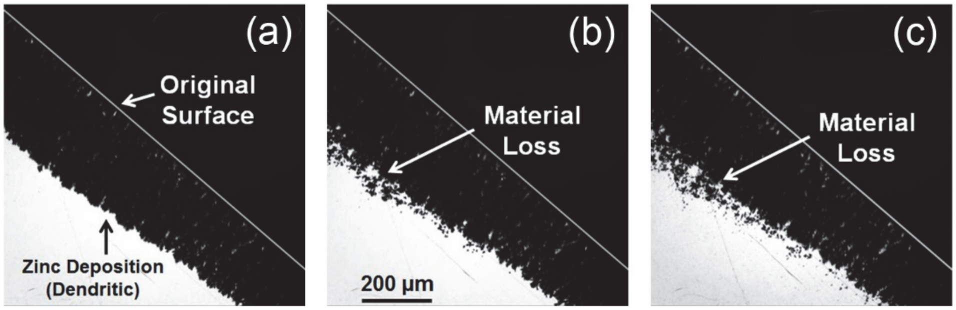

Figure 1.2. Optical micrographs showing the progression of dissolution of Zn that was electrodeposited in a dendritic morphology at -1000 mV versus Zn/Zn(II) within an imidazolium based ionic liquid. The micrographs show a side view of the electrode and the zinc deposition grew parallel to the plane of the figure. Micrographs show dissolution after (a) 0 min, (b) 15 min and (c) 30 min.

2. Electrodeposition Behavior of Zinc

The first section of this chapter overviews the zinc electrode and zinc electrodeposition behavior observed by other investigations. The second section of this chapter gives the scope of this dissertation work.

2.1. The Zinc Electrode

This section overviews the zinc electrode and discusses the deposition behavior of zinc within aqueous and ionic liquid electrolytes. The first section gives a background of the zinc electrode and discusses its current limitations. The second section discusses the electrodeposition behavior of zinc within aqueous systems. The third section details the properties of ionic liquid electrolytes. Finally the fourth section overviews what other investigations have seen with zinc deposition within ionic liquid electrolytes.

2.1.1. Formation of Detrimental Morphologies

Zinc is used in primary battery applications such as disposable batteries. Its use in secondary batteries (rechargeable), however, is limited due to cycling problems associated with the zinc electrode. The current state of the art for zinc based rechargeable batteries using an alkaline electrolyte can only achieve around 200 charge/discharge cycles prior to failure [7]. The poor cycling of the zinc electrode is the result of the formation of detrimental morphologies (e.g. dendrites), redistribution of zinc (size and shape change), and electrode passivation [5].

During discharging within a conventional aqueous alkaline electrolyte, zinc oxidizes (releasing electrons) and undergoes a reaction with hydroxides in the solution to form zincate, $Zn(OH)_4^{2-}$, by the following reaction

$$Zn(s) + 4OH^- \leftrightarrow Zn(OH)_4^{2-} + 2e^- \tag{2.1}$$

When the concentration of zincate reaches supersaturation, zinc oxide will precipitate out of solution by the following reaction

$$Zn(OH)_4^{2-} \leftrightarrow ZnO(s) + H_2O + 2OH^- \tag{2.2}$$

The redistribution of zinc from cycling results in shape change and electrode densification. This shape change and densification tends to decrease the active surface area of the electrode and thus lower its discharging capacity. This redistribution is intensified by the fast diffusing zincate that allows the zinc to reduce back on the electrode at a location far from the original oxidation location [5, 8]. Although the amount of zinc redistribution and consequently capacity loss may be small for a single cycle, it leads to a significant reduction in capacity over many cycles [8].

Another problem encountered with alkaline electrolytes is electrode passivation [9, 10]. Upon discharging, the zincate concentration within the electrolyte can reach the supersaturation point resulting in the precipitation of zinc oxide. The zinc oxide typically precipitates onto the zinc electrode surface resulting in a zinc oxide layer covering the electrode surface. This zinc oxide layer significantly decreases the ionic conductivity to the electrode. Furthermore, the zinc oxide layer can grow to the point where ionic conductivity effectively stops resulting in electrode passivation.

The foremost reason for the poor cyclability of the zinc electrode is its propensity of forming detrimental structures such as dendrites during the charge cycle [5]. These morphologies can grow and penetrate through the electrolyte/separator region and short out the cell. Furthermore, the fragile nature of these detrimental morphologies may result with these morphologies breaking off from the electrode during discharging that effectively removes active material from the battery system.

Detrimental morphologies initiate from the growth interface instabilities that develop on the electrode surface during electrodeposition. These instabilities occur when the growth rate exceeds the mass transport rate of the Zn(II) that feeds the growth [11-13]. As the growth rate increases, the growth becomes more anisotropic resulting in the formation and growth of dendritic structures. Since the growth rate is directly related to the charging current density, the current density plays a crucial role in the formation of these detrimental morphologies. The higher the current density, the more likely dendritic morphologies will form.

Examples of various dendritic morphologies are shown in Figure 2.1. At very low growth rates, a spongy morphology is typically formed [13]. Faster growth rates typically result in the formation of dendritic structures. Diggle et al. observed that zinc dendritic structures were strongly dependent on growth rate. With growth rates below 3 μm per minute, termed slow growth rate (SGR), the dendritic structures exhibited a layered structure consisting of hexagonal crystals. With growth rates exceeding 67 μm per minute, termed fast growth rate (FGR), the dendritic structures exhibited a fern like morphology that were polycrystalline in nature [12].

Typically, separators are used to help improve the cyclability of the zinc electrode by physically impeding the growth of the zinc dendrites and preventing shorting out the electrochemical cell [5]. Other methods include adding additives such as bismuth that have been shown to decrease the formation of dendritic structures, but additives also can lead to lowered performance of the battery system. Zinc flow batteries have demonstrated the ability of cycling the zinc electrode over a thousand cycles [4, 14]. Adding flow allows one to decrease the diffusion gradients and thus inhibit the formation of instabilities that would otherwise form in a mass transport limited system. Adding flow, however, means that the rechargeable battery system requires energy for energy storage and flow batteries are inherently a more complex system than conventional rechargeable battery systems.

To date, a commercial system has not been developed utilizing zinc for energy storage applications. The propensity of the zinc electrode to form detrimental structures such as dendrites has hampered its viability for energy storage applications. There isn't one driving force that results in dendritic structures but it appears to be related to the size of the concentration gradient that forms in front of the electrode/electrolyte interface during electrodeposition. Besides the influence of the applied potential or current, the propensity of forming zinc dendritic structures during deposition within an potassium hydroxide (KOH) aqueous electrolyte has been shown to increase at lower temperatures, higher concentration of KOH, lower Zn(II) concentrations within the electrolyte, and with no electrolyte stirring [5, 13, 15].

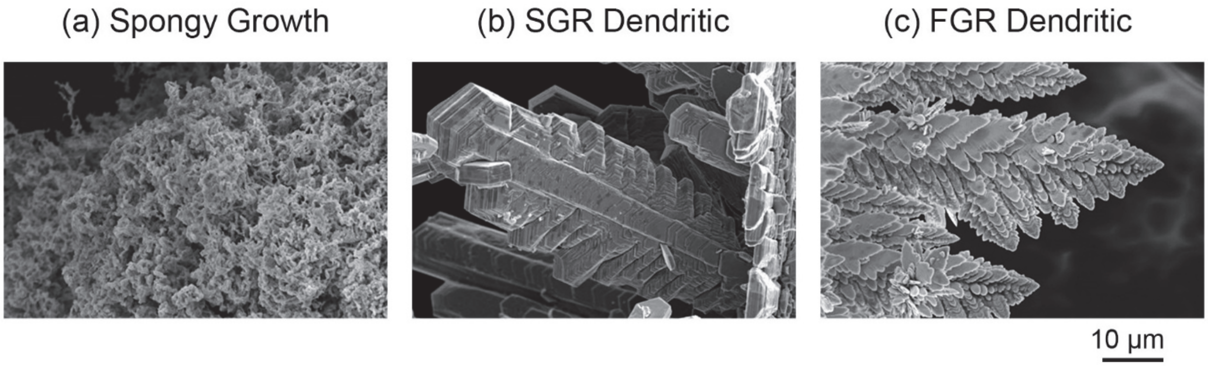

Figure 2.1. SEM images of dendritic morphologies that occur from varying degrees of growth rates from low growth rates exhibiting spongy growth (a), medium growth rates exhibiting slow growth rate (SGR) dendritic structures (b), and high growth rates exhibiting fast growth rate (FGR) dendritic structures [16].

2.2.2. Electrodeposition Behavior of Zinc within Aqueous Systems

The morphology of zinc that has been electrodeposited within aqueous electrolyte systems such as alkaline potassium hydroxide (KOH) systems typically exhibits distinct types of morphologies that are dependent on the deposition parameters such as the applied current for galvanostatic deposition or the applied potential for potentiostatic deposition. For galvanostatic deposition, Wang et al. characterized the Zn depositions in five categories as shown in Figure 2.2 consisting of heavy spongy, dendritic, boulder, layer-like, and mossy. Zinc deposition at high growth rates (exceeding 75 mA cm^{-2} within 8.5 M KOH) exhibited large boulder agglomerate structures and highly branched dendrites that are termed heavy spongy deposits. Dendritic structures are typically observed at slightly lower growth rates under an applied current of around 45 mA cm^{-2} within 8.5 M KOH. A compact boulder and a layer-like structure were obtained with an applied current between 15 to 40 mA cm^{-2} within 8.5 M KOH. Finally, mossy or filamentous growth was observed at currents lower than 10 mA cm^{-2} within 8.5 M KOH [13].

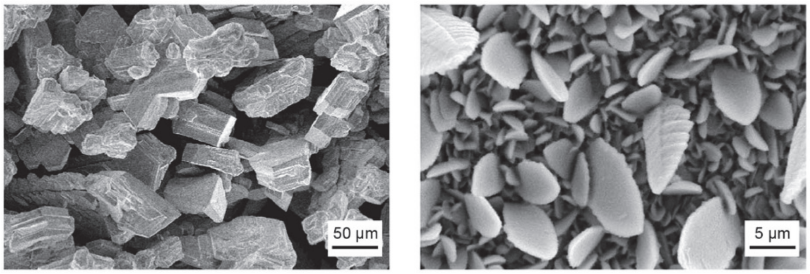
(a) Heavy Spongy

(b) Dendritic

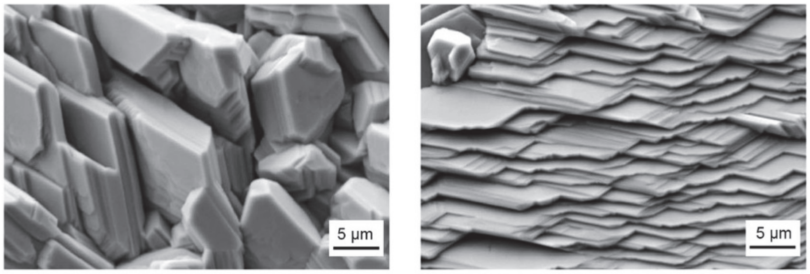
(c) Boulder

(d) Layer-like

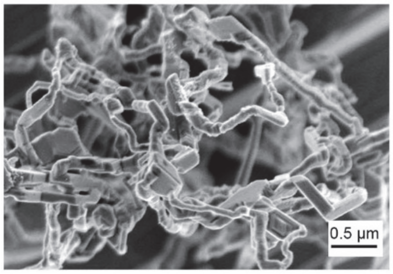
(e) Filamentous Mossy

Figure 2.2. SEM images of various Zn deposition morphologies as characterized by Want et al. SEM images were reproduced from Wang et al. [13].

Bockris et al. also observed distinct morphologies including dendritic morphologies resulting from varying applied potentials during potentiostatic zinc deposition. Mossy growth was obtained after potentiostatic deposition at an overpotential of 10 mV within 2 M KOH. A higher overpotential of 50 mV resulted in layer-like deposition. In addition, boulder-like and dendritic structures were observed at overpotentials exceeding 100 mV [17]. Finally, Lopez and Choi demonstrated that the deposition parameters can be tuned to form various types of deposition morphologies from boulder to dendritic fern like depositions by selecting the overpotential and the deposition temperature [15].

Zinc forms as a hexagonal closed packed (hcp) crystal and a schematic representation of the six crystallographic directions for zinc that are perpendicular to the basal plane, (0001), is shown in Figure 2.3. During electrodeposition, zinc tends to grow on the prism planes in the $\langle\bar{1}100\rangle$, $\langle\bar{1}\bar{1}20\rangle$, or $\langle 1\bar{2}10\rangle$ directions as shown in Figure 2.3. For deposition at low growth rates resulting in Zn morphologies similar to the layer-like morphology shown in Figure 2.2 (d), the growth of zinc is dominated by step-edge growth. The top of the zinc layers corresponds to the (0001) basal planes and growth occurs primarily in the $\langle\bar{1}100\rangle$, $\langle\bar{1}\bar{1}20\rangle$, or $\langle 1\bar{2}10\rangle$ directions on the prism planes [17]. As the system moves to dendritic growth, zinc growth also is dominated in the $\langle\bar{1}100\rangle$, $\langle\bar{1}\bar{1}20\rangle$, or $\langle 1\bar{2}10\rangle$ directions but dendritic structures also develop from the fast growing crystallographic directions as shown in the schematic in Figure 2.4 [18]. Growth of dendritic structures dominated in the $\langle\bar{1}100\rangle$, $\langle\bar{1}\bar{1}20\rangle$, or $\langle 1\bar{2}10\rangle$ directions has been observed for the deposition of zinc within alkaline solutions regardless of the substrate or initial orientation of the zinc grains [11].

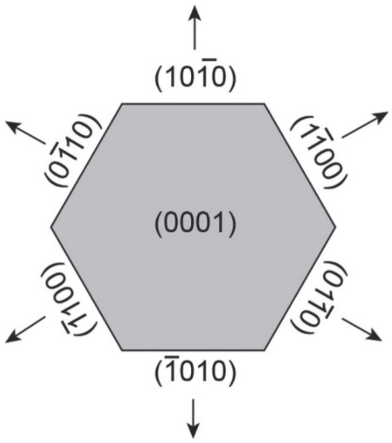

Figure 2.3. Schematic representation of the crystallographic planes for hexagonal closed packed (hcp) zinc and the arrows correspond to crystallographic directions $\langle\bar{1}100\rangle$, $\langle\bar{1}\bar{1}20\rangle$, and $\langle 1\bar{2}10\rangle$.

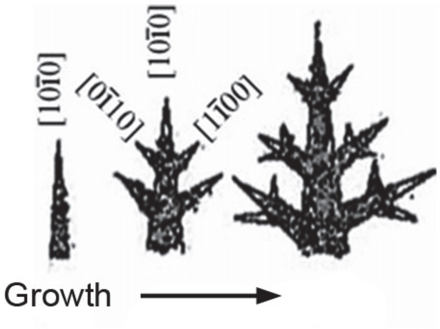

Figure 2.4. Schematic representation of development of zinc dendritic structure from a single zinc crystal from the growth in the fast growing directions. Reproduced from Pal et al. [18].

2.2.3. Ionic Liquid Electrolyte Systems

The term ‘ionic liquids’ is used for liquid substances that consist of cations and anions at temperatures below 100 °C [19]. A subset of ionic liquids termed ‘room temperature ionic liquids’ is given to ionic liquids that remain liquid at room temperature [19]. There are two main reasons why ionic liquids remain liquid down to room temperatures. First, the coordination between the cations and the anions is low and this coordination impedes the ability of the cations and anions to pack together efficiently. Second, the ionic liquid forms a quasi-lattice of ion pairs, but the lattice energy is low allowing for the ionic liquid to remain liquid at low temperatures [19, 20].

Ionic liquids are considered as attractive materials for use as battery electrolytes [21]. Unlike conventional aqueous electrolytes, typically consisting of a solution of salt within a solvent, ionic liquids are made entirely of ions. The cation largely controls the physical properties of the ionic liquid where its structure and size influences the viscosity and the ionic conductivity. Cations are also adsorbed on the cathode surface and electrostatically repulsed from the anode surface and therefore determine the structure of the double layer. Anions affect the stability and the chemical reactivity of the ionic liquid (Abbott 2006).

Ionic liquids have two key advantages over aqueous electrolytes. First, they have a wider electrochemical stability window of up to 4.2 V than aqueous based electrolytes that typically exhibit a stability window of 1.2 V [21]. Second, ionic liquids are thermally stable at elevated temperatures of up to 300°C [21]. Aqueous electrolytes, in contrast, are only stable below 100°C at atmospheric pressure and precludes their use in high temperature applications. The unique properties of ionic liquids open up new areas of investigation in electrochemical research that could not be reached using aqueous electrolytes.

Unfortunately, many ionic liquids are extremely sensitive to water and even small amounts of water can impact their performance [22]. It is important to limit the exposure of ionic liquid systems to moisture including limiting or its exposure to the natural humidity from [23]. Therefore, research and development of ionic liquid systems typically is conducted within controlled atmospheres.

2.2.4. Electrodeposition Behavior of Metals within Ionic Liquid Systems

Recently there has been intense study of metal deposition from ionic liquid electrolyte systems. The wide temperature range and low vapor pressure of ionic liquids allows for elevated temperature deposition of metals where deposition behavior can be enhanced such as nucleation, surface diffusion, and crystallization. To date, however, little is known about the nucleation and growth mechanisms for metal deposition within an ionic liquid electrolyte [24].

Imidazolium based cations have received a lot of interest in metal deposition due to their low viscosity and high conductivity. Interest includes utilizing ionic liquid electrolyte systems for energy storage applications. Recently, Ho et al. demonstrated that a zinc/manganese dioxide rechargeable battery with a gel electrolyte utilizing an imidazolium based ionic liquid was able to achieve over 70 cycles while maintaining a discharge capacity of nearly 1 mAh cm^{-2} [25].

Metal ions diffuse much more slowly in ionic liquid systems than in aqueous systems. This lower diffusion would be expected to increase the propensity of forming dendritic structures since the system will exhibit steep diffusion gradients during electrodeposition [26]. Ionic liquid systems, however, have exhibited the ability to electrodeposit metals with deposition morphologies that are dense and exhibit minimal dendritic morphologies. A few investigations are highlighted here: An investigation by Gou et al. showed that a dense, compact deposition of nickel can be obtained within an imidazolium based ionic liquid electrolyte [27]. With the use of additives that included acetonitrile and ethylene, Abbot et al. demonstrated the ability to obtain a dense and compact deposition of zinc within a deep eutectic based ionic liquid [26]. Finally, within an imidazolium based ionic liquid, Ispas et al. demonstrated the ability to obtain a dense compact deposit of silver after electrodeposition [28].

It is not fully known why ionic systems can obtain dense and compact electrodeposition morphologies, but it is hypothesized that the large size of the cations changes the nature of the double layer that forms on the electrode surface. This change in the nature of the double layer may impact the deposition behavior of the metal ions resulting in a more uniform deposition [26].

2.2. Scope of Dissertation

Ionic liquid electrolytes can offer key advantages over traditional alkaline based electrolytes for zinc based energy storage applications. Utilizing ionic liquid electrolytes can eliminate electrode passivation since OH^- is not present within the reaction. Furthermore, the double layer that forms during electrodeposition within ionic liquid systems may allow metal ions to form dense and compact morphologies that would be ideal for energy storage applications [26]. The deposition behavior of zinc within ionic liquids, however, has not fully been investigated. Therefore, it is important to understand the deposition behavior of zinc and investigate how deposition parameters influence the deposition morphology. The aim of this investigation is to understand the deposition behavior of zinc within an ionic liquid electrolyte system to further develop a better predictive structure-property relationship of metal deposition within ionic liquid systems.

The ionic liquid system chosen for this study was an imidazolium based ionic liquid electrolyte consisting of zinc trifluoromethanesulfonate, ($Zn(OTf)_2$, dissolved within an 1-butyl-3-methyl-imidazolium trifluoromethanesulfonate, BMIm OTf. The chemical structure of BMIm OTf is shown in Figure 2.5. This system was chosen since it has exhibited excellent cyclability as an electrolyte for a printed battery [25]. Imidazolium based ionic liquids also exhibit good ionic conductivity and a wide electrochemical stability window [21].

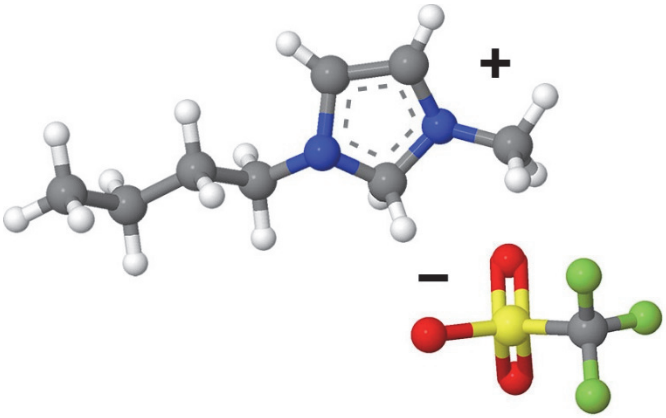

Figure 2.5. Chemical structure of 1-butyl-3-methyl-imidazolium trifluoromethanesulfonate (BMIm OTf). Structure created using Jmol (software version 13.0.15).

Various factors are known to influence the deposition behavior of zinc in alkaline electrolytes. These factors include current density, potential, ionic concentration, concentration gradients, electrolyte viscosity, ionic diffusion, temperature, and electrolyte convection [11-13]. This project investigated the influence of following factors on the electrodeposition behavior of zinc in an ionic liquid electrolyte:

- Applied potential - Controlled by the potentiostat
- Zinc ionic concentration - The initial ionic concentration is determined by the addition of zinc salts to the ionic liquid electrolyte.
- Temperature – Controlled by a resistance heater embedded within the electrochemical cell

Since the metal electrode of the battery can be viewed as cycling between crystal growth and dissolution, it is ideal to directly observe the charge/discharge behavior and the resulting crystal microstructure in an in-situ cell structure. This investigation coupled two in-situ analysis techniques that allowed for direct analysis of the zinc morphology during electrodeposition. The evolution of the zinc deposition morphology was analyzed by in-situ atomic force microscopy (AFM). The observations obtained by in-situ AFM were verified by in-situ ultra-small-angle X-ray scattering (USAXS). The USAXS allowed for analysis of a large electrode area without possible convolution and electrical shielding that might be present with the AFM analysis. Along with the electrochemical behavior measured for the system, the in-situ analysis techniques allowed for a better understanding of the zinc morphological evolution during electrodeposition within ionic liquid systems.

The objectives of this study included developing an understanding of the morphological behavior of zinc within ionic liquid electrolytes and comparing/contrasting the morphological behavior observed to that observed within aqueous systems. In addition, an objective was to determine how and why surface instabilities develop during electrodeposition within an ionic liquid electrolyte. Finally, an objective was to determine the optimum deposition parameters that allowed for electrodeposition of zinc as a dense and uniform film ideal for energy storage applications.

3. Electrochemical Behavior of Zn/Zn(II) within an Imidazolium Based Ionic Liquid

This chapter focuses on the electrochemical behavior of Zn/Zn(II) within the zinc trifluoromethanesulfonate ($Zn(OTf)_2$) / 1-butyl-3-methyl-imidazolium trifluoromethanesulfonate (BMIm OTf) ionic liquid electrolyte system. The first part of this chapter overviews the electrochemical methods of cyclic voltammetry (CV) and chronoamperometry and discusses how these techniques were used to analyze the diffusion behavior of Zn(II) and the deposition behavior of Zn. The experimental procedure is overviewed in section 3.2. Section 3.3 gives the results from the electrochemical analysis. This section also discusses the influence of the zinc salt concentration, temperature, and the applied voltage on the resulting behavior of Zn/Zn(II) within the $Zn(OTf)_2$/BMIm OTf ionic liquid electrolyte system. The final section of this chapter overviews the main conclusions from this electrochemical investigation.

3.1. Electrochemical Methods

This section overviews the electrochemical techniques used to analyze the behavior of the $Zn(OTf)_2$/BMIm OTf system. The electrochemical techniques used in this investigation included cyclic voltammetry and chronoamperometry. From these techniques, parameters measured included the diffusion coefficient, degree of irreversibility, and the nucleation behavior.

3.1.1. Cyclic Voltammetry

Cyclic voltammetry (CV) is an electrochemical technique where the current is measured while the applied potential to the cell is linearly swept at a constant rate between two set voltage limits. A cyclic voltammetry (CV) analysis can give preliminary information on the oxidation and reduction reactions for an electrochemical system. The CV technique can also be used to determine if the reactions are reversible or irreversible, whether passivation occurs, and the stability of the electrolyte.

For a reversible system undergoing a CV, the current can be solved by using Fick's first and second laws. A reversible reaction is described as

$$O + ne^{-} \leftrightarrow R \tag{3.1}$$

Where O is the oxidized species and R is the reduced species and n is the number of electrons participating in the reaction. The relation of the current density, i, to the concentration gradient of O can be obtained using Fick's first law where

$$i = nFD_O \left(\frac{\partial C_O}{\partial z}\right)_{z=0} \tag{3.2}$$

F is the Faraday constant, D_O is the diffusion coefficient of the oxidized species, O, and z is the distance from the electrode surface. This relation assumes one-dimensional diffusion, the reaction occurs on the electrode surface and only the oxidized species, O, is undergoing reduction. Equation (3.2) is valid if other transport methods such as migration and convection are negligible and if the capacitive charging is negligible.

Assuming one-dimensional diffusion, Fick's second law relates how the concentration gradient changes with time where

$$\frac{\partial C_O}{\partial t} = D_O \frac{\partial^2 C_O}{\partial z^2} \tag{3.3}$$

Using these two relations, one can solve for the current density during a CV following the derivation given by Bard and Faulkner assuming a semi-infinite and diffusion limited system [29]. A useful relation that falls out of this derivation is the relation for the peak current density, i_p, to the scan rate, v. The peak current density for a reversible system at 25ºC is [29]

$$i_p = (2.69 \times 10^5) n^{3/2} D_O^{1/2} C_O^* v^{1/2} \tag{3.4}$$

where C_O^* denotes the bulk concentration of the oxidized species. If the system is irreversible, than the shape of the cyclic voltammogram will be altered as compared to a reversible reaction. The expression for the peak current density is similar to the reversible reaction where [29]

$$i_p = (2.99 \times 10^5) \alpha^{1/2} D_O^{1/2} C_O^* v^{1/2} \tag{3.5}$$

Note that α is the electron transfer coefficient that typically has a value of around 0.5. From equations (3.4) and (3.5) for both the reversible and the irreversible conditions, the peak current density is linearly proportional to the square root of the scan rate, v, and linearly proportional to the bulk concentration, C_O^*.

In addition, the CV analysis can be used as a quick tool to determine the reversibility of an electrochemical process. For the reversible case, the peak potential is independent of the scan rate, v. In contrast, the peak potential of an irreversible reaction shifts in the negative direction for reduction with increasing scan rates. A tenfold increase in the scan rate is predicted to yield a more negative peak potential of $30/\alpha$ mV at 25°C [29]. Therefore, a simple method of determining the reversibility of a system is by comparing the cyclic voltammograms for various scan rates and noting if the reduction peak potential becomes more negative with faster scan rates.

3.1.2. Chronoamperometry

Chronoamperometry is an electrochemical analysis where the current is measured as a function of time after the potential is stepped from one constant value to a second constant value. For example, a basic chronoamperometry analysis may involve stepping the potential from the open circuit potential to a potential where the oxidized species are reduced at a diffusion-limited rate. The current transient that results from the potential step is then monitored. From the observed current transient, one can analyze the diffusion behavior of the oxidized species and the nucleation behavior for electrodeposition.

A. Current Response Planar Electrode

Assuming one-dimensional diffusion (planar electrode in a semi-infinite system) where the reduction is occurring at the diffusion-limited rate on the electrode surface, the current transient for reduction of the oxidized species, O, can be solved using Fick's second law, where

$$\frac{\partial C_O(z,t)}{\partial t} = D_O \frac{\partial^2 C_O}{\partial z^2} \tag{3.6}$$

The diffusion limited current density, i_d, as a function of time is calculated assuming the following three boundary conditions for semi-infinite one-dimensional diffusion

I. $C_O(z,0) = C_O^*$ (3.7)

II. $\lim_{z\to\infty} C_O(z,t) = C_O^*$ (3.8)

III. $C_O(0,t) = 0 \text{ (for t} > 0)$ (3.9)

The solution for the diffusion limited current density, i_d, for a system exhibiting semi-infinite one dimensional diffusion (termed the Cottrell equation) is [29]

$$i_d(t) = \frac{nFD_O^{1/2}C_O^*}{\pi^{1/2}t^{1/2}} \tag{3.10}$$

From this solution, following a potential step, the diffusion limited current density, i_d, is expected to decrease at the rate of $t^{-1/2}$. If a system exhibits diffusion limited behavior and the concentration of the oxidized species, C_O^*, is known, then the diffusion coefficient, D_O, can be measured by a potential step analysis.

B. Current Response Disk Electrode

The electrochemical analysis conducted in this research used a disk electrode. For a disk electrode, diffusion occurs radially as well as normal to the electrode surface. Figure 3.1 shows the geometry of a disk electrode. In contrast to the planar electrode, the current density is not uniform across the electrode surface. Instead, the current density will be higher at the edge of the electrode since it is the nearest surface to the surrounding volume.

The diffusion equation for the oxidized species, O, following the disk geometry is [29]

$$\frac{\partial C_O(r,z,t)}{\partial t} = D_O\left[\frac{\partial^2 C_O(r,z,t)}{\partial r^2} + \frac{1}{r}\cdot\frac{\partial C_O(r,z,t)}{\partial r} + \frac{\partial^2 C_O(r,z,t)}{\partial z^2}\right] \tag{3.11}$$

The five boundary conditions for solving for the current response are

$$\text{I.}\quad C_O(r,z,0) = C_O^* \tag{3.12}$$

$$\text{II.}\quad \lim_{r\to\infty} C_O(r,z,t) = C_O^* \tag{3.13}$$

$$\text{III.}\quad \lim_{z\to\infty} C_O(r,z,t) = C_O^* \tag{3.14}$$

$$\text{IV.}\quad \left.\frac{\partial C_O(r,z,t)}{\partial z}\right|_{z=0} = 0 \ \ (\text{for } r > r_0) \tag{3.15}$$

$$\text{V.}\quad C_O(r,0,t) = 0 \ \ (\text{for } r \le r_0 \text{ and } t > 0) \tag{3.16}$$

An analytical solution for equation (3.11) was obtained by Aoki et al. [30] by restating the problem in terms of a dimensionless parameter, τ, where

$$\tau = \frac{4D_O t}{{r_0}^2} \tag{3.17}$$

The relation of current density to the time is

$$i = \frac{4nFD_O C_O^*}{\pi r_O} f(t) \tag{3.18}$$

For short times where $\tau < 1$,

$$f(t) = \frac{\pi^{1/2}}{2\tau^{1/2}} + \frac{\pi}{4} + 0.094\tau^{1/2} \tag{3.19}$$

And for long times where $\tau > 1$,

$$f(t) = 1 + 0.71835\tau^{-1/2} + 0.05626\tau^{-3/2} - 0.00646\tau^{-5/2} \cdots \tag{3.20}$$

As pointed out by Bard and Faulkner [29], there are three current transient regimes observed with a disk electrode. Initially, the diffusion length, described by $(D_O t)^{0.5}$, is small in relation to r_0 and the current response follows a Cottrell like relation (semi-infinite planar electrode). As the experiment continues, an intermediate regime occurs when the diffusion length grows to be comparable to r_0. In this regime, the current of the disk electrode will be slightly larger than obtained by a planar electrode as the edge effect resulting from the electrode geometry starts to strengthen. Generally, Cottrell like behavior occurs when $\tau < 0.01$ with the transition to the intermediate behavior around $\tau \approx 0.01$. For long times, the current approaches a steady state current as the diffusion length becomes large enough that the electrode starts to behave like a hemispherical electrode.

For the chronoamperometry analyses conducted in this research, the electrochemical behavior was investigated with a disk electrode. Since the parameter, τ, from equation (3.17) remained at a value less than one during the electrochemical analyses, equations (3.18) and (3.19) were used for obtaining the diffusion coefficient of Zn(II) within the ionic liquid electrolyte from the chronoamperometry analysis.

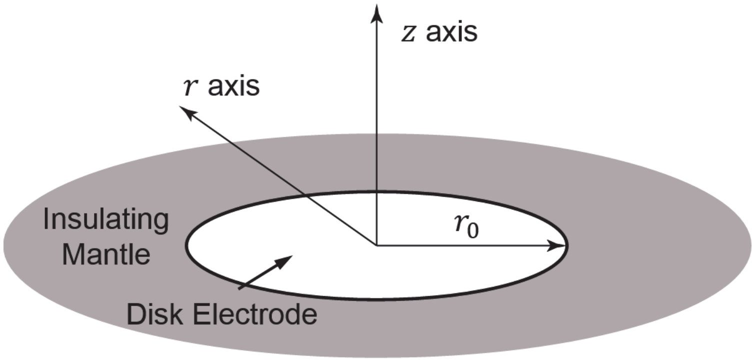

Figure 3.1. Schematic of a disk electrode within an insulating mantle.

3.1.3. Theoretical Model for Nucleation

The current transient from the potential step analysis can also reveal the nucleation behavior for the system allowing for the measurement of nucleation densities and nucleation rates. The model used for the nucleation behavior analysis of Zn from the ionic liquid electrolyte is the Scharifker model [31]. Scharifker and Hills showed that the three-dimensional nature of nucleation and diffusion can be simplified to a one-dimensional problem by noting that the spherical diffusion fields of individual nuclei eventually overlap as shown in Figure 3.2. Assuming a one-dimensional diffusion field, one can then use the Avarmi theorem to describe nucleation. This allowed for resolving two limiting regions of nucleation: instantaneous and progressive. Instantaneous nucleation is where there is an immediate activation of the available nucleation sites and the system immediately switches to growth. In contrast, nuclei continue to form during the time frame of the experiment during progressive nucleation.

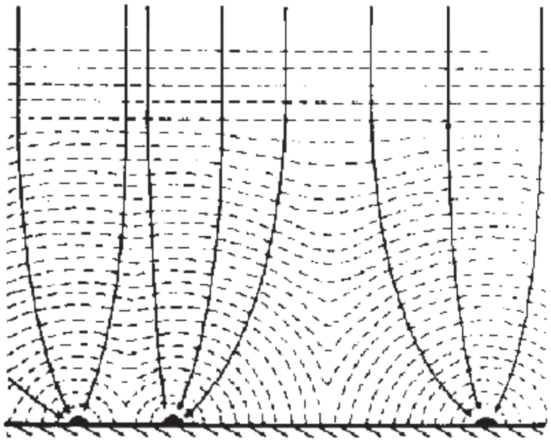

Figure 3.2 Schematic of the diffusion zones (dashed lines) for growing nuclei showing their eventual overlap. Figure reproduced from Scharifker and Hills [31].

Scharifker and Hills derived models for instantaneous and progressive nucleation. The dimensionless current transient for instantaneous nucleation is modeled as

$$\frac{I^2}{I_m^2} = \frac{1.9542}{t/t_m}\left(1 - exp\left[-1.2564\left(t/t_m\right)\right]\right)^2 \tag{3.21}$$

and the dimensionless current transient for progressive nucleation is modeled as

$$\frac{I^2}{I_m^2} = \frac{1.2254}{t/t_m}\left(1 - exp\left[-2.3367\left(t/t_m\right)^2\right]\right)^2 \tag{3.22}$$

Where I_m is the maximum current measured during the current transient and t_m is the corresponding time at I_m . The plots of equations (3.21) and (3.22) are shown in Figure 3.3. By comparing the current transient response of the chronoamperometry data, one can infer the nature of the nucleation process: instantaneous or progressive.

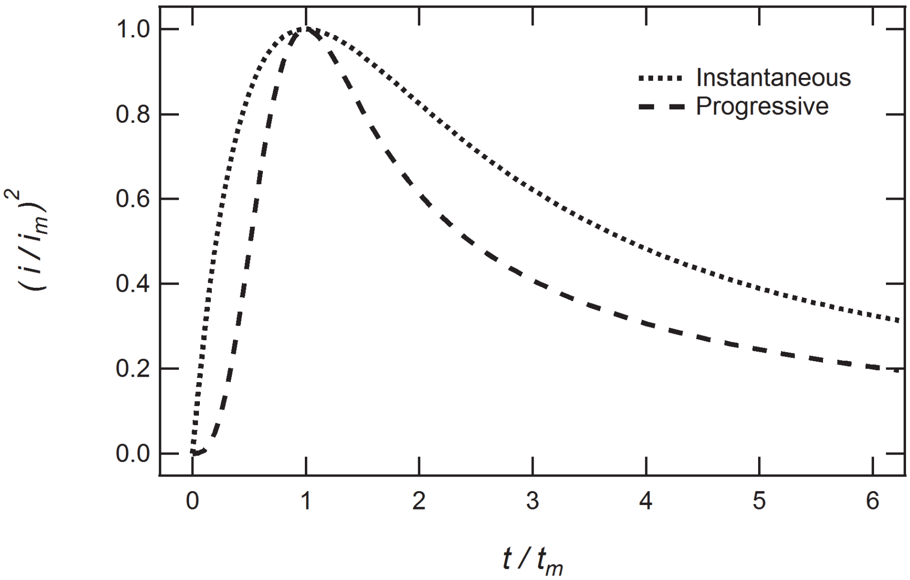

Figure 3.3. Non-dimensional I^2/I_m^2 versus t/t_m plots for instantaneous and progressive theoretical models.

The current transient for both instantaneous (3.23) and progressive nucleation (3.24) are described by [31]

$$i = \frac{zFD_O^{0.5}C_O^*}{\pi^{0.5}t^{0.5}}[1 - exp(-N\pi kD_O t)] \tag{3.23}$$

and

$$i = \frac{zFD_O^{0.5}C_O^*}{\pi^{0.5}t^{0.5}}\left[1 - exp\left(\frac{-AN_\infty \pi k' D_O t^2}{2}\right)\right] \tag{3.24}$$

where

$$k = (8\pi C_O^* M/\rho)^{0.5} \tag{3.25}$$

and

$$k' = \frac{4}{3}(8\pi C_O^* M/\rho)^{0.5} \tag{3.26}$$

N is the nucleation density and AN_∞describes the nucleation rate where A is the steady state nucleation constant per site and N_∞ is the number density of active sites. For calculating k and k', M is the molecular weight and ρ is the density of the electrochemically deposited species. Since the current transient passes through a maximum, the maximum current and corresponding time can be derived by taking the first derivative of equations (3.23) and (3.24). The corresponding equations for instantaneous nucleation are [31]

$$t_m = \frac{1.2564}{N\pi k D_O} \tag{3.27}$$

$$i_m = 0.6382\, zFD_O\sqrt{kN} \tag{3.28}$$

And for progressive nucleation are [31]

$$t_m = \sqrt{\frac{4.6733}{AN_\infty \pi k' D_O}} \tag{3.29}$$

$$i_m = 0.4615\, zFD_O^{3/4}C_O^*(k'AN_\infty)^{1/4} \tag{3.30}$$

Utilizing equations (3.23) through (3.30) allows one to calculate the nucleation density, N, for a system exhibiting instantaneous nucleation behavior or the nucleation rate, AN_∞, for a system exhibiting progressive nucleation behavior.

3.2. Electrochemical Experimental

Section 3.2.1 overviews the ionic liquid preparation procedure including the methods used to reduce the water content within the electrolyte prior to testing. The following section overviews the electrochemical cell assembly. Finally, the section 3.2.3 details the instrumentation and the testing procedure.

3.2.1. Ionic Liquid Preparation

The ionic liquid electrolyte was prepared by dissolving the desired amount of zinc trifluoromethanesulfonate ($Zn(OTf)_2$, Sigma-Aldrich, 98%) into 1-butyl-3-methyl-imidazolium trifluoromethanesulfonate (BMIm OTf, EMD Chemicals, >99%) at an elevated temperature of 80ºC. To help remove residual water from the system, the cleaning procedures outlined by Gnahm and Kolb [23] were followed. Molecular sieves of 3 Å pore size were added to the electrolyte at roughly a 1 to 3 mass ratio. In addition, the electrolyte was dried within a furnace at 100°C for 4-6 hours. The ionic liquid was then stored within a vacuum desiccator under a vacuum of 25 mm Hg for at least 24 hours prior to testing. The resulting electrolyte mixture was clear with a slight amber color.

Table 3.1 tabulates the measured concentrations for the three different $Zn(OTf)_2$ concentrations investigated. The molal concentrations analyzed in this investigation were 0.05, 0.1, and 0.34 mol

kg^{-1}. The corresponding molar concentrations the three $Zn(OTf)_2$ concentrations were 0.067, 0.13, and 0.41 mol L^{-1}. There was a large error for measuring the volume of the solution for calculating the molar concentration (+/- 0.2 mL) since the volumes measured were small (less than 20 mL) and the viscosity of the ionic liquid was high. Therefore, molal concentrations (mol kg^{-1}) are used throughout this report to designate the three different $Zn(OTf)_2$ concentrations.

Analysis of diffusion behavior for the system was conducted using the molar concentration $Zn(OTf)_2$ within BMIm OTf. As discussed in the previous paragraph, there was a large uncertainty in calculating the molar concentration. In addition, thermal expansion experienced by the ionic liquid electrolyte at elevated temperatures would effectively reduce the molar concentration at elevated temperatures. The thermal expansion measured, however, for the temperature ranges analyzed in this investigation (from 25 to 55°C) was small and well within the volume measurement error.

Table 3.1. Targeted $Zn(OTf)_2$ molal concentrations and the measured molal and molar concentrations along with the corresponding errors.

Targeted Molality (mol kg^{-1})	**Measured Molality (mol kg^{-1})**	**Error (+/-)**	**Molar Concentration (mol L^{-1})**	**Error (+/-)**
0.05	0.0512	0.001	0.067	0.0025
0.1	0.1005	0.001	0.130	0.005
0.34	0.3398	0.001	0.408	0.015

3.2.2. Electrochemical Cell

This section overviews the electrochemical cells used for this investigation. The electrochemical behavior of Zn(II) within the $Zn(OTf)_2$/BMIm OTf electrolyte was investigated within an electrochemical cell designed for in-situ electrochemical analysis by atomic force microscopy (AFM). The cyclic voltammetry of the neat BMIm OTf was conducted within a glass electrochemical cell.

A. Electrochemical Cell for Analysis of $Zn(OTf)_2$/BMIm OTf

The electrochemical experiments were conducted in an electrochemical cell (Asylum Research) that was designed for electrochemical analysis within an atomic force microscope (AFM). The same cell is used for the AFM investigation presented in Chapter 4. The electrochemical AFM cell was constructed from polyether ether ketone (PEEK) and has ports for fluid exchange and access for electrodes. The O-rings and gaskets for enclosing the cell were made from fluoro rubber of a Viton equivalent material. The electrolyte reservoir for the cell has a liquid capacity of approximately 6 milliliters. The ports to the electrolyte reservoir were used to feed through the counter and reference electrodes. A third port was used to feed dry argon gas into the electrolyte reservoir to help maintain a dry atmosphere within the electrolyte chamber.

The working electrode was a platinum disk that was sputter deposited on a 0.5 mm thick glass wafer. The diameter of the Pt disk was 1 mm with a surface area of 0.00785 cm^2. The thickness of the platinum disk was around 600 nm. The electrical connection to the platinum substrate was obtained by a 0.1 mm wide 6 mm long and 600 nm thick sputter deposited Pt leg. The total electrical resistance from the potentiostat/galvanostat to the Pt disk electrode was measured at 25 Ω. The counter and reference electrodes were Zn wire (Alfa Aesar, 99.995%) and the surface area of the counter electrode was roughly 0.50 cm^2.

Prior to testing, the Pt electrode was cleaned by submerging within 1M H_2SO_4 for 5 minutes and washed with Millipore water. Subsequently, the Pt electrode was plasma etched within a Harrick Plasma cleaner (Model PDC-32G) for 3 minutes to assure that all organics were removed from the surface. For plasma cleaning, shop air was used as the process gas for generating plasma. The entire cleaning process was repeated to assure that most contaminates were removed from the Pt substrate surface.

The electrochemical cell assembly was dried with nitrogen gas prior to adding the ionic liquid electrolyte. In addition, molecular sieves with a 3 Å pore size were added at roughly a 1 to 3 mass ratio to the ionic liquid electrolyte. The molecular sieves were added to help maintain a low water content within the ionic liquid electrolyte during testing. Figure 3.4 shows a photograph of the final cell assembly prior to adding the electrolyte. Figure 3.4 also points out the location of the reference, counter, and Pt substrate electrodes. Finally, the temperature of the system was maintained at the desired temperature during the analysis by an electrical resistance heater embedded within the electrochemical cell.

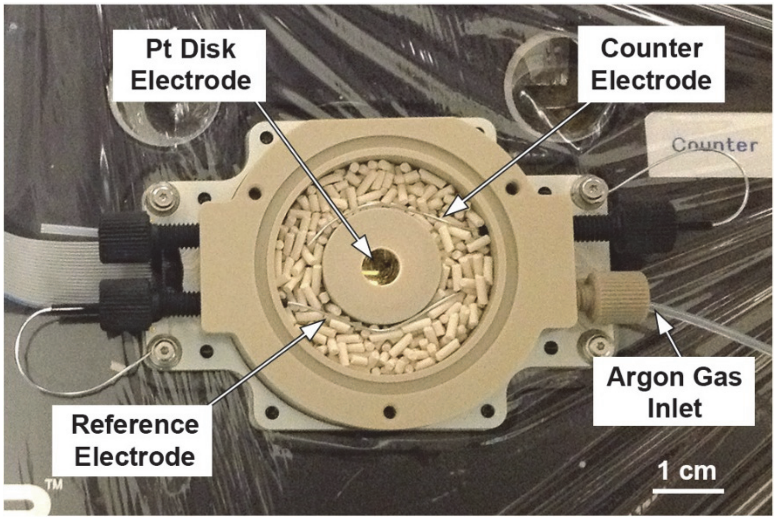

Figure 3.4. Top down view of the in-situ AFM electrochemical cell. Note that 3Å molecular sieves are shown in the electrolyte reservoir of the cell.

B. Electrochemical Cell for Cyclic Voltammetry Analysis of the Neat BMIm OTf

The cyclic voltammetry of the neat BMIm OTf was conducted within a glass flask. The flask was enclosed and dry argon gas flowed through the reservoir chamber throughout testing. The working and counter electrodes were 0.5 mm diameter Pt wire. The Pt wires were immersed within the electrolyte by 10 mm. The total surface area of the working electrode was 0.157 cm^2.

The reference electrode was a 0.5 mm diameter Zn wire (Alfa Aesar, 99.995%). The reference electrode was immersed within a 0.40 mol/L $Zn(OTf)_2$ dissolved within BMIm OTf. The solution was enclosed within a Teflon (PTFE) tube. The junction between reference electrode solution and the neat BMIm OTf was a glass frit (Porous Vycor).

3.3.3. Instrumentation and Procedure

The electrodeposition experiments were conducted using a Bio-Logic SP-300 potentiostat/galvanostat. The potentials were referenced to the Zn/Zn(II) of the reference electrode.

For the electrochemical analyses, the AFM cantilever assembly and head were positioned on top of the cell and the top gasket was closed. Dry argon gas was allowed to percolate through the cell for at least 10 minutes prior to analysis. During analysis, the atmosphere within the electrolyte chamber of the cell was periodically purged with dry argon gas to help maintain a dry atmosphere above the electrolyte. After each electrochemical experiment, the AFM cantilever assembly was removed from the cell to allow for cleaning off any films that may have attached to the working electrode surface during oxidation. Cleaning was conducted with an electrolyte soaked cotton swab. In addition, the working electrode surface was visually monitored with an optical microscope during the experiments to double check that the electrode surface was exhibiting deposition over the entire surface.

3.3. Results and Discussion

3.3.1. Cyclic Voltammetry

This section overviews the cyclic voltammetry analysis of the various zinc concentrations at various temperatures. Cyclic voltammetry tests were conducted at three $Zn(OTf)_2$ concentrations at 0.05, 0.10 and 0.34 mol kg^{-1} (0.07, 0.13, and 0.41M respectively) within the BMIm OTf ionic liquid at temperatures ranging from 25 to 55°. The cyclic voltammetry tests were run from the open circuit potential to a vertex of -800 mV versus Zn/Zn(II) and returned to the initial potential.

A. Scan Rate

Figure 3.5 shows the cyclic voltammograms of a Pt electrode in $Zn(OTf)_2$ concentration of 0.1 mol kg^{-1} for various scan rates from 5 to 50 mV s^{-1}. For the same scan rates, Figure 3.6 shows the cyclic voltammograms of a Pt electrode in $Zn(OTf)_2$ concentration of 0.3 mol kg^{-1}. The cyclic voltammogram of the neat BMIm OTf is plotted in the inset within both Figure 3.5 and Figure 3.6. The neat ionic liquid exhibited an electrochemical stability window of around 2.6 V from around -900 mV to around 1700 mV versus Zn/Zn(II). The range analyzed for the cyclic voltammetry from -800 mV to 600 mV versus Zn/Zn(II) is well within the stability range of the BMIm OTf ionic liquid. In addition, neither cathodic nor anodic peaks were observed on the cyclic voltammogram of the neat BMIm OTf that would point to the presence of water within the ionic liquid system.

The cathodic current corresponds to the reduction of Zn(II) to Zn and the anodic current is associated with the dissolution of Zn forming Zn(II). As shown in both Figure 3.5 and Figure 3.6, the potential of the cathodic peaks continued to decrease with increasing scan rates for both concentrations. For the 0.1 mol kg^{-1} concentration, cathodic peaks were observed from -520 mV versus Zn/Zn(II) at a scan rate of 5 mV s^{-1} and decreased to -680 mV at a scan rate of 50 mV s^{-1}. Similarly, the 0.34 mol kg^{-1} concentration had a cathodic peak of -630 mV at a scan rate of 5 mV s^{-1} and decreased to -770 mV at the 50 mV s^{-1} scan rate.

The separation between the cathodic and anodic peaks was measured around 0.8 to 1 V for the cyclic voltammetry scans at 25ºC for both the 0.1 and 0.34 mol kg^{-1} concentrations. The large potential difference between the cathodic and anodic peaks and the fact that the potential of the anodic peak becomes more negative with faster scan rates indicates that the system is electrochemically irreversible. Furthermore, the integrated electric charge transfer during the oxidation was 10% smaller than during reduction for the 5 mV s^{-1} CV within the 0.34 mol kg^{-1} concentration electrolyte. Within the lower concentration of 0.1 mol kg^{-1}, the charge transfer during the oxidation was 30% smaller than during reduction for the 5 mV s^{-1} CV. This suggests that either the Zn reduced during the cathodic scan could not be oxidized completely during the anodic scan or that there is a parasitic reaction occurring during the cathodic scan.

Figure 3.7 shows the peak cathodic current plotted against the scan rate speed. Generally, the data appeared to follow the square root of the scan rate as expected for a diffusion limited system following equation (3.5). From the peak cathodic data, a diffusion coefficient of 9×10^{-8} cm^2 s^{-1} Zn(II) within 0.34 mol kg^{-1} concentration at 25°C was estimated using equation (3.5). This value was obtained assuming that the electron transfer coefficient, α, was 0.5. The value obtained for the diffusion coefficient, however, should only be used as a general estimate since equation (3.5) was derived assuming a single step electron transfer process.

B. Temperature

The influence of temperature on the zinc deposition within the ionic liquid was analyzed by cyclic voltammetry. Figure 3.8 shows the effect of increasing temperature on the resulting CV's for the various $Zn(OTf)_2$ concentrations (10 mV s^{-1} scan rate). Two main effects were observed for each concentration. First, the peak current increases with increasing temperature due to the increasing diffusion. Second, the overpotential required for initial zinc deposition on the Pt electrode decreased as the temperature. This decrease in the required overpotential may be the result of the higher thermal energy to help overcome the activation energy barrier. For the 0.05 mol kg^{-1} concentration, the potential required to initiate zinc deposition was around -600 mV at 35ºC. At 55ºC, the potential required for deposition increased to around -400 mV. Similar behavior was observed for the concentrations of 0.1 mol kg^{-1} and 0.34 mol kg^{-1}. It was also observed that with higher zinc salt concentrations, the potentials required for deposition were lower for each of the temperatures analyzed. The 0.34 mol kg^{-1} concentration exhibited the lowest overpotential required for deposition with a value near -220 mV at 55ºC.

The influence of temperature and the $Zn(OTf)_2$ concentration did not appear to follow the Nernst equation. The Nernst equation predicts that the overpotential required for deposition would change by only a few millivolts for the temperature and concentration ranges analyzed in this investigation. The lowest equilibrium potential given by the Nernst equation is -798 mV versus a standard hydrogen electrode (SHE) for the 0.05 mol kg^{-1} at 55°C and the highest equilibrium potential is -772 mV versus SHE for the 0.34 mol kg^{-1} at 25°C. Instead, deposition potentials varied by hundreds of millivolts for the ranges analyzed.

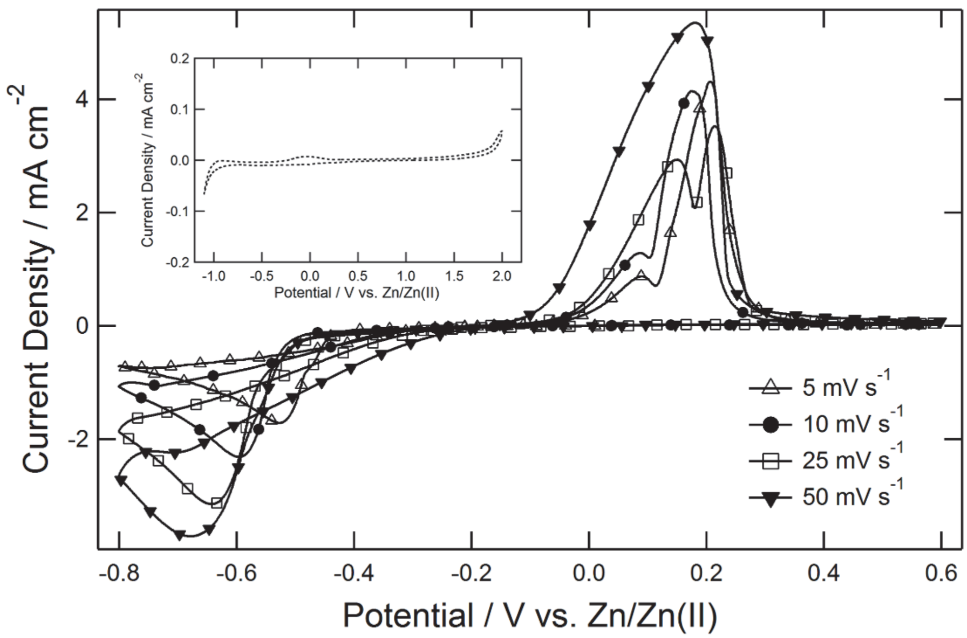

Figure 3.5. Cyclic voltammograms of a Pt electrode for $Zn(OTf)_2$/BMIm OTf concentrations of 0.1 mol kg^{-1} (0.13 M) for with various scan rates at 25ºC. Inset graph shows the cyclic voltammogram for a neat BMIm OTf at a scan rate of 10 mV s^{-1} at room temperature.

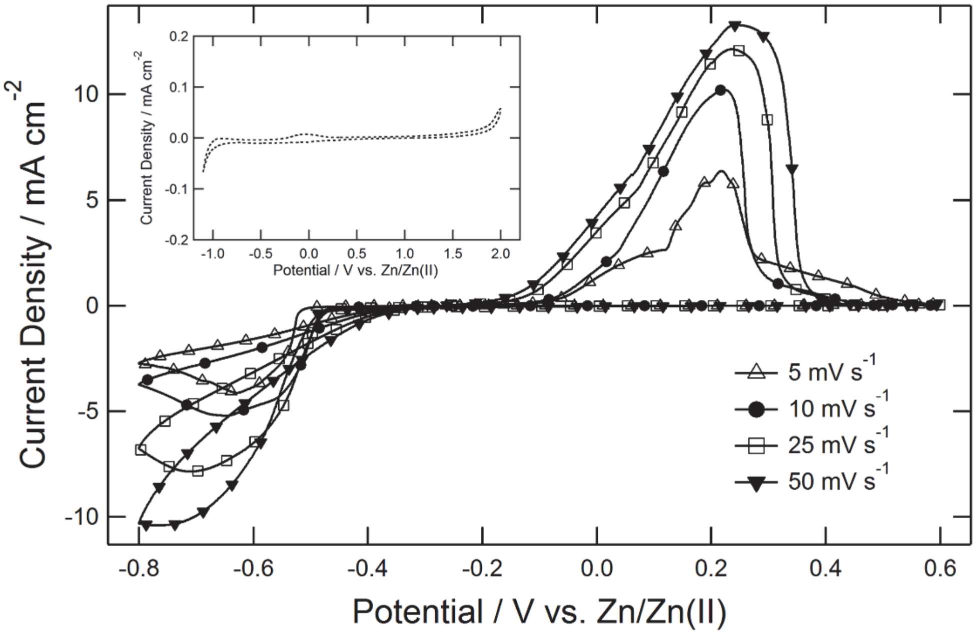

Figure 3.6. Cyclic voltammograms of a Pt electrode for $Zn(OTf)_2$/BMIm OTf concentrations of 0.3 mol kg^{-1} (0.41 M) for with various scan rates at 25ºC. Inset graph shows the cyclic voltammogram for a neat BMIm OTf at a scan rate of 10 mV s^{-1} at room temperature.

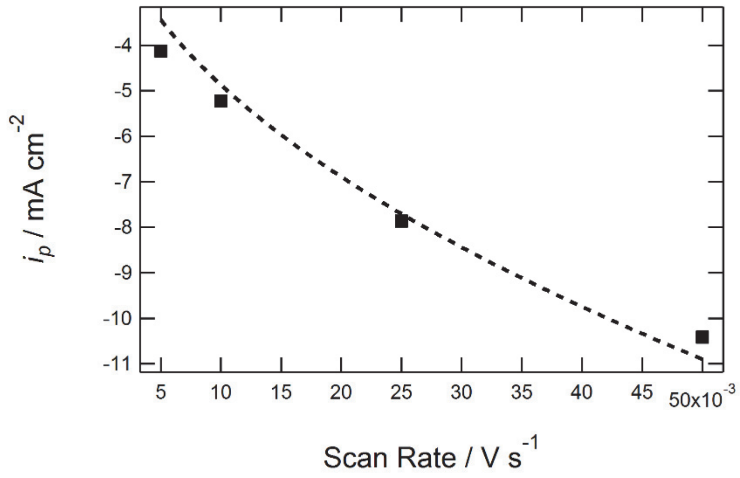

Figure 3.7. Peak cathodic current density plotted against the scan rate for 0.34 mol kg^{-1} (0.41 M) Zn(OTf)$_2$/BMIm OTf at 25ºC. The dashed line corresponds to the best fit curve following ${i_p}^{0.5}$.

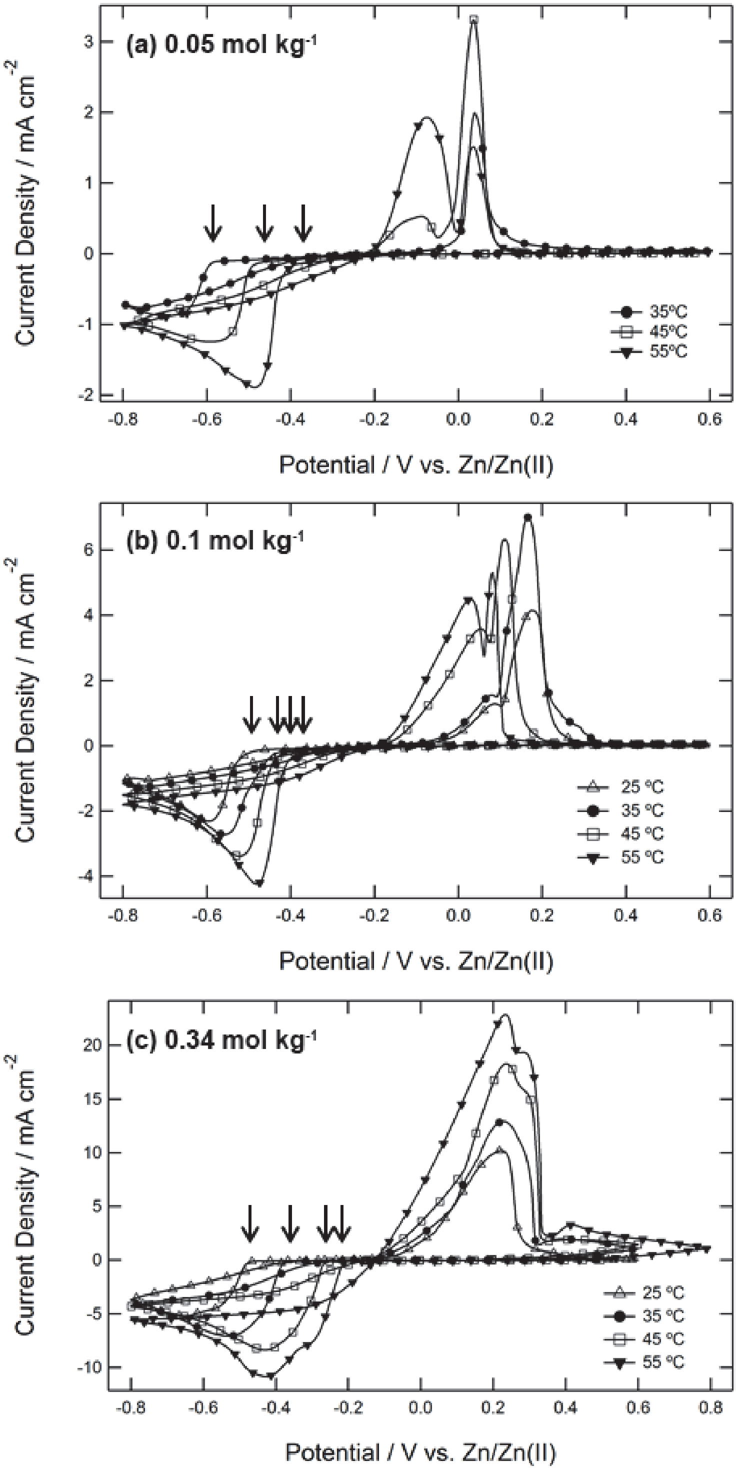

Figure 3.8. Cyclic voltammograms of a Pt electrode in Zn(OTf)$_2$ concentrations of (a) 0.05, (b) 0.1, and (c) 0.034 mol kg^{-1} at various temperatures with a scan rate of 10 mV s^{-1}. The arrows highlight the potentials at which deposition of Zn occurred on the Pt electrode.

3.3.2. Chronoamperometry Analysis

Figure 3.9 shows the chronoamperograms of a Pt electrode in $Zn(OTf)_2$ concentrations of 0.1 and 0.34 mol kg^{-1} starting at open circuit potential and undergoing various potential steps versus the Zn/Zn(II) reference. Current density peaks associated with nucleation were observed for each potential step and after the peaks the current density converged with time. The current transient observed for the 0.1 mol kg^{-1} concentration exhibited two peaks for the potentials of -500 and -550 mV versus the Zn/Zn(II) reference and suggests a two-step deposition behavior. These peaks merge into a single peak with for the potential steps of -600 and -700 mV versus the Zn/Zn(II) reference. The current transient for the 0.34 mol kg^{-1} concentration exhibited expected behavior of a diffusion limited system. The current density peaks increased in magnitude with more negative potential steps and the deposition time for the peaks decreased with more negative potential steps.

From the chronoamperograms for the concentration of 0.34 mol kg^{-1}, the kinetic behavior was analyzed by sampled-current voltammetry for the $Zn(OTf)_2$/BMIm OTf system. Figure 3.10 shows a sampled-current voltammogram for the potential step data. The sampled-current voltammogram plots the normalized current density versus the overpotential. The overpotential is defined as the difference between applied potential and the potential where no net current occurs (rest potential). The overpotential corresponding to i/i_d equal to 0.5 defines a value that is independent of the species concentration at the surface. Instead, this value defines the oxidation and reduction behavior of the system. For the $Zn(OTf)_2$/BMIm OTf system, the corresponding overpotential was around -250 mV versus Zn/Zn(II) and suggests a highly irreversible system. For comparison, a value of 0 V corresponds to a reversible system. In addition, the transition from a normalized current of 0 to unity over a wide potential range of 600 mV suggests a system with sluggish kinetics.

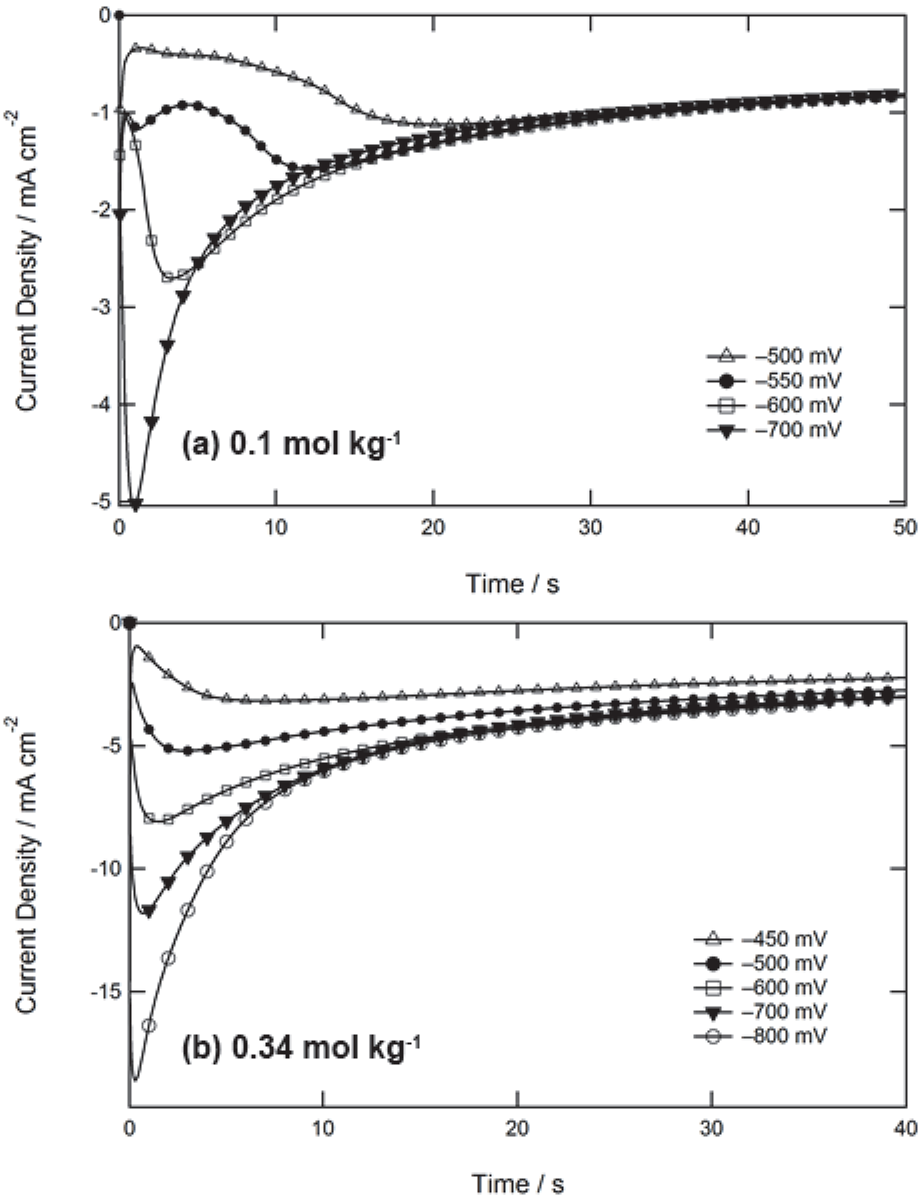

Figure 3.9. Chronoamperograms of a Pt electrode in Zn(OTf)$_2$ concentrations of (a) 0.1 mol kg^{-1} (0.13 M) and (b) 0.34 mol kg^{-1} (0.41 M) for various potential steps versus Zn/Zn(II) at 25ºC.

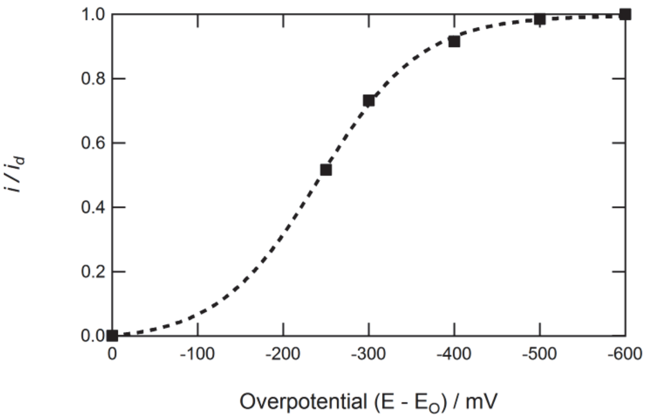

Figure 3.10. Sampled current voltammogram of the normalized current density sampled at 10 seconds versus the overpotential for the deposition of Zn on a Pt electrode in 0.34 mol kg^{-1} (0.41 M) $Zn(OTf)_2$/BMIm OTf at 25ºC. The dashed line is a best fit sinusoidal for the data points.

A. Diffusion Coefficient of Zn(II)

The diffusion coefficient of Zn(II) within the ionic liquid system was measured for each potential and concentration investigated. The diffusion coefficient, D_O, of Zn(II) within the $Zn(OTf)_2$/BMIm OTf system was obtained from a best fit curve analysis with the theoretical current-time response. For the Pt disk electrode, the theoretical current-time response for a disk electrode given in equations (3.18) and (3.19) were used for calculating the diffusion coefficient. Figure 3.11 shows the resulting chronoamperograms for various temperatures and for $Zn(OTf)_2$ concentrations of 0.05, 0.1, and 0.34 mol kg^{-1} that were used for calculating the diffusion coefficients.

Figure 3.12 shows the calculated diffusion coefficient of Zn(II) within the $Zn(OTf)_2$/BMIm OTf system plotted against the temperature for the three $Zn(OTf)_2$ concentrations. The error ranges for the data points in Figure 3.12 were calculated from the uncertainty in the actual $Zn(OTf)_2$ concentration (Refer to section 3.2.1). The calculated diffusion coefficients increased with increasing temperature. The diffusion coefficient of Zn(II) at 25ºC was estimated to be 1.5 × 10^{-7} cm^2 s^{-1} for both the $Zn(OTf)_2$ concentrations of 0.1 and 0.34 mol kg^{-1}. At 55ºC, the 0.34 mol kg^{-1} system achieved a diffusion coefficient increased to 5.3 × 10^{-7} cm^2 s^{-1}. The 0.1 and 0.05 mol kg^{-1} concentrations were slightly lower, but within the measurement error, at 4.5 × 10^{-7} cm^2 s^{-1} and 5.0 × 10^{-7} cm^2 s^{-1} respectively.

For the concentration range analyzed, it did not appear the $Zn(OTf)_2$ concentration had a significant influence on the resulting diffusion of Zn(II) within the $Zn(OTf)_2$/BMIm OTf system. The higher concentration of 0.34 mol kg^{-1} exhibited a slightly higher diffusion coefficient than the 0.1 and 0.05 mol kg^{-1} concentrations. The calculated values for the 0.34 mol kg^{-1} concentration, however, were within the error range of the 0.1 and 0.05 mol kg^{-1} concentrations.

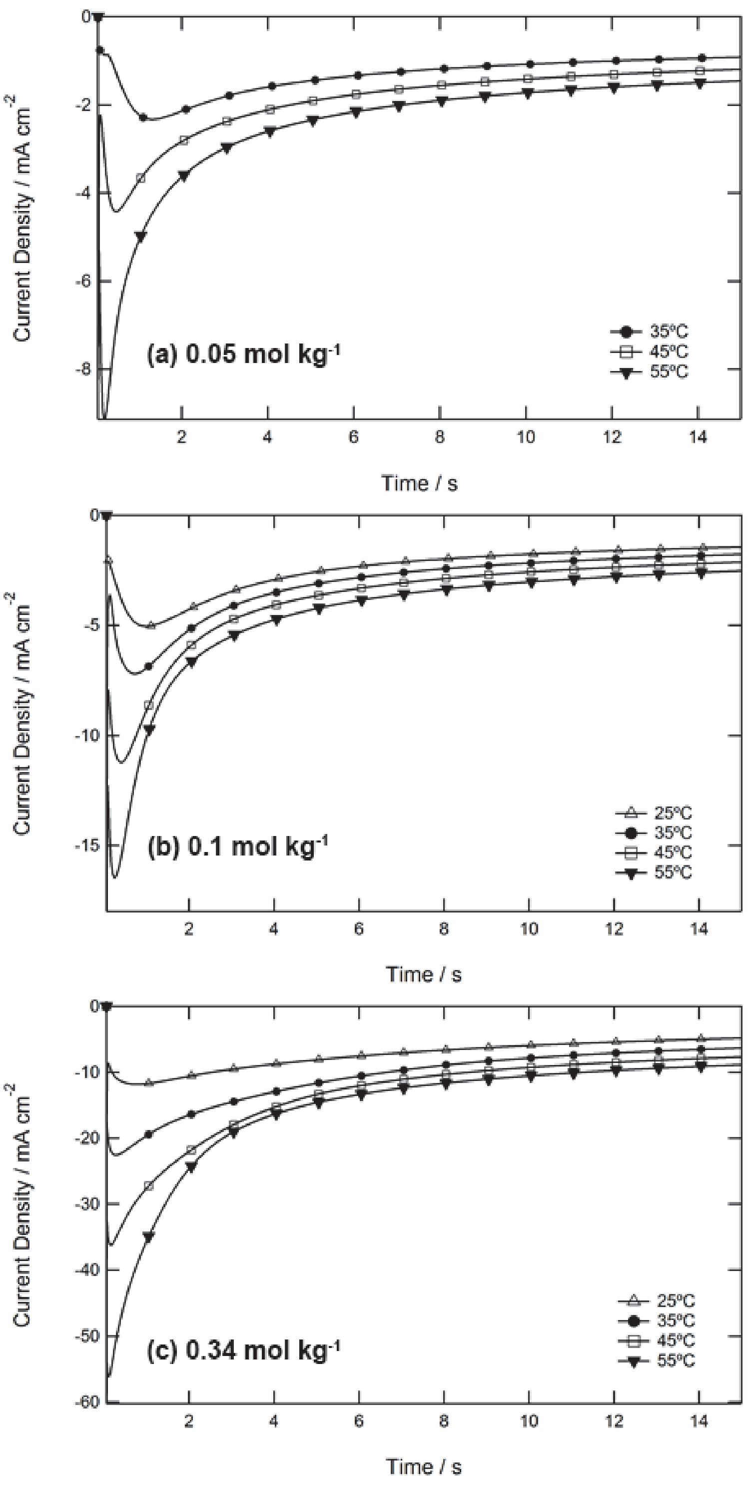

Figure 3.11. Chronoamperograms of a Pt electrode in (a) 0.05, (b) 0.1 and (c) 0.34 mol kg^{-1} (0.67, 0.13, and 0.41 M) Zn(OTf)$_2$/BMIm OTf with a potential step of -700 mV versus Zn/Zn(II) at various temperatures.

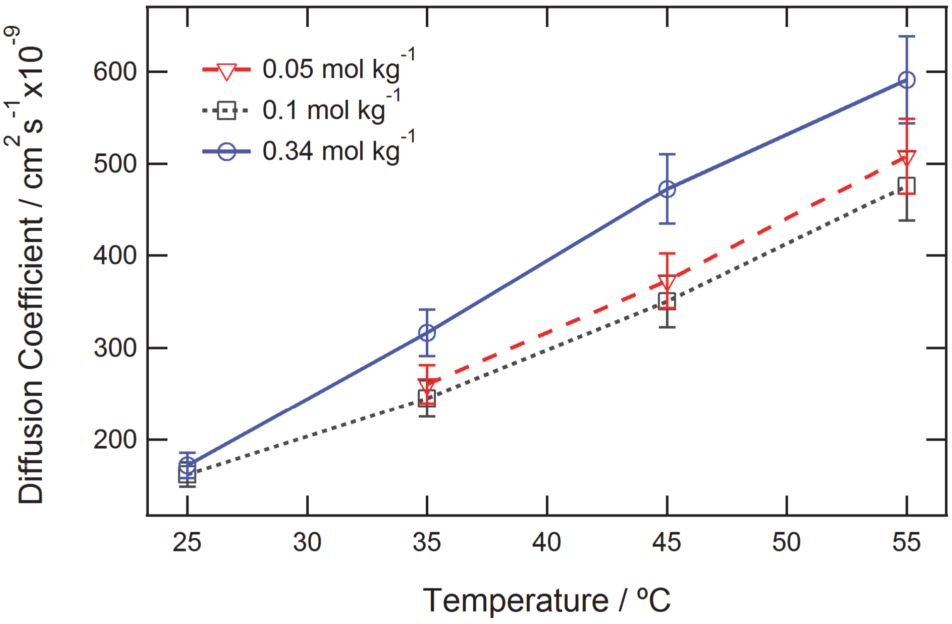

Figure 3.12. Calculated diffusion coefficients for the various $Zn(OTf)_2$ concentrations versus temperature. Error bars represent the measurement error.

The values measured for the diffusion coefficient of Zn(II) within the $Zn(OTf)_2$/BMIm OTf system were comparable to similar systems determined by other investigations. Pitner and Hussey investigated Zn deposition within chloride-1-methyl-3-ethylimidazolium chloride ionic liquid electrolyte with a Zn(II) concentration of 0.025 mol liter^{-1} and obtained a diffusion coefficient of Zn(II) of 6.7×10^{-7} cm^2 s^{-1} at 40°C [32]. By interpolation of the data obtained from this investigation, the diffusion coefficient of Zn(II) within $Zn(OTf)_2$/BMIm OTf was estimated to be 3.5×10^{-7} cm^2 s^{-1} at 40°C. Typically, the diffusion coefficients within imidazolium based ionic liquids vary from 1 to 12×10^{-7} cm^2 s^{-1} measured near room temperature [21].

The measured diffusion coefficients for Zn(II) within ionic liquid electrolytes, however, were significantly lower than measured for conventional aqueous based electrolytes that are typically on the order of 10^{-5} cm^2 s^{-1} [33]. The diffusion of Zn(II) measured within an 8.2 M KOH aqueous solution at 25°C was 4.5×10^{-6} cm^2 s^{-1} [34]. The higher diffusion coefficients in aqueous systems compared to ionic liquid systems are attributable to the greater viscosity of ionic liquid systems [35]. The room temperature dynamic viscosity of a KOH electrolyte is in the range of 22 to 36 cP [36] and BMIm based ionic liquid systems are in the range of 180 to 380 cP [21]. Note that the viscosity data for the BMIm ionic liquid systems was measured without a dissolved salt such as $Zn(OTf)_2$. Dissolving a salt within an ionic liquid system typically increases the viscosity [35] and viscosity of the $Zn(OTf)_2$/BMIm OTf could be well above the value for the neat ionic liquid system without a dissolved salt.

B. Nucleation Behavior of Zn(II) on Pt

The chronoamperometry data for the various potential steps were plotted non-dimensionally as I^2/I_m^2 versus t/t_m. These plots were then compared to the theoretical Shaifker model for instantaneous and progressive nucleation [31]. Figure 3.13 shows the resulting plots for the various potential steps for the $Zn(OTf)_2$ concentrations of 0.1 and 0.34 mol kg^{-1} at 25ºC along with the theoretical models. The dimensionless plots from the 0.1 mol kg^{-1} data appeared to be best described as a progressive nucleation system. The potential steps of -500, -600 and -700 mV showed a similar current transient that followed just above the theoretical transient for a progressive system. The -550 mV potential step fell slightly below the theoretical transient, but they may be explained by experimental error. Although the results are not given here, the 0.05 mol kg^{-1} $Zn(OTf)_2$ concentration appeared to follow the same trend as the 0.1 mol kg^{-1} concentration. In contrast, the 0.34 mol kg^{-1} data appeared to most closely follow the instantaneous theoretical model. Note that the influence of temperature was also analyzed, but the temperature did not significantly influence the current transient behavior of any of the systems analyzed.

These results suggest that there is a strong correlation between the concentrations of Zn(II) within the electrolyte to the resulting nucleation behavior of Zn on the Pt substrate. The higher concentration of 0.34 mol kg^{-1} exhibited instantaneous nucleation at each applied potential and system temperatures analyzed. On the other hand, the lower concentration levels of 0.05 and 0.1 mol kg^{-1} exhibited progressive nucleation regardless of the applied potential or temperature.

Zhu et al. analyzed the electrodeposition of Ni(II) on a Pt substrate within an amide-type ionic liquid and they observed similar nucleation behavior as was observed in this analysis for the 0.34 mol kg^{-1} data [37]. The dimensionless plots for the chronoamperometry data obtained by Zhu et al. most closely followed the theoretical plot for instantaneous nucleation. In addition, similar to the 0.34 mol kg^{-1} data presented here, their data also trended at a higher dimensionless transient of $(i/i_m)^2$ versus (t/t_m) than predicted by the instantaneous model presented by [31]. Pitner and Hussey analyzed the electrodeposition behavior of Zn within an imidazolium based ionic liquid on glassy carbon, but they determined that the nucleation behavior most closely follows progressive nucleation [32].

The discrepancy between the nucleation behaviors identified from various investigations can probably be explained by the influence of the substrate. A glassy carbon substrate, as used in the Pitner and Hussey investigation, may require a higher activation barrier to initiate nucleation resulting in progressive behavior. In contrast, a Pt substrate, as used by Zhu et al., may effectively have decreased the nucleation barrier and pushed the system to follow instantaneous behavior. Furthermore, our investigation also highlighted the importance of the Zn(II) concentration on the nucleation behavior of the system. Electrodeposition within the lower Zn(II) concentration electrolyte exhibited progressive nucleation while deposition within the higher concentration exhibited instantaneous nucleation.

The nucleation density and the nucleation rates were estimated for the potential step depositions utilizing the theoretical relation of the current density to the time for instantaneous and for progressive nucleation. The 0.34 mol kg^{-1} Zn(OTf)$_2$ concentration appeared to exhibit instantaneous nucleation for the potential steps and temperatures analyzed. The theoretical current-time relationship for instantaneous nucleation is described by equation (3.23). With the diffusion coefficient measured in the previous section, the nucleation density, N, was obtained by fitting the theoretical model of the current density to the potential step data. Figure 3.14 shows the best fit (least squares method) of the theoretical model to the potential step data conducted within 0.34 mol kg^{-1} Zn(OTf)$_2$ at 25°C.

The nucleation density plotted against the applied potential obtained from the theoretical model is shown in Figure 3.15. Figure 3.15 shows that there is an exponential relation of the calculated nucleation density obtained from the model to the applied potential. At -450 mV versus Zn/Zn(II), the nucleation density was estimated by the model to be 0.4×10^6 cm^{-2} and at -700 mV, the nucleation density was estimated to be fifteen times higher at 6.3×10^6 cm^{-2}.

For Zn electrodeposition within the 0.1 mol kg^{-1} concentration at 25°, the nucleation behavior appeared to follow the progressive nucleation model. The nucleation rate, AN_∞, was estimated by fitting the theoretical model for the current density given in equation (3.24) to the potential step data. Figure 3.16 shows the best fit (least squares method) of the theoretical model to the potential step data conducted within 0.1 mol kg^{-1} Zn(OTf)$_2$ at 25°C.

The calculated nucleation rates plotted against the applied potential obtained from the theoretical model for electrodeposition within 0.1 mol kg^{-1} Zn(OTf)$_2$ at 25°C are shown in Figure 3.17. The nucleation rate estimated from the model scaled logarithmically with the applied potential. At -500 mV versus Zn/Zn(II), the nucleation rate was estimated to be 7.7×10^4 cm^{-2} s^{-1}. By -600 mV, the estimated rate was almost two orders of magnitude higher at 3.4×10^6 cm^{-2} s^{-1}.

Although the nucleation density and nucleation rates were calculated from theoretical models, the numbers give an estimation that were compared to experimental data obtained from in-situ electrochemical atomic force microscopy analysis (EC AFM) in Chapter 6.

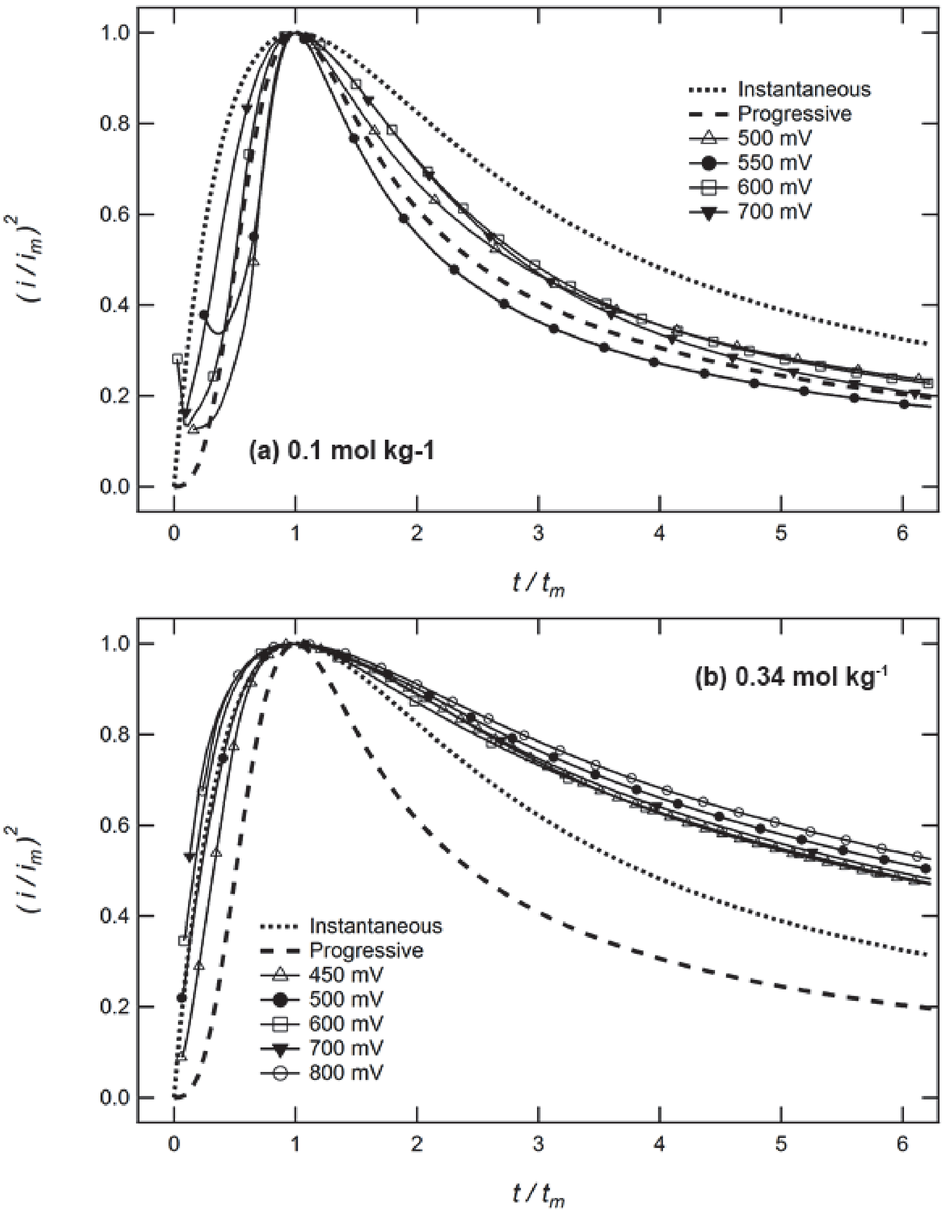

Figure 3.13. Chronoamperograms normalized to the maximum current and corresponding time for the potential step data for Zn(OTf)$_2$ concentrations of (a) 0.1 and (b) 0.34 mol kg^{-1} at 25ºC. Dashed lines correspond to the theoretical model of instantaneous and progressive nucleation.

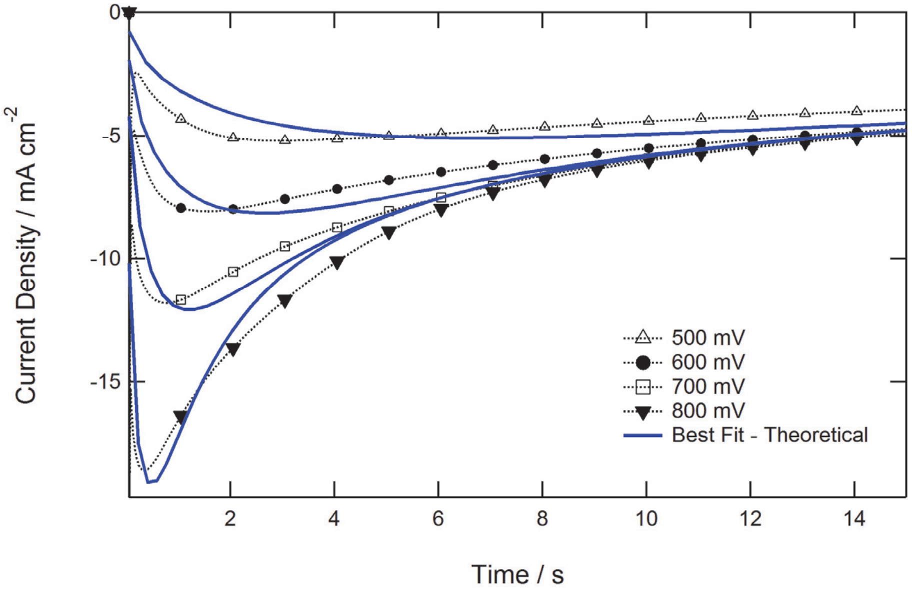

Figure 3.14. Best fit of the instantaneous nucleation model to the chronoamperometry data obtained with the 0.34 mol kg^{-1} (0.41 M) $Zn(OTf)_2$/BMIm OTf for various potential steps at 25°C.

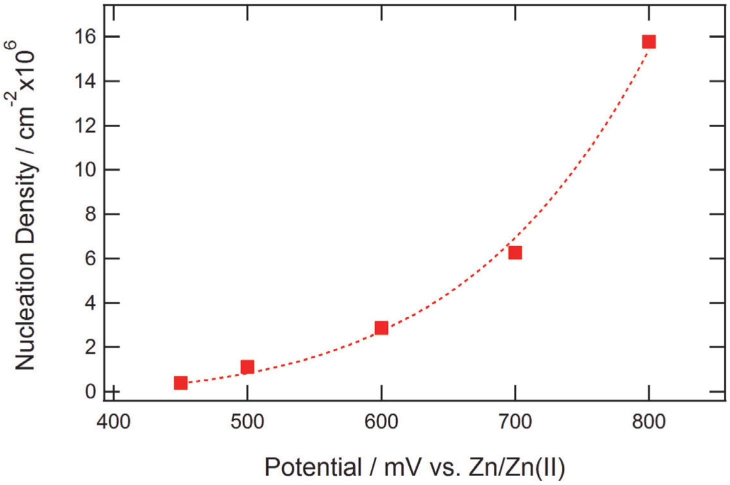

Figure 3.15. Calculated nucleation density obtained from the instantaneous nucleation model as a function of the applied potentials versus Zn/Zn(II) for electrodeposition within the 0.34 mol kg^{-1} (0.41 M) $Zn(OTf)_2$/BMIm OTf at 25°C

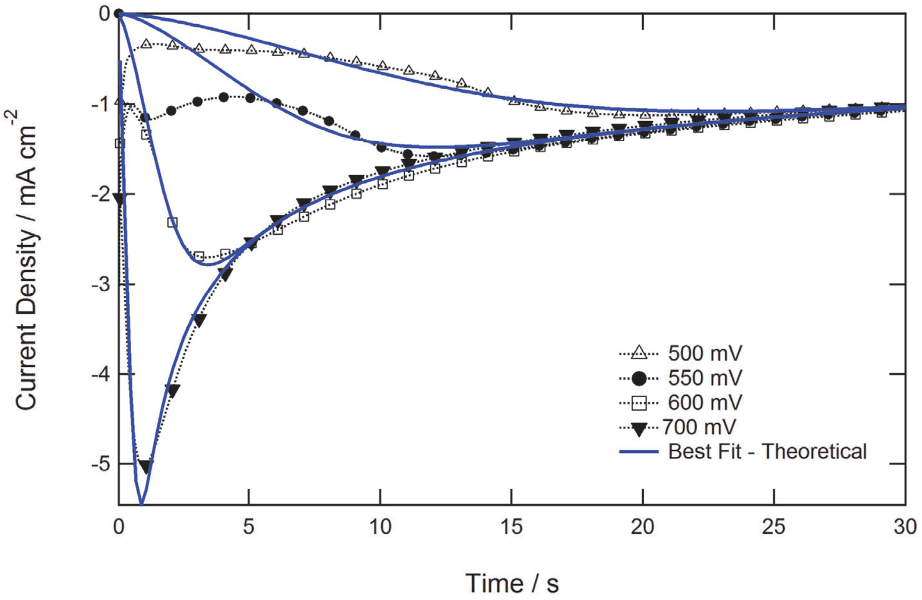

Figure 3.16. Best fit of the progressive nucleation model to the chronoamperometry data obtained with the 0.1 mol kg^{-1} (0.41 M) Zn(OTf)$_2$/BMIm OTf for various potential steps at 25°C.

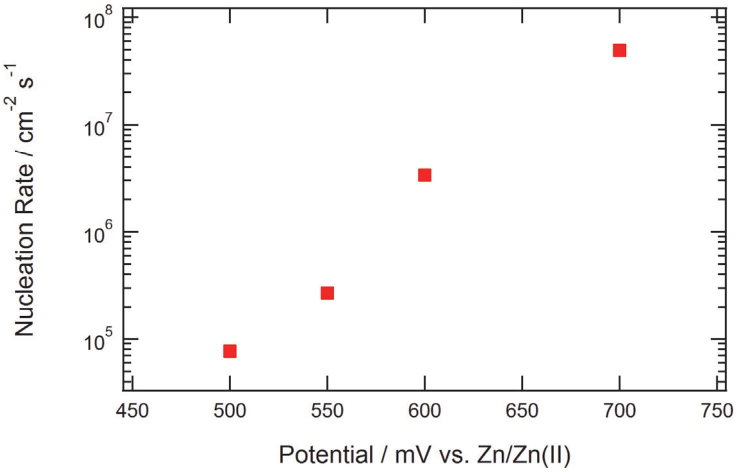

Figure 3.17. Calculated nucleation rates obtained from the instantaneous nucleation model as a function of the applied potentials versus Zn/Zn(II) for electrodeposition within the 0.34 mol kg^{-1} (0.41 M) Zn(OTf)$_2$/BMIm OTf at 25°C.

3.4 Conclusions

This chapter investigated the electrochemical behavior of Zn(II) within the $Zn(OTf)_2$/BMIm OTf ionic liquid electrolyte by utilizing electrochemical methods such as cyclic voltammetry (CV) and chronoamperometry. Electrodeposition of zinc was conducted on a Pt substrate and the potential was referenced to Zn/Zn(II). The influence of zinc salt concentration, temperature, and applied potential were investigated. The three levels of zinc salt concentrations analyzed were $Zn(OTf)_2$ concentrations of 0.05, 0.1, and 0.34 mol kg^{-1}. In addition, the electrochemical behavior of the system was analyzed at 25, 35, 45, and 55 ºC.

From the CV analysis, a single cathodic peak represented the reduction of Zn(II) to Zn. The system exhibited irreversible behavior since measured potential at the cathodic peak decreased with increasing scan rates. Furthermore, the charge transfer that occurred during the CV analysis at the 5 mV s^{-1} scan showed that the charge passed during the anodic current was 10% lower than the cathodic current for the 0.34 mol kg^{-1} concentration and 30% lower for the 0.1 mol kg^{-1} concentration. This suggests that either the zinc was not completely oxidized within the anodic region or there was a parasitic reaction occurring in the cathodic region. Finally, the peak cathodic current measured from the CV analysis increased with the square root of the scan rate as expected for a diffusion limited system.

The CV analysis of the neat BMIm OTf exhibited a wide electrochemical stability window of around 2.6 V with a range from -900 mV to 1700 mV versus the Zn/Zn(II) reference. In addition, no peaks were observed that would indicate the presence of water within the ionic liquid.

The diffusion coefficient of Zn(II) within the $Zn(OTf)_2$/BMIm OTf ionic liquid electrolyte was estimated from the chronoamperometry analyses. The estimated diffusion coefficient of Zn(II) increased with increasing temperature from 25 to 55°C. At 25ºC, the diffusion coefficient of Zn(II) was estimated to be 1.5×10^{-7} cm^2 s^{-1}. At 55ºC, the diffusion coefficient was estimated to be as high as 5.5×10^{-7} cm^2 s^{-1} for the 0.34 mol kg^{-1} concentration. The values obtained for the diffusion coefficients were within the same range as values obtained from other investigations within Zn(II) within imidazolium based ionic liquid systems [21, 32].

The nucleation behavior of Zn on the Pt substrate was analyzed by the current transient measured from the chronoamperometry analysis. Comparing the current transient to the Scharifker model [31], the 0.34 mol kg^{-1} $Zn(OTf)_2$ concentration most closely followed instantaneous nucleation behavior and the lower zinc salt concentrations of 0.05 and 0.1 exhibited progressive nucleation. The nucleation behavior did not appear to be influenced by temperature within the range analyzed (25 to 55ºC).

The 0.34 mol kg^{-1} $Zn(OTf)_2$ concentration appeared to exhibit instantaneous nucleation behavior, the theoretical nucleation density was calculated using the instantaneous nucleation model. The calculated nucleation density increased exponentially with increasing overpotential with values ranging from 0.6 × 10^6 cm^{-2} at -450 mV versus Zn/Zn(II) to 16 × 10^6 cm^{-2} at -800 mV versus Zn/Zn(II).

In contrast to the Zn deposition behavior within the 0.34 mol kg^{-1} concentration, Zn deposition within the 0.1 mol kg^{-1} $Zn(OTf)_2$ concentration exhibited progressive nucleation behavior. The theoretical nucleation rate was calculated from the progressive nucleation model and the nucleation rate appeared to scale logarithmically with the applied overpotential. The nucleation rate varied from 8 × 10^4 cm^{-2} s^{-1} at -500 mV versus Zn/Zn(II) to 7 × 10^7 cm^{-2} s^{-1} at -500 mV.

4. In-situ Electrochemical Atomic Force Microscopy (AFM)

In-situ analysis of the zinc deposition by atomic force microscopy (AFM) allows for analyzing the topography of the zinc deposition morphology. The capabilities of the AFM allow one to directly measure morphological quantities that are typically difficult to obtain by other imaging methods such as electron and optical microscopy. For example, the AFM allows for direct measurement of the surface texture and roughness and allows one to observe the surface evolution. In addition, since the AFM image is built from the interactions of a probe with the sample instead of relying on transmission through a sample, the AFM lends itself as a technique for in-situ electrochemical investigations.

An in-situ AFM analysis was conducted on the electrodeposition of zinc within an ionic liquid electrolyte under various deposition conditions. The zinc deposition on a substrate was conducted potentiostatically and AFM images of the zinc morphology were obtained during electrodeposition. The zinc morphology was characterized and the growth rates of individual zinc grains were measured. In addition, statistical analysis was conducted on the AFM data that included surface roughness and characterization utilizing the height difference correlation function. The information gained from this analysis allowed for a better understanding of the morphological behavior of zinc deposition within an ionic liquid and how its deposition behavior was influenced by the electrolyte and by the deposition potential.

4.1. Imaging with the AFM

Imaging with an AFM is conducted by scanning a probe over the surface of the sample to build the height topography of the surface within a selected region. An AFM relies on several components to build an image, as shown in Figure 4.1. The three main components are the piezoelectric transducer, a force transducer, and a feedback control. The piezoelectric transducer is made of a material that converts electrical potential into mechanical motion. The height of the AFM tip is controlled by changing the potential applied to the piezoelectric transducer. As the tip comes into contact with the surface, the force between the tip and the surface is measured with the force transducer. The force transducer is typically the cantilever with an optical lever. The feedback control is required to help maintain a constant force on the AFM tip as it follows the contours of the surface by controlling the amount of expansion of the piezoelectric transducer. Maintaining a constant force between the tip and the sample also sets the distance between the tip and the sample. Therefore, the distance that the piezoelectric moves up or down while the probe travels across the surface will represent the sample topography. A three-dimensional height image is then obtained by monitoring the voltage applied to the piezoelectric transducer as the tip scans across the surface.

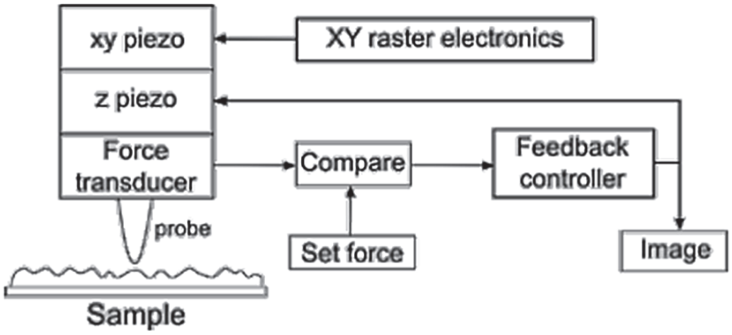

Figure 4.1. Diagram highlighting the main components for AFM operation. Reproduced from Eaton and West [38].

The AFM cantilever and tip are fabricated by using microelectromechanical systems (MEMS) technology and is typically made of silicon or silicon nitride. The geometry of the tip is critical to the quality of the images that are obtained by the AFM. Surface features such as a pit or a crack cannot be imaged correctly if the AFM tip cannot reach to the bottom of the feature as highlighted in Figure 4.2. An AFM tip is typically a 4 sided pyramid of a few microns in height. Tips, however, are used with various height to width aspect ratios depending on the application.

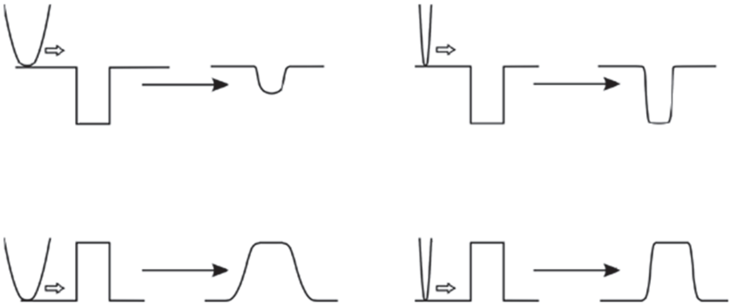

Figure 4.2. Comparison of height profiles obtained from a dull tip (left) to the profiles obtained from a sharp tip (right). Reproduced from Eaton and West [38].

The two main AFM topographic modes used in this research were contact mode and tapping mode. In contact mode, the AFM tip is in direct contact with the sample surface and the tip applies a force to the sample surface. During contact mode, a combination of cantilever bending and sample compression occurs. A set-point is used to maintain a certain cantilever deflection as measured by the force transducer. Since the forces applied to the surface and the tip can be high, one should consider that the tip and the sample can be damaged during imaging. Also, the nature of the sample surface may affect the imaging results. The advantage of contact mode is an increased resolution and the ability to image faster than other modes. The tradeoff is the possibility of damaging the sample and the AFM tip.

The second AFM mode used in the research is tapping mode (also termed non-contact mode). In tapping mode, an input signal is applied to the cantilever that vibrates the AFM tip. The movement of the tip is then dependent on its interaction with the sample surface. Typically, the AFM tip is oscillated near its natural resonant frequency and the amplitude of the oscillations is controlled by the operator. As the oscillating tip is brought close to the surface, the detected change in the oscillation that occurs from the force interaction with the surface is detected. A force interaction set point is then used with the feedback loop to maintain a constant force interaction between the tip and the surface as the tip moves across the surface. The advantage of tapping mode is the ability of using a smaller force than required for contact mode to image the surface thus reducing the risk of damaging the sample with the tradeoff of lower resolution and slower scanning speeds.

An AFM image is obtained by moving the AFM tip across the sample in a raster scan pattern that has a fast scan direction (designated as the X direction) and a slow scanning direction (designated as the Y direction). The surface topography map is created by measuring the Z position of the cantilever for each X and Y position. The Z position is the measured voltage on the Z piezo that is required to maintain a constant deflection of the cantilever (or constant tip force on the sample). The two main data channels collected during an AFM scan in contact mode are the Z position (height) and the deflection.

The deflection is related to the force acting on the sample. A setpoint is chosen to maintain the deflection of the cantilever at a certain value. The setpoint largely determines the amount of force used to keep the tip in contact with the surface. The higher the difference between the free deflection and the setpoint, the higher the tip will be pushed on the surface. The deflection data channel is the error signal of the feedback used to maintain the deflection value as the tip moves across the surface. If the feedback loop was perfect, then the deflection image would look flat. The feedback loop, however, is not perfect since the tip encounters sudden changes in topography during scanning. The ability of collecting these sudden changes in topography allows the deflection channel to be used for resolving edges that may be obscured in the height data. Since the deflection image shows the height single error, where positive deflections are lighter in color and negative deflections are darker in color, the image typically shows a shaded appearance of the surface as if the surface is illuminated by a light source.

The height channel is used to construct the surface topography image and it is obtained from the voltage applied to the Z piezo in order for the cantilever to maintain a set deflection set point. The image is scaled from voltage to distance with a linear scale factor. Piezo materials do not respond linearly with voltage, however, and accurate measurement of sample features should be conducted for feature sizes of less than 100 nm. To obtain better height measurement above 100 nm, some AFM manufacturers include a second sensor that directly measures the height of the AFM lever. The AFM instrumentation used in this investigation uses a Linear Variable Differential

Transformer (LVDT) as a second sensor to directly measure the height of the lever. Although the LVDT allows for accurate measurement of height above 100 nm, the tradeoff of using the LVDT to measure the height is that it does not have the resolution capabilities of the height measurement obtained from the optical lever for features smaller than 100 nm.

4.2. AFM Analysis

One of the main benefits of the AFM is the capability of creating three-dimensional topographic maps of the surface. The topographic map of the surface allows for analysis of particle volumes, height aspect ratios, and accurate geometry measurements. The height data collected from the AFM lends itself to statistical analysis as well and this section overviews the statistical methods used in this investigation. The first section overviews surface roughness characterization and the second section discusses the use of a correlation function used to analyze the topography obtained from the AFM imaging.

4.2.1. Statistical Analysis

Roughness is one of the parameters that are measured with the AFM and the most commonly used roughness parameter is the root-mean squared roughness (RMS). A surface that exhibits a higher RMS indicates that the surface exhibits a greater topological variation. The formula for calculating the RMS is

$$\mathrm{RMS} = \sqrt{\frac{1}{n}\sum_{i=1}^{n}\left|y_i^2\right|} \tag{4.1}$$

where n is the number of data points and y is the height measurement of the data point i. For AFM imaging, the degree of data correcting such as leveling and background subtraction strongly influences the roughness measurements. Therefore, it is important to process all the data under similar conditions so that the calculated roughness parameters remain valid for comparison.

4.2.2. Height Difference Correlation Function

The surface topography of metal electrodeposition can be treated as a fractal surface for quantitative analysis. Techniques for characterizing fractal surfaces include the family of height difference correlation functions [39] (Page 130). These functions allow for analysis of the dependence of the average height difference to the horizontal separation distance between pairs of points. In other words, the functions tell how the roughness changes as the horizontal length scale used to measure the roughness changes. Figure 4.3 shows an illustration on how the surface roughness varies with the length scale used to measure the surface roughness. Initially, the roughness increases with increasing length scales until the roughness saturates at some critical value (typically termed the correlation length). Above this critical value, the roughness remains constant with increasing length scales.

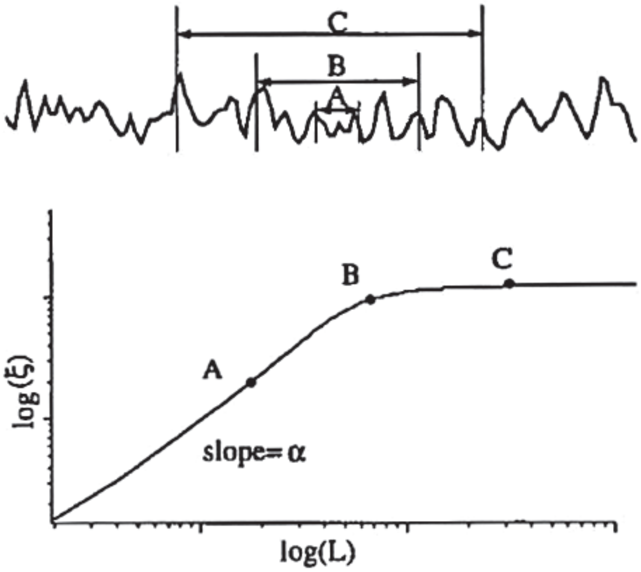

Figure 4.3. Illustration on how the surface roughness varies with the length scale used to measure the roughness. For this figure, ζ represents the standard deviation of the surface height and L is the length scale of the measurement. Figure reproduced from Tong and Williams [40].

The AFM data obtained from this investigation were analyzed utilizing the height difference correlation function. The height difference correlation function is the s of the difference between two points and allows for analysis of the scaling of the surface at different lengths [40]. The reader is referred to investigations by Schug et al. [41] and Huo and Schwarzacher [42] as examples of utilizing correlation functions to characterize AFM imaged surfaces. For AFM data, the height difference correlation, C_x, is typically analyzed along the fast scanning direction since the slow scanning direction may exhibit errors in the height data resulting from instrumental drift. The height difference correlation function for the fast scanning direction (x) is

$$C_x(\tau_x) = \frac{1}{N(M-m)} \sum_{l=1}^{N} \sum_{n=1}^{M-m} (z_{n+m,l} - z_{n,l})^2 \tag{4.2}$$

where τ_x is the distance between two points ($z_{n+m,l}$ and $z_{n,l}$) in the fast scanning direction, N is the number of scan lines along the y-axis, M is the number of data points along the fast scan direction (x-axis), and z is the corresponding height value of a given point.

Many real surfaces appear to exhibit self-affine fractal characteristics over certain measurement length scales. A self-affine fractal surface will scale at different amounts in the height direction (z-direction) than in the x- and y-directions. In contrast, a self-similar surface scales at the same amounts for all directions. If the surface exhibits self-affine fractal characteristics, the height difference correlation function can be described by the following relation [40]

$$C_x(\tau_x) = 2\sigma^2 \left[1 - exp\left(\left(-\frac{\tau_x}{L_x}\right)^{2H}\right)\right] \tag{4.3}$$

where σ is the root mean square of the height deviation, L_x is the horizontal correlation length, and H is the scaling factor (Hurst exponent). This expression allows one to describe a surface that follows a Gaussian distribution by just three parameters: σ, L_x, and H.

Figure 4.4 shows an example of how the parameters describing a Gaussian surface relate to the height difference correlation. The Hurst exponent, H, describes how the surface roughness scales with the measurement distance, τ_x, in the region where τ_x is less than the horizontal correlation length, L_x. For a locally smooth surface, the Hurst exponent approaches one [39]. The correlation length is the characteristic length of the surface and it is the crossover between the scaling regime (described by the Hurst exponent) and the saturated regime. In the saturated regime, at $\tau_x > L_x$, the power difference of the height saturates at σ. Furthermore, the value for σ calculated from the saturated regime is comparable to the calculated RMS of the surface.

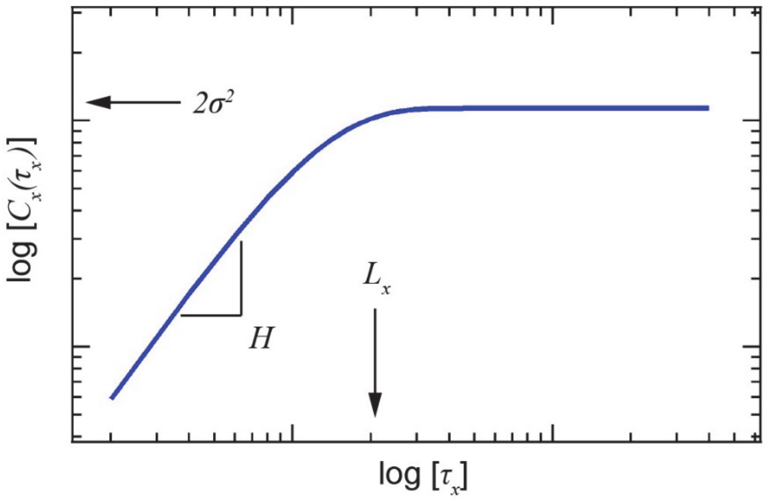

Figure 4.4. A log-log plot showing an example of a typical relationship of the height difference correlation, $C_x(\tau_x)$, to the measurement distance, τ_x, for a surface exhibiting Gaussian behavior.

As the surface grows during electrodeposition, the height difference correlation typically follows two types of behavior shown in Figure 4.5 [43]: normal and anomalous scaling. During growth, normal scaling exhibits a constant local scaling behavior and local surface roughness. The local surface roughness is defined as the roughness measured at a length scale, τ_x, that is less than the horizontal correlation length, L_x. In this investigation, the local surface roughness is also termed the local surface height difference correlation. Normal scaling also exhibits an increasing correlation length and saturated surface roughness with growth. In contrast, both the local and saturated surface roughness increase during anomalous scaling.

Electrodeposition typically consists of island formation and growth followed by island coalescence. The island formation and growth typically follows anomalous scaling up to island coalescence. After island coalescence, the growth starts to follow normal scaling [43]. This transition from anomalous to normal scaling behavior was observed by Iwamoto et al. for the electrodeposition of Cu from a copper sulfate plating solution. As the Cu islands grew on the substrate surface, the island height increased as well as the island perimeter. This increase by both the height and the perimeter increased the height difference correlation across all the length scales resulting in anomalous scaling. After the islands coalesce, the electrodeposition of Cu then transitioned from anomalous to normal scaling behavior [44].

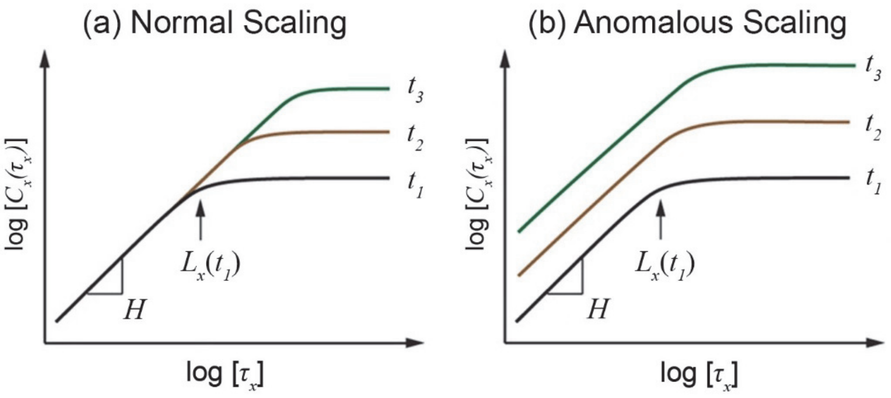

Figure 4.5. Height difference correlation for dynamic scaling with increasing time, t, for surface growth exhibiting normal scaling (a) and surface growth exhibiting anomalous scaling (b). Figures modified from Guo et al. [43].

4.3. AFM Experimental

This section overviews the experimental procedure for the in-situ AFM analysis of zinc deposition within an ionic liquid electrolyte. First, details are given on the instrumentation and data collection method. Next, the preparation of the ionic liquid electrolyte is given and electrochemical cell assembly is overviewed. The electrodeposition parameters that were varied for this investigation are overviewed. In addition, this section overviews how the zinc deposition thickness was monitored during the in-situ trials. Finally, details on how the AFM data were corrected and the procedures for the data analysis are given.

The electrochemical cell used for the AFM analysis is detailed in Chapter 3 section 3.2. Also, the ionic liquid preparation was similar to that followed for the electrochemical analysis detailed in Chapter 3 section 3.2.

4.3.1. Instrumental

Atomic force microscopy (AFM) images were obtained using an Asylum MFP3D instrument capable of 90 µm closed loop travel. A silicon nitride AFM tip was used for imaging on a silicon nitride cantilever (Olympus TR800PSA). On the AFM tip assembly, two sets of AFM levers were available. One lever with a length of 200 µm and a spring constant of 0.15 was used to measure the deposition thickness. The second lever with a length of 100 µm and a spring constant of 0.57 was used for AFM imaging. All imaging data collected within the ionic liquid electrolyte were obtained in contact mode. AFM data were collected using MFP3D imaging software (version 111111+1219) that is a user interface within IGOR Pro (software version 6.2.2.2). For contact mode imaging, data collected included the height channel, deflection channel and the LVDT sensor channel.

Zinc deposition for the AFM analysis was conducted potentiostatically with a three-electrode cell using a Bio-Logic SP-300 potentiostat/galvanostat. Electrochemical measurements were collected with the potentiostat/galvanostat utilizing EC-Lab® software (version 10.23).

Electron microscopy was conducted ex-situ on the final Zn deposition morphology for selected samples. The electron microscopy was conducted on a JEOL JSM-7401F FESEM scanning electron microscope. Images were obtained using the lower secondary electron detector (LEI mode) that allowed for better imaging of the Zn deposition topography.

4.3.2. Ionic Liquid Electrolyte Preparation

For this AFM investigation, preparation of the ionic liquid followed a similar procedure as followed for the electrochemical analysis presented in Chapter 3 (refer to section 3.2). The ionic liquid for the AFM analysis, however, was obtained from a different vendor (Ionic Liquid Technologies, Inc.). The ionic liquid, 1-butyl-3-methyl-imidazolium trifluoromethanesulfonate (BMIm OTf) used in the electrochemical analysis was obtained from EMD Chemicals. The ionic liquid obtained from Ionic Liquid Technologies, Inc. was certified at the same purity as the ionic liquid from EMD Chemicals with a purity level of greater than 99%. Electrochemically, the behavior of the ionic liquids from the two different vendors appeared to be similar.

Two different $Zn(OTf)_2$ concentrations were analyzed in this investigation: 0.1 and 0.34 molal (mol kg^{-1}). Table 4.1 tabulates the measured concentrations for the two $Zn(OTf)_2$ concentrations. The $Zn(OTf)_2$ concentrations are presented as molal quantities (mol kg^{-1}) throughout this chapter.

Table 4.1. Targeted and measured $Zn(OTf)_2$ molal concentrations for the ionic liquid electrolyte. The error given is the measurement error for the measured molal concentration.

Targeted Molality (mol kg^{-1})	Measured Molality (mol kg^{-1})	Error (+/-)
0.1	0.1045	0.001
0.34	0.3393	0.001

4.3.3. Electrochemical Cell Assembly and AFM Measurement

The substrate used for Zn deposition analysis consisted of a 1 mm diameter platinum disk that was sputter deposited on a 0.5 mm thick glass wafer. The surface roughness of the Pt disk electrode measured around 3 nm RMS (from AFM measurements). The counter and reference electrodes were Zn wire and potentials were referenced to Zn/Zn(II). The reader is referred to section 3.2 for further information on the electrochemical cell setup.

Figure 4.6 also shows the location of where the AFM measurements were obtained during the Zn deposition analysis. AFM imaging was conducted at a location between 200 to 250 μm from the edge of the disk electrode. The deposition thickness was measured at the edge of the electrode as shown in Figure 4.6. During electrodeposition, the AFM assembly was moved off the Pt substrate in the direction highlighted in Figure 4.6. Moving the assembly away from the Pt substrate assured that the assembly was not electrically shielding the Pt substrate during electrodeposition. Although the assembly was moved away from the last AFM scan location for each deposition pulse, the assembly was able to be returned to same location to within 2 μm.

Although roughly 4 mm of the Pt substrate leg used for the electrical connection was in contact with the electrolyte, the Pt leg was effectively electrically shielded by the AFM cantilever assembly (refer to Figure 4.6). Minimal Zn deposition was observed along the Pt leg after deposition and this area was not calculated for the current density.

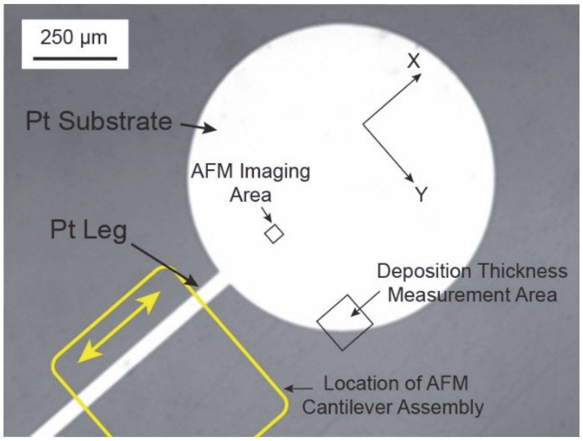

Figure 4.6. Optical micrograph of the Pt disk electrode used for AFM analysis. The electrical connection to the disk electrode was from a Pt leg as highlighted. The AFM cantilever assembly was located just above the Pt leg as shown schematically. The assembly was moved off the Pt electrode during electrodeposition pulses. The areas on the Pt surface analyzed by AFM are shown and the direction of the fast scanning and slow scanning are noted (X direction and Y direction respectively),

4.3.4. Electrodeposition of Zinc

Prior to the deposition analysis, the Pt substrate was initialized by potentiostatic reduction of Zn at -500 mV versus Zn/Zn(II) for a total charge passed of 52.3 mC cm^{-2}. The Zn deposit was then removed by potentiostatic oxidation at +200 mV versus Zn/Zn(II). This initiation step appeared to eliminate problems that were often encountered with the first deposition pulse where the initial deposition was uneven across the Pt substrate. In addition, the initiation step allowed for measurement of the resting potential of the system after Zn was deposited on the Pt substrate. The resting potential of the Zn deposit covering the Pt substrate was between -100 to -170 mV versus the Zn/Zn(II) reference. The large discrepancy of the resting potential of the Zn deposition to the Zn/Zn(II) reference was attributed to the inherently high resistivity of the ionic liquid electrolyte and the large distance of 10 to 12 mm between the reference electrode and the Pt substrate (working electrode).

The in-situ analyses of Zn deposition within the ionic liquid were conducted with pulses at a constant reducing potential (potentiostatic deposition) versus the Zn/Zn(II) reference. The total charge per pulse was either 52.3 mC cm^{-2} for the deposition conducted within 0.1 mol kg^{-1} Zn(OTf)$_2$/BMIm OTf electrolyte or 104.6 mC cm^{-2} for deposition conducted within 0.34 mol kg^{-1} Zn(OTf)$_2$/BMIm OTf . The charge passed of 52.3 mC cm^{-2} and 104.6 mC cm^{-2} corresponds to 100 and 200 ideal Zn monolayers (ML) respectively. Electrodeposition was carried out at 25°C and the electrolyte remained unstirred.

Six different deposition parameters were analyzed for this investigation. For each parameter, deposition was carried out with a series of pulsed depositions with AFM imaging between the deposition pulses. Typically, the electrodeposition for the AFM analysis was conducted until a total charge of 1464.4 mC cm^{-2} was passed (corresponding to 2800 ideal Zn monolayers).

Table 4.2 lists the parameters analyzed for the Zn deposition investigation where the Zn(OTf)$_2$ concentration was either 0.1 or 0.34 mol kg^{-1} and the deposition potential varied from -400 to -700 mV versus the Zn/Zn(II) reference. Table 4.2 also lists the measured resting potential after Zn was electrodeposited on the Pt substrate. The deposition overpotential listed in Table 4.2 was calculated by subtracting the resting potential from the applied deposition potential versus the Zn/Zn(II) reference. A large measurement error for the resting potential was noted in Table 4.2 and this measurement error was attributed to the sluggish kinetics of the system.

A typical in-situ experiment consisted of potentiostatic deposition for a desired amount of charge passed (either 52.3 mC cm^{-2} or 104.6 mC cm^{-2}) followed by holding at a slightly reducing potential of around -5 mV versus the resting potential for AFM imaging. This process of Zn deposition and imaging was then repeated. The electrodeposition pulses typically were conducted within 60 seconds and holding at a slightly reducing potential for the AFM imaging was around 10 minutes.

After the final deposition cycle, the deposited Zn was removed through oxidation by holding at a constant potential of +200 mV versus the Zn/Zn(II) reference. In addition, some samples were removed without oxidizing and washed for ex-situ SEM analysis. The ionic liquid electrolyte was washed from the sample with ethanol and Millipore water.

Table 4.2. Electrodeposition parameters for each of the AFM in-situ investigations.

Test	**Zn(OTf)$_2$ Concentration (mol kg^{-1})**	**Deposition Potential (mV vs. Zn/Zn(II))**	**Resting Potential (mV vs. Zn/Zn(II))**	**Deposition Overpotential (mV)**
A	0.1	-430	-100 ± 10	-330 ± 10
B	0.1	-600	-100 ± 10	-500 ± 10
C	0.34	-400	-130 ± 10	-270 ± 10
D	0.34	-500	-170 ± 10	-330 ± 10
E	0.34	-650	-130 ± 10	-520 ± 10
F	0.34	-700	-150 ± 10	-550 ± 10

4.3.5. Deposition Thickness Measurement

At selected intervals during the in-situ analysis of Zn deposition, the total Zn deposition thickness on the Pt electrode was measured using a second AFM tip on the cantilever assembly. The tip was scanned along the edge of the electrode as noted in Figure 4.6. A height image was obtained from the LVDT sensor channel. The AFM tip was scanned at the instrument's limit of 90 μm × 90 μm and collected 256 data points per line. The glass substrate was used for a height reference and the thickness of the deposition was measured from subtracting original Pt substrate thickness from the average total thickness measured after Zn deposition. Figure 4.7 shows the three-dimensional image obtained by the AFM of the electrode edge and the glass substrate used for the deposition thickness measurement.

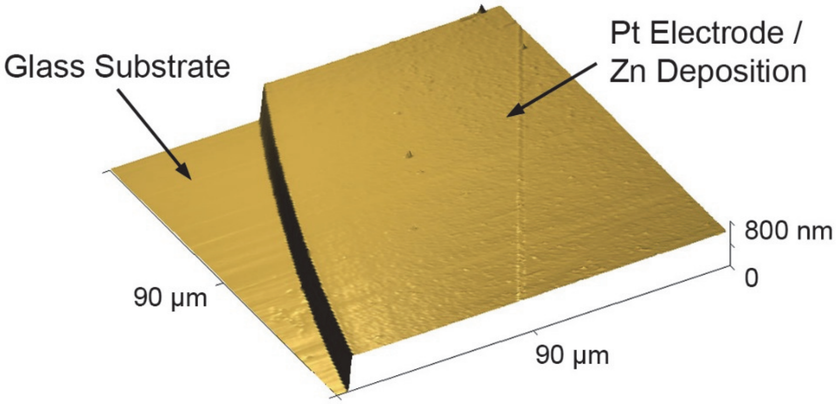

Figure 4.7. Three-dimensional AFM image of the Pt electrode edge before Zn deposition and the underlying glass substrate. The scanning area 90 µm × 90 µm. The AFM images of the electrode edge were used to measure the Zn deposition thickness.

4.3.6. Data Analysis

The scanning area of the AFM images used for analysis measured 4 µm × 4 µm with 512 data points per scan line. AFM images were analyzed within Gwyddion open source software (version 2.31) [45]. Both the height data channel and the LVDT sensor channel were used for analysis of the AFM data. The height channel was used to obtain the topography images and to measure surface features of less than 100 nm.

The height data from the LVDT sensor channel was used for data analysis. The topographic data from the LVDT sensor was leveled with using a plane fit within the Gwyddion software. If large features were present, these features were temporarily masked for the plane leveling step so that these large features would not introduce leveling errors. The roughness parameters and the height difference correlation dependence were obtained within the Gwyddion software from the leveled LVDT sensor data.

4.4. Results and Discussion

This section presents the results obtained from the in-situ AFM analysis of zinc deposition within an ionic liquid electrolyte. The electrochemical behavior observed during the zinc deposition is given in the first section. The second section overviews the deposition film thickness measurements that were conducted during the in-situ analysis. The third section presents the morphological evolution of zinc with increasing deposition thickness. The fourth section compares the in-situ AFM images to ex-situ scanning electron microscopy (SEM) images of the zinc deposition morphology. Finally, statistical analysis of the AFM data is presented in the fifth section.

4.4.1. Electrochemical Behavior

Chronoamperograms from the deposition conducted within 0.1 mol kg^{-1} $Zn(OTf)_2$/BMIm OTf electrolyte at -430 mV versus Zn/Zn(II) are shown in Figure 4.8. The first deposition pulse on the Pt substrate resulted in a current density profile that exhibited a reducing peak at around 4 seconds of deposition for a peak current of -1.8 mA cm^{-2}. The current decreased with continued time exhibiting diffusion limited behavior. With subsequent pulses, the initial current peak was no longer observed. Instead, the current decays following diffusion limited behavior. The total time required to pass 52.3 mC cm^{-2} (100 Zn monolayers) was 50 seconds for the first deposition pulse and the time required increased to 76 seconds by the tenth deposition pulse. For the last half of the deposition, the reducing current was around -0.5 mA cm^{-2}.

Within the same $Zn(OTf)_2$ concentration at a lower reducing voltage of -600 mV versus Zn/Zn(II), the chronoamperograms exhibited similar behavior as observed at -430 mV as shown in Figure 4.9. The chronoamperograms for the initial deposition on the Pt substrate exhibited a small current peak at 1.5 seconds with a maximum current of -3 mA cm^{-2}. This initial current peak was attributed to nucleation of Zn on the Pt substrate. Subsequent pulses did not exhibit a current peak and instead exhibited diffusion limited behavior. The total time required to pass 52.3 mC cm^{-2} was 41 seconds for the first deposition pulse and 63 seconds by the sixth pulse. The reducing current for a given time was observed to decrease with subsequent pulses. By the sixth pulse, the reducing current for the last half of deposition was between -0.7 to -0.5 mA cm^{-2}.

The chronoamperograms for the deposition within 0.34 mol kg^{-1} $Zn(OTf)_2$/BMIm OTf electrolyte at -400 mV versus Zn/Zn(II) is shown in Figure 4.10. For this analysis, the first deposition pulse was conducted at -500 mV versus Zn/Zn(II) for a total charge passed of 52.3 mC cm^{-2} to assure adequate Zn deposition across the Pt substrate. Subsequent deposition pulses at -400 mV versus Zn/Zn(II) exhibited current peaks. After the current peak, the system appeared to follow diffusion limited behavior where the current continued to decrease with increasing deposition time. The current transient peak for the second pulse was 20 seconds at -2 mA cm^{-2}. With subsequent pulses, the current was observe to increase for a given deposition time. By the 5th pulse, the current transient exhibited a peak was around 12 seconds for a reducing current of -2.5 mA cm^{-2}. The total time required to pass 104.6 mC cm^{-2} (200 ideal Zn monolayers) was about 50 seconds.

For deposition at -500 mV versus Zn/Zn(II), the chronoamperograms for all the pulses exhibited similar behavior as shown in Figure 4.11. The reducing current exhibited a peak at between 17 to

22 seconds for a reducing current of between 2.4 to 2.5 mA cm^{-2}. The total time required to pass 104.6 mC cm^{-2} (200 ideal Zn monolayers) was between 51 to 53 seconds and was similar to the time required for deposition at -400 mV versus Zn/Zn(II).

Figure 4.12 shows the chronoamperograms for selected deposition pulses within 0.34 mol kg^{-1} Zn(OTf)$_2$/BMIm OTf electrolyte at a reducing potential of -650 mV versus Zn/Zn(II). For the initial deposition on the Pt substrate, a reducing peak at 1.4 seconds for a reducing current of -8.4 mA cm^{-2} was observed. This reducing peak attributed to the nucleation of Zn on the Pt substrate. Subsequent deposition pulses exhibited only a minimal peak and the current transient appeared to follow diffusion limited behavior. The reducing current transient followed similar behavior for the deposition pulses. At 5 seconds of deposition time, the reducing current was between -6 and -7 mA cm^{-2}. After 15 seconds, the reducing current dropped to between -4 to -5 mA cm^{-2}. The total time required to pass 104.6 mC cm^{-2} (200 ideal Zn monolayers) for each of the pulses was between 17 to 20 seconds.

The chronoamperograms for the deposition at a reducing potential of -700 mV versus Zn/Zn(II) within 0.34 mol kg^{-1} Zn(OTf)$_2$/BMIm OTf electrolyte is shown in Figure 4.13. The current transient for each of the pulses exhibited similar behavior with each pulse exhibiting a reducing current peak. The reducing current peak for the initial deposition pulse on the Pt substrate was 1.1 second for a reducing current -8.4 mA cm^{-2}. Subsequent pulses exhibited similar peak behavior. The total time required to pass 104.6 mC cm^{-2} (200 ideal Zn monolayers) for each of the pulses was between 19.5 to 21.5 seconds. The current transient behavior for the -700 mV pulses was similar to the current transient behavior observed with the -650 mV analysis.

Figure 4.14 plots the initial deposition pulses on the Pt substrate for the various deposition conditions analyzed within this investigation. The deposition within the 0.1 mol kg^{-1} Zn(OTf)$_2$/BMIm OTf electrolyte exhibited the same current transient behavior after deposition of 7 seconds. The current transient peak for the -600 mV deposition was higher than that obtained at -430 mV. For deposition within the 0.34 mol kg^{-1} Zn(OTf)$_2$/BMIm OTf electrolyte, the deposition at -700 and -650 mV versus Zn/Zn(II) exhibited similar current transients. The deposition at -700 mV exhibited a slightly higher reducing current peak than that observed at -650 mV (-9.0 mA cm^{-2} compared to -8.4 mA cm^{-2}). Regardless of the deposition conditions, all the current transients exhibited diffusion limited behavior and appeared to approach the same steady state current for their respective Zn(OTf)$_2$ concentrations.

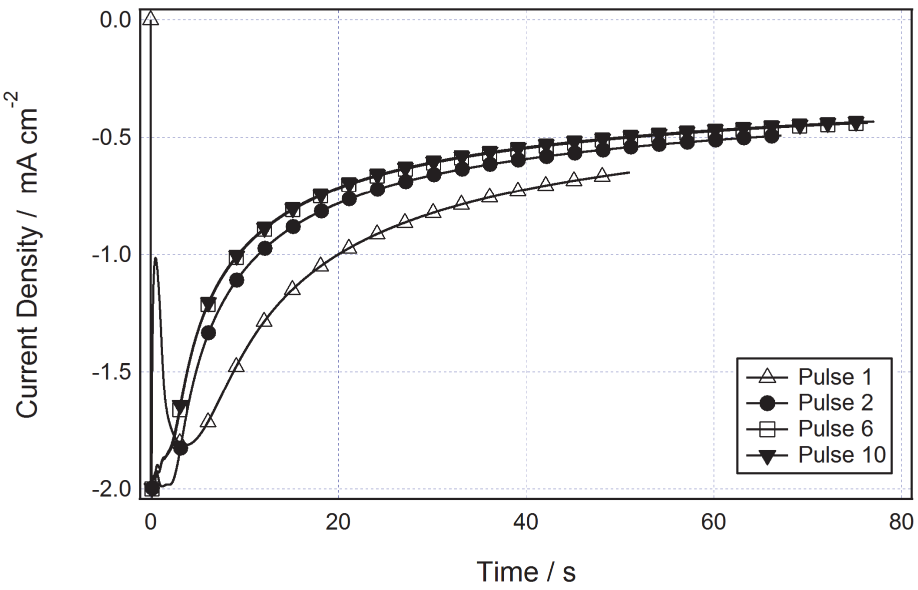

Figure 4.8. Selected chronoamperograms of Zn deposition pulses in 0.1 mol kg^{-1} Zn(OTf)$_2$/BMIm OTf at -430 mV versus Zn/Zn(II) reference. The total charge passed for each deposition pulse was 52.3 mC cm^{-2} (100 Zn monolayers).

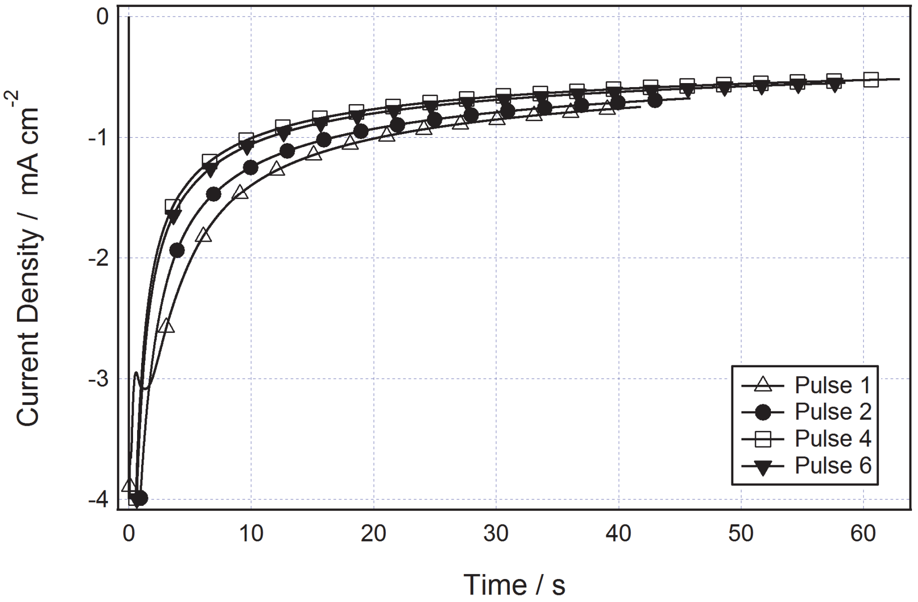

Figure 4.9. Selected chronoamperograms of Zn deposition pulses in 0.1 mol kg^{-1} Zn(OTf)$_2$/BMIm OTf at -600 mV versus Zn/Zn(II) reference. The total charge passed for each deposition pulse was 52.3 mC cm^{-2} (100 Zn monolayers).

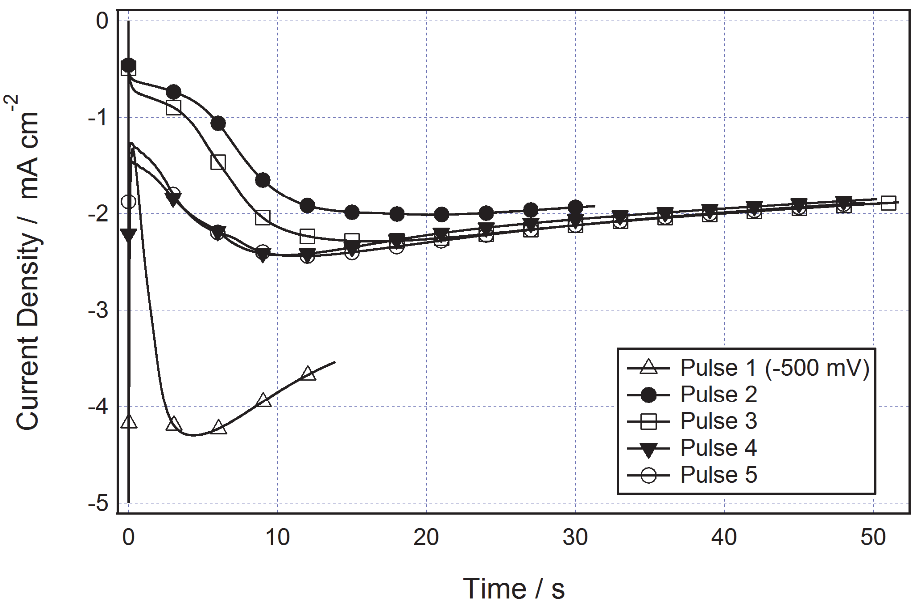

Figure 4.10. Selected chronoamperograms of Zn deposition pulses in 0.34 mol kg^{-1} Zn(OTf)$_2$/BMIm OTf at -400 mV versus Zn/Zn(II) reference. The first pulse was conducted at -500 mV versus Zn/Zn(II). The total charge passed for Pulse 1 and Pulse 2 was 52.3 mC cm^{-2} (100 Zn monolayers) and the total charge passed for subsequent pulses was 104.6 mC cm^{-2} (200 Zn monolayers).

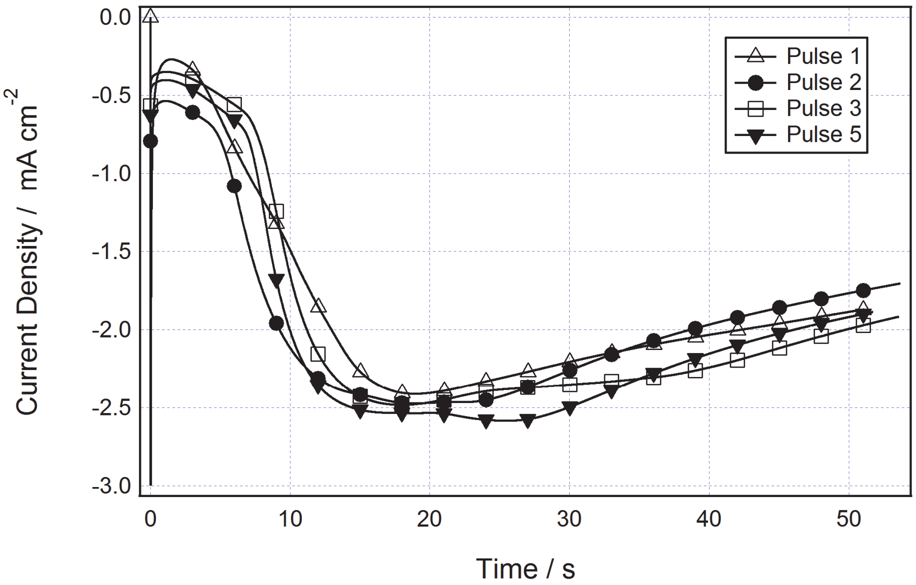

Figure 4.11. Selected chronoamperograms of Zn deposition pulses in 0.34 mol kg^{-1} Zn(OTf)$_2$/BMIm OTf at -500 mV versus Zn/Zn(II) reference. The total charge passed for each deposition pulse was104.6 mC cm^{-2} (200 Zn monolayers).

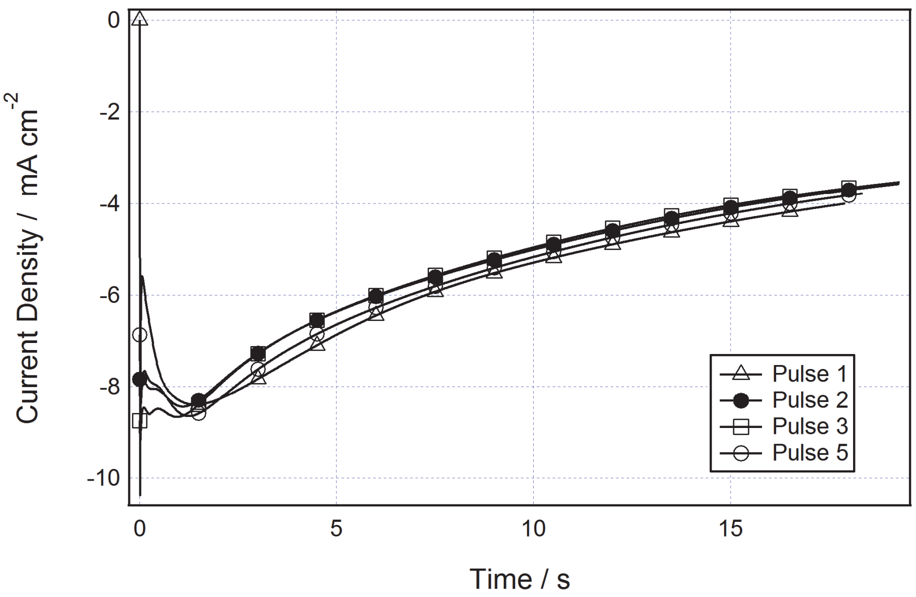

Figure 4.12. Selected chronoamperograms of Zn deposition pulses in 0.34 mol kg^{-1} Zn(OTf)$_2$/BMIm OTf at -650 mV versus Zn/Zn(II) reference. The total charge passed for each deposition pulse was 104.6 mC cm^{-2} (200 Zn monolayers).

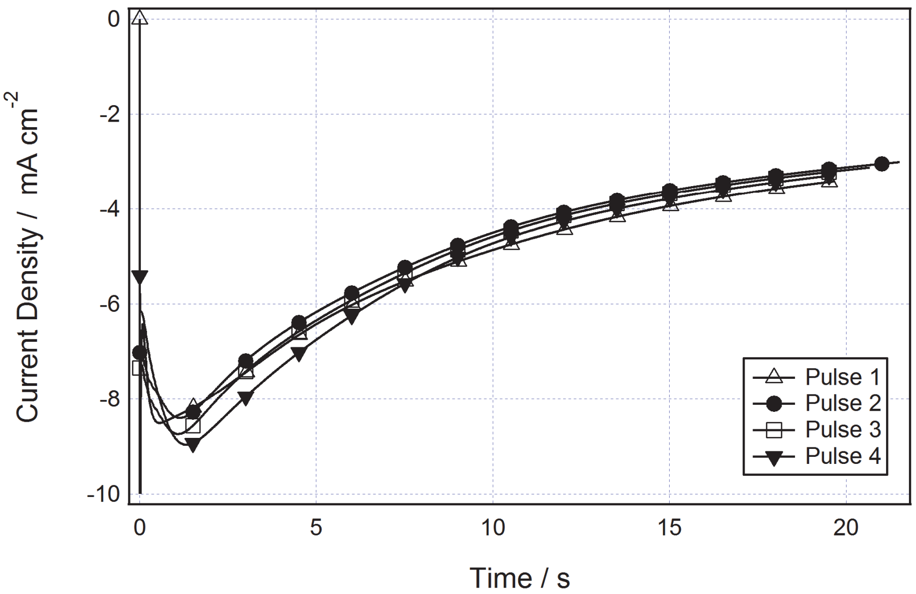

Figure 4.13. Chronoamperograms of Zn deposition pulses in 0.34 mol kg^{-1} Zn(OTf)$_2$/BMIm OTf at -700 mV versus Zn/Zn(II) reference. The total charge passed for each deposition pulse was 104.6 mC cm^{-2} (200 Zn monolayers).

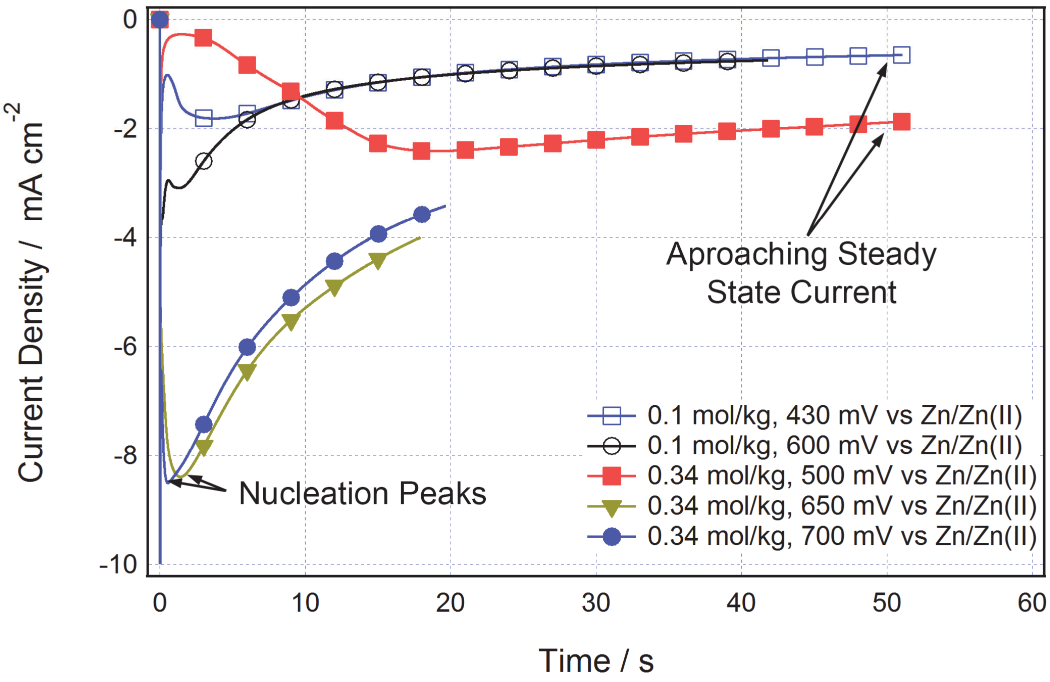

Figure 4.14. Chronoamperograms of the initial deposition pulse on the Pt substrate for various conditions analyzed. The total amount of charge passed was 52.3 mC cm^{-2} for the 0.1 mol kg^{-1} solutions and 104.5 mC cm^{-2} for the 0.34 mol kg^{-1} solutions.

4.4.2. Zinc Deposition Thickness Analysis

At selected intervals during the in-situ analysis of Zn deposition, the total Zn deposition thickness on the Pt electrode was measured using a second AFM tip on the cantilever assembly. Table 4.3 lists the measured thickness values of the selected scans along with the amount of charge that was passed in terms of ideal Zn monolayers (ML). Using the relation that one ideal monolayer of Zn is equal to 0.2477 nm, the ideal thickness was calculated and noted in Table 4.3.

Generally, the measured thickness of the Zn deposition was within 10% of the ideal thickness for the given amount of charge passed. Although a few measurements exhibited thicknesses above the ideal value, most thicknesses values were lower than the ideal thickness. From the deposition layer thickness measurements, the average thickness growth was 0.23 nm per Zn monolayer of charge passed. For comparison, the ideal growth rate would be 0.248 nm per Zn monolayer of charge passed assuming 100% electrodeposition efficiency.

Table 4.3. Zinc deposition thicknesses measured by the AFM after selected amounts of charge passed in terms of ideal Zn monolayers for various in-situ investigations conducted (refer to Table 4.2). The ideal Zn thickness for the amount of charge passed is given for comparison.

In-situ Test	Ideal Zn Monolayers (ML)	Ideal Zn Thickness (nm)	Measured Thickness (nm)
C (-400 mV)	800	198	208
C (-400 mV)	1000	248	244
C (-400 mV)	2000	495	418
D (-500 mV)	1000	248	278
D (-500 mV)	1200	298	302
D (-500 mV)	2800	694	672
E (-650 mV)	800	198	152
E (-650 mV)	1200	298	256
E (-650 mV)	2000	495	439

4.4.3. AFM Analysis

This section discusses the AFM observations from deposition within the ionic liquid electrolyte under various $Zn(OTf)_2$ concentrations and potentials. Six different deposition conditions were analyzed for this in-situ investigation as listed in Table 4.2. From these conditions, three types of the deposition behavior were observed from the AFM analysis. The deposition conducted at the low electrolyte concentration of $Zn(OTf)_2$ (0.1 mol kg^{-1}) resulted in the formation and growth of boulder like Zn morphology. For the second case, the Zn deposition morphologies became dominated by grains oriented at an angle in relation to the substrate. This type of behavior was observed for the in-situ trials conducted with potentiostatic deposition at -400, -500 and -650 mV versus the Zn/Zn(II) reference within a 0.34 mol kg^{-1} $Zn(OTf)_2$. Finally, the third type of behavior exhibited the formation of surface instabilities that were observed at the highest deposition overpotentials of -700 mV versus Zn/Zn(II) in 0.34 mol kg^{-1} $Zn(OTf)_2$ concentration and -600 mV versus Zn/Zn(II) in the 0.1 mol kg^{-1} $Zn(OTf)_2$ concentration.

A. Stepped Boulder Dominated Growth

Figure 4.15 shows the growth of Zn within a 0.1 mol kg^{-1} $Zn(OTf)_2$/BMIm OTf electrolyte at a potential of -430 mV versus Zn/Zn(II) after various amounts of charge passed in terms of Zn monolayers. After the initial deposition of 400 Zn monolayers, the zinc deposition exhibited small grains that measured between 100 to 200 nm in size. By 2000 monolayers, the Zn grains measured between 200 to 600 nm in size. The grain morphologies appeared to be similar but at a smaller size scale to the boulder morphology observed by Zn electrodeposition within aqueous KOH [13, 17].

During growth, it appeared that the larger grains covered the neighboring smaller grains as the perimeter of the larger grains grew over the smaller grains. Assuming that all the grains are growing at the same rate, a possible method of how the larger grains is eventually covering the smaller grains is shown in Figure 4.16. From the AFM images, however, it appeared that the crystallographic orientation of the Zn grains also played an important role in their growth behavior. Figure 4.17 shows the progression of two Zn grains during deposition that is highlighted by the vertical and horizontal arrows. The grain highlighted by the vertical arrow appeared to be oriented with its basal plane perpendicular to the substrate. This grain exhibited fast growth and eventually covered its smaller neighbors. A grain that appeared not to grow during deposition is highlighted by the horizontal arrow. This grain appeared to be oriented with its basal plane nearly parallel to the substrate. By 2000 Zn monolayers of charge passed, this grain was covered by faster growing neighboring grains. Therefore, growth rate appeared to be faster on the prism planes allowing for favorably oriented grains to grow at a faster rate than unfavorably oriented grains.

Figure 4.18 shows the height profile along the Zn grain after deposition of 2000 ideal Zn monolayers. The angle between the two top faces of the grain was measured to be 125° and is near the 120° expected between prism planes.

The growth of this single grain was analyzed by directly measuring the grain size on two axes. One axis measured the distance from the top and bottom basal planes and the second axis measured the width of the grain as shown in the inset figure in Figure 4.19. Figure 4.19 plots the resulting distance measurements of the grain against the amount of charge passed (ideal Zn monolayers). The perimeter of the grain grew to cover its smaller neighbors during deposition. Since the grain grew unimpeded by neighboring grains, the measured grain growth exhibited a linear relation to the amount of charge passed. In addition, the Zn grain grew faster in the direction perpendicular to the basal plane and this direction corresponded to the $\langle\bar{1}100\rangle$, $\langle\bar{1}\bar{1}20\rangle$, or $\langle 1\bar{2}10\rangle$ directions (on the prism planes). The growth rate in the basal plane direction, measured at 0.27 nm ML^{-1}, was slightly lower to the growth rate perpendicular to the basal plane that was measured at 0.35 nm ML^{-1}. Finally, the slightly lower growth rate on the basal plane of the Zn grain compared to the prism planes resulted in a consistent aspect ratio during deposition as shown in Figure 4.19.

Figure 4.20 highlights another grain that initially exhibited a high profile at 600 monolayers of deposition, but this grain was overtaken by neighboring grains with continued deposition. This particular grain was oriented with its basal plane tilted slightly in reference to the substrate. Growth of this grain was dominated on the prism planes. Step edge growth, however, was also observed on the basal plane (refer to the deflection images at 600 and 800 ML in Figure 4.20). The width of the grain was measured at various amounts of charge passed as shown in the inset of Figure 4.21. Initially, the width of the grain grows linearly with the amount of charge passed up to 1200 monolayers. With continued deposition, the growth rate slows down and this was attributed to the impeding growth of neighboring grains. Initially, the growth rate of the grain was measured at 0.30 nm ML^{-1} and this rate was comparable to other rates measured in this investigation.

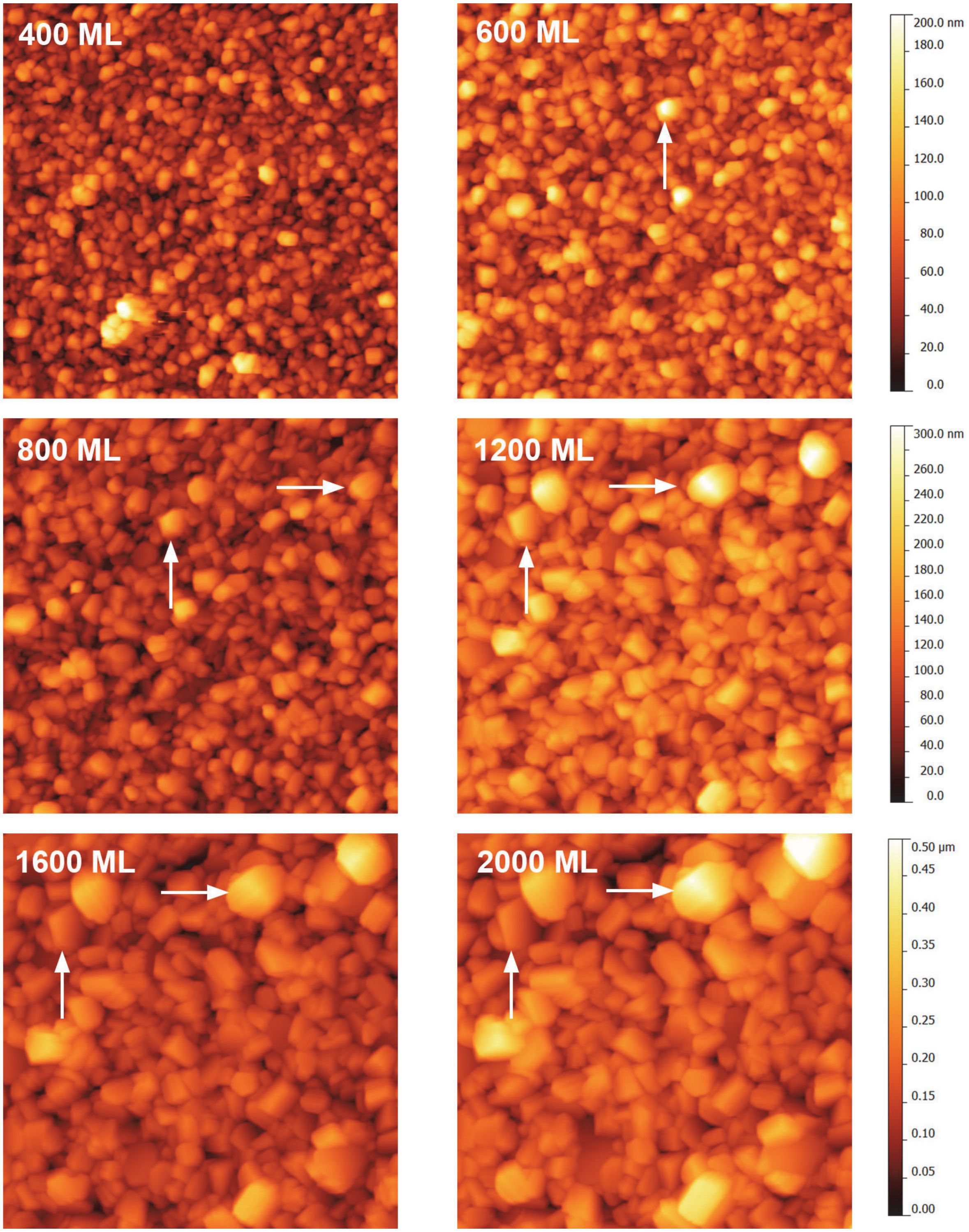

Figure 4.15. Sequential AFM images of the Zn deposition at -430 mV versus Zn/Zn(II) reference (0.1 mol kg^{-1} $Zn(OTf)_2$/BMIm OTf) after various amounts of charge passed corresponding to ideal Zn monolayers (ML). Arrows show the progression of features with continued deposition. Images are 4 µm × 4 µm.

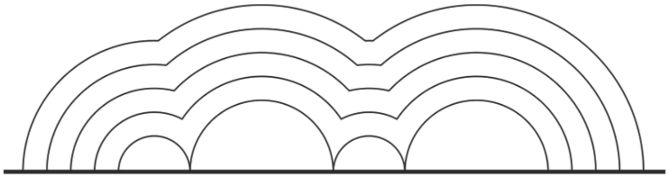

Figure 4.16. Schematic showing how larger Zn grains eventually cover smaller grains with continued deposition assuming that all the grains grow at the same rate.

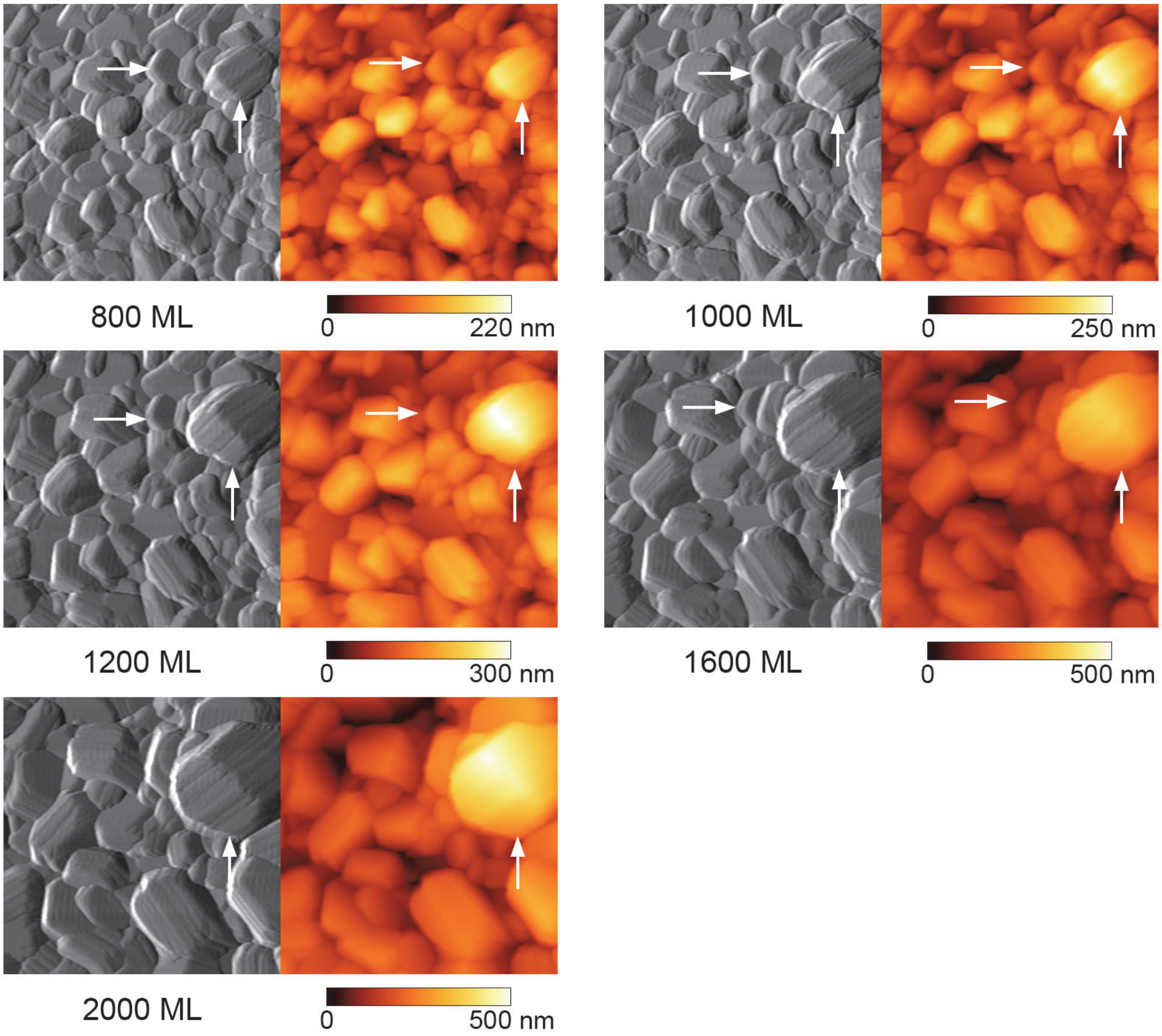

Figure 4.17. AFM image from both the deflection and height data following the growth of the Zn crystal oriented with its basal plane perpendicular to the substrate. Charge passed is noted in ideal Zn monolayers (ML). Deposition at -430 mV versus Zn/Zn(II) reference with an electrolyte concentration of 0.1 mol kg^{-1} $Zn(OTf)_2$/BMIm OTf. Images are 1.5 µm × 1.5 µm.

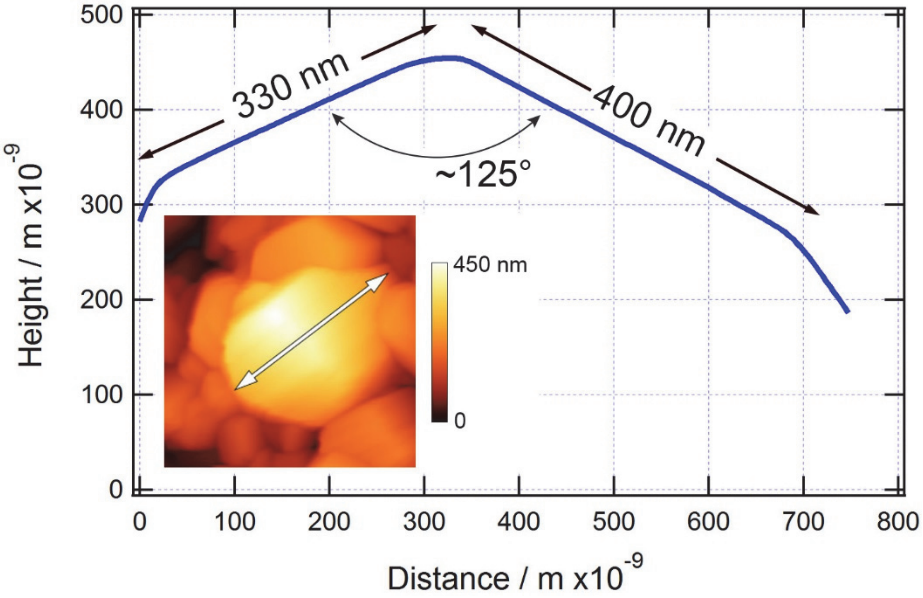

Figure 4.18. Height profile of a Zn crystal. The figure inset shows the AFM image of the Zn crystal along with the height profile line. The AFM image shows the location of the height profile line and the image is 1 μm × 1 μm.

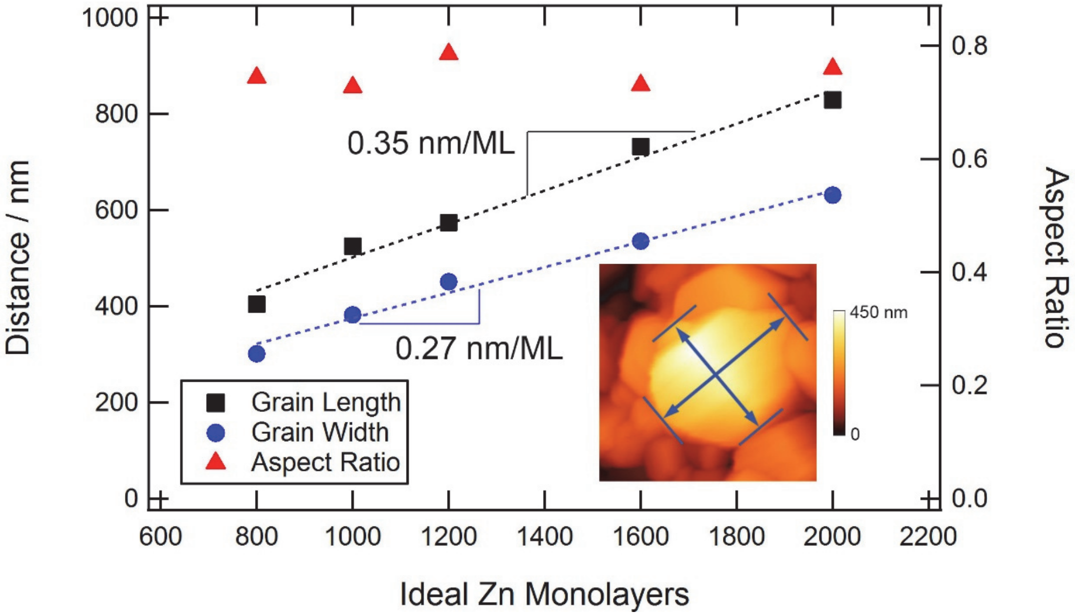

Figure 4.19. Measured width and height of a Zn crystal oriented with its basal plane perpendicular to the substrate as a function of the amount of charge passed in ideal Zn monolayers (ML). The width to height aspect ratio is plotted against the right axis. The AFM image shows where the measurements were obtained and the image is 1 μm × 1 μm.

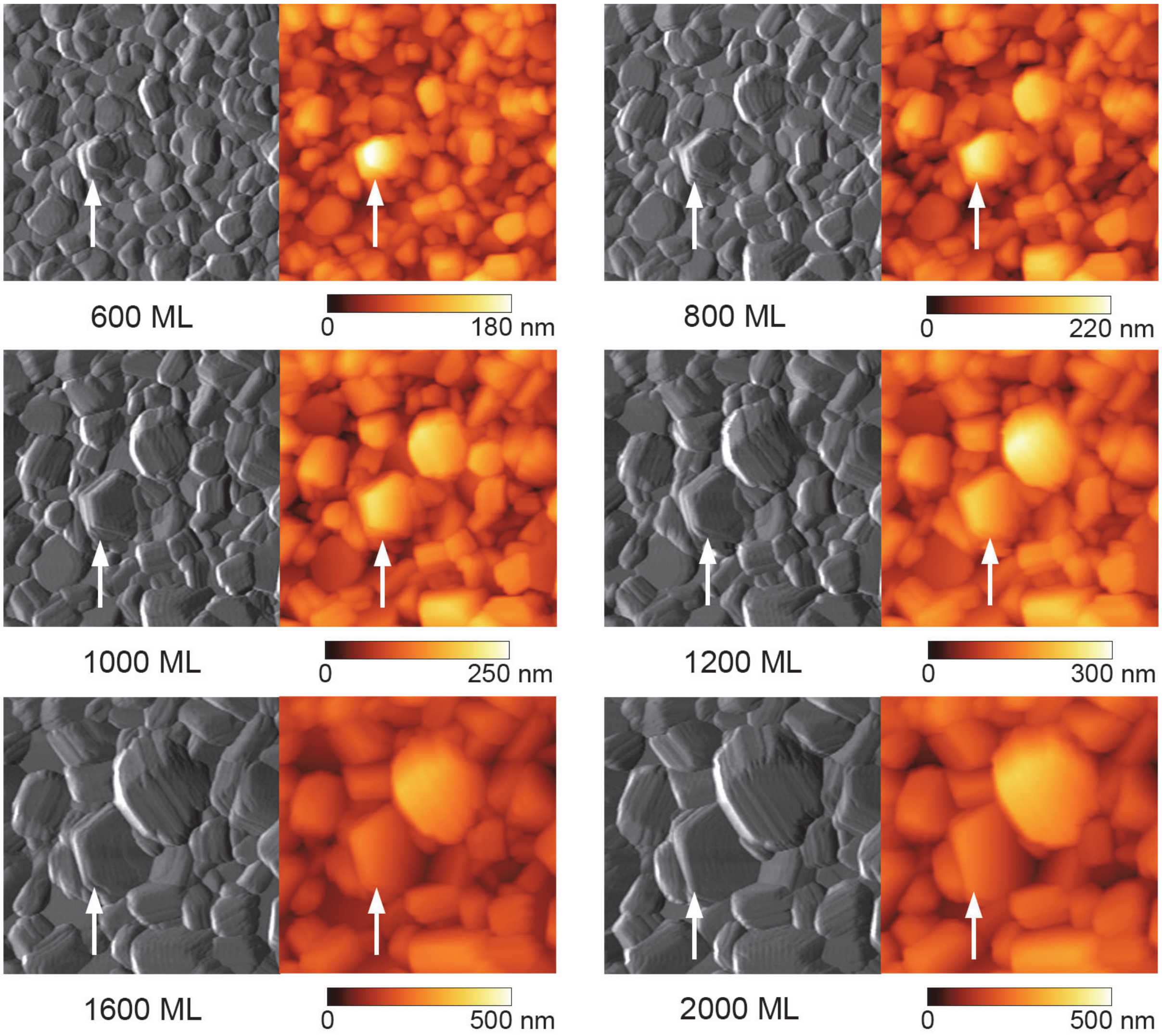

Figure 4.20. AFM image from both the deflection and height data following the growth of the Zn crystal oriented with its basal plane at a slight angle in relation to the substrate. Charge passed is noted in ideal Zn monolayers (ML). Deposition at -430 mV versus Zn/Zn(II) reference with an electrolyte concentration of 0.1 mol kg^{-1} $Zn(OTf)_2$/BMIm OTf. Images are 1.5 µm × 1.5 µm.

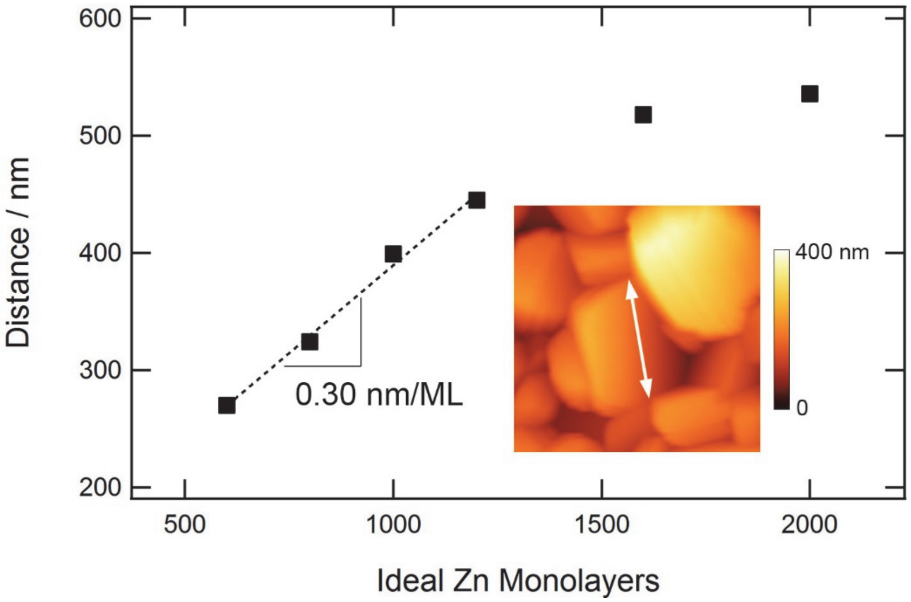

Figure 4.21. Measured width of a Zn crystal oriented with its basal plane a slight angle to the substrate as a function of the amount of charge passed in ideal Zn monolayers (ML). The width to height aspect ratio is plotted against the right axis. The AFM image shows where the measurement was obtained and the image is 1 µm × 1 µm.

B. Selected Grain Orientation Dominated Growth

Three in-situ analyses resulted in similar Zn deposition growth behavior and these analyses were conducted within 0.34 mol kg^{-1} Zn(OTf)$_2$ concentrations at potentiostatic deposition of -400, -500 and -650 mV versus Zn/Zn(II).

Figure 4.22 shows the progression of Zn morphology with continued electrodeposition within the ionic liquid electrolyte during deposition at a constant voltage of -400 mV versus the Zn/Zn(II) reference. After a charge is passed corresponding to 400 Zn monolayers, the substrate exhibited small Zn grains. These grains grew with continued deposition and smaller grains were continually being covered by larger neighboring grains. At 1200 monolayers, the grains appeared to be randomly oriented by measuring the angle of the basal plane in relation to the substrate for individual grains. After 1600 monolayers of deposition, the grains oriented with their basal plane at a high angle in relation to the substrate appeared to have grown at a faster rate. With continued deposition, these angled grains dominated growth and covered the neighboring grains until grains with an angled orientation largely dominated the surface. An example of this growth dominance is highlighted by a horizontal arrow in Figure 4.22 that shows the growth progression of a grain oriented with its basal plane parallel to the substrate surface. With continued deposition, this grain starts to be covered by the neighboring grains with tilted orientations as shown after 2000 and 2800 monolayers of Zn deposition.

The growth of the Zn deposition at -500 mV versus the Zn/Zn(II) is shown in Figure 4.23. As with the Zn deposition conducted at the higher potential of -400 mV versus Zn/Zn(II), the initial deposition appeared to consist of small randomly oriented grains after 400 monolayers if charge passed. With continued deposition, grains oriented with their basal planes parallel to the substrate were covered by grains with the basal plane tilted in relation to the substrate. A feature highlighted by a horizontal arrow shows the progression of a grain with its basal plane tilted and this grain grew to cover its neighboring grains after 2800 Zn monolayers of deposition.

The growth of Zn at a lower potential of -650 mV is shown in Figure 4.24. As observed at the higher potentials, the initial deposition of 400 monolayers exhibited small, randomly oriented grains. By 1200 monolayers, it was observed that grains with their basal plane tilted in relation to the substrate eventually covered the neighboring grains. The tilted grains continued to grow and increase their perimeters until these grains largely dominated the surface by 2800 monolayers.

Figure 4.25 shows a schematic of the possible mechanism of how the grains oriented with their basal plane at a high angle in relation to the substrate allowed them to eventually cover neighboring grains. Growth appeared to be dominated in directions perpendicular to the basal plane on the prism planes. Grains oriented with their basal plane parallel to the substrate grew at the same rate as angled grains on the prism planes, but growth of these parallel oriented grains was quickly impeded by their neighbors. In contrast, the orientation of the angled grains allowed them to grow over their neighbors as shown in the schematic in Figure 4.25.

Figure 4.26 shows the growth of the Zn grain oriented with its basal plane parallel to the substrate during deposition at -400 mV versus Zn/Zn(II). The grain appeared to be growing primarily on the prism planes. Step edge growth was also observed on the basal plane but this growth appeared slower than the growth on the prism planes. This Zn grain impinged on neighboring grains after 1600 monolayers of charge passed impeding its growth. By 2800 monolayers, most of the surface of the grain was covered by its neighboring grains. Figure 4.27 shows how the diameter of the grain as measured across its basal surface grew with the amount of charge passed. The grain growth appeared to be linearly dependent on the amount of charge passed and the growth in the diameter of the grain was measured to be 0.26 nm per monolayer.Figure 4.28 shows a zoomed in progression of the zinc morphology evolution during deposition at -500 mV versus Zn/Zn(II). During this deposition, nucleation continually occurred on the Zn surface. The horizontal arrows in Figure 4.28 highlights a parent grain and, at 600 ML, a new grain nucleates on the basal plane of the parent grain. This new grain appeared to be oriented with its basal plane parallel to the underlying grain. With continued deposition, this nucleated grain evolved from a rounded morphology to a faceted morphology by 1000 ML.

The vertical arrow in Figure 4.28 at 600 ML highlights another nucleation site. After 800 ML, a new Zn grain was observed. The parent grain was oriented with its basal plane parallel to the substrate. The nucleated grain, however, appeared to be oriented at an angle in relation to the substrate. This orientation allowed for it to grow a rapid rate in a direction perpendicular to the substrate as shown after 1600, 2000, and 2400 ML.

Figure 4.29 shows the measurement of the diameter for grain nucleated on a parent grain at 600, 800, and 1000 Zn monolayers of charge passed (ML). The nucleated grain grew with a linear dependence to the amount of charge passed (ideal Zn monolayers). The grain growth was measured at 0.275 nm per monolayer and is within the same range as measured for other Zn grains during deposition at -400 mV versus Zn/Zn(II).

All three conditions analyzed in this section exhibited similar morphological development with zinc deposition. During electrodeposition, grains that grew unimpeded by its neighbors exhibited a growth rate that was linearly dependent on the amount of charge passed. In addition, the number of grains per unit area continued to decrease during electrodeposition since smaller grains were continuously being covered by larger grains. Although the grains were growing at about the same rate, the faster growth rate on the prism planes allowed for grains oriented with their basal planes tilted to the substrate to grow and eventually cover their neighbors. Furthermore, grains exhibiting a tilted basal plane ended up dominating the surface by 2000 monolayers of charge passed for each of the three deposition conditions.

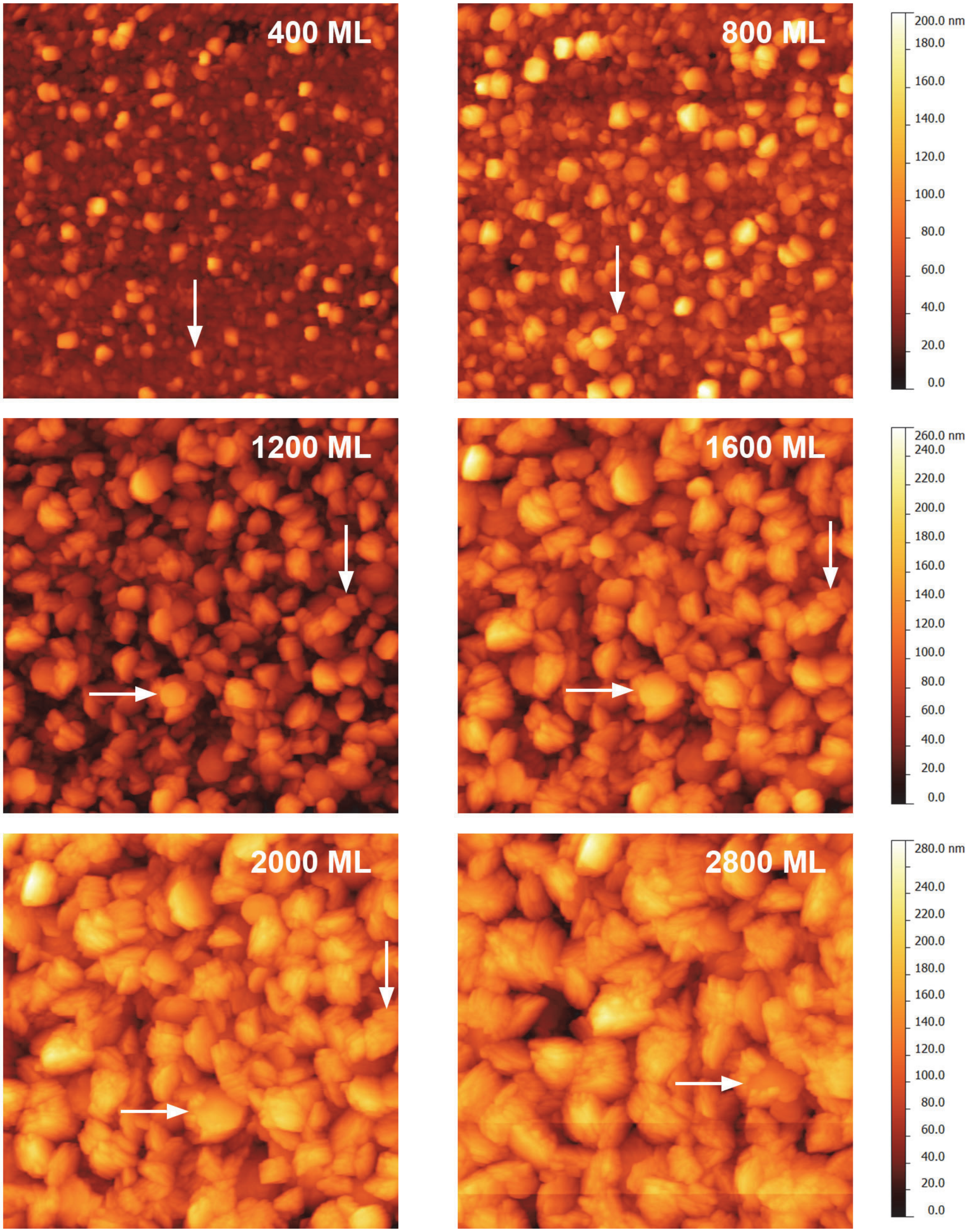

Figure 4.22. Sequential AFM images of the Zn deposition at -400 mV versus Zn/Zn(II) reference (0.34 mol kg^{-1} $Zn(OTf)_2$/BMIm OTf) after various amounts of charge passed corresponding to ideal Zn monolayers (ML). Arrows show the progression of features with continued deposition. Images are 4 µm × 4 µm.

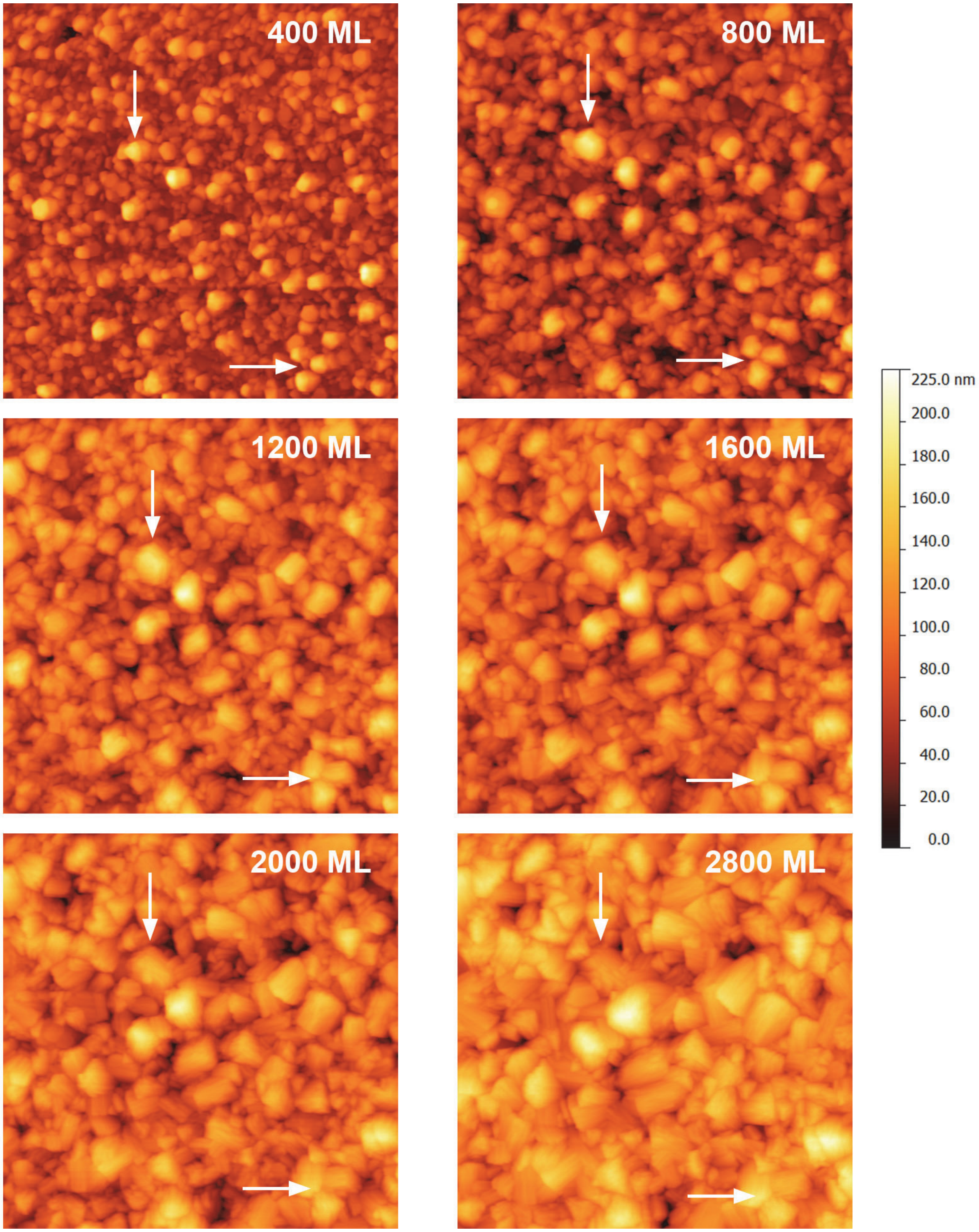

Figure 4.23. Sequential AFM images of the Zn deposition at -500 mV versus Zn/Zn(II) reference (0.34 mol kg^{-1} $Zn(OTf)_2$/BMIm OTf) after various amounts of charge passed corresponding to ideal Zn monolayers (ML). Arrows show the progression of features with continued deposition. Images are 4 μm × 4 μm.

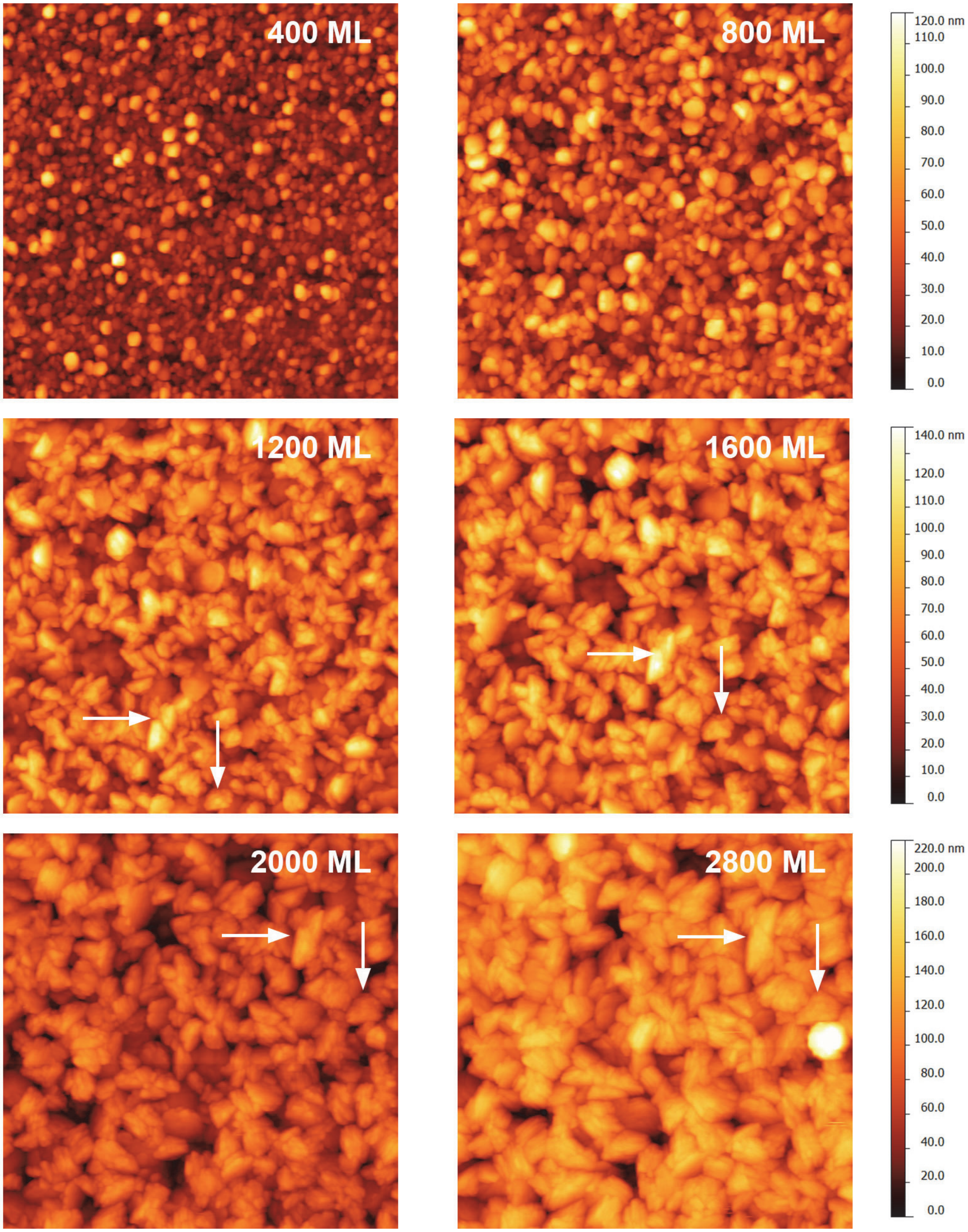

Figure 4.24. Sequential AFM images of the Zn deposition at -650 mV versus Zn/Zn(II) reference (0.34 mol kg^{-1} Zn(OTf)$_2$/BMIm OTf) after various amounts of charge passed corresponding to ideal Zn monolayers (ML). Arrows show the progression of features with continued deposition. Images are 4 µm × 4 µm.

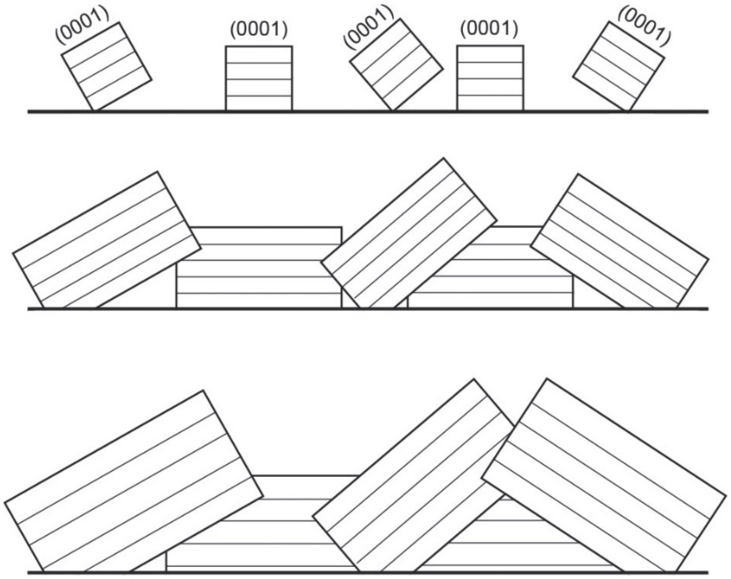

Figure 4.25. Schematic showing how Zn grains oriented with their basal plane at an angle in relation to the substrate will allow these grain to grow and cover neighboring grains that are oriented with their basal plane parallel to the substrate.

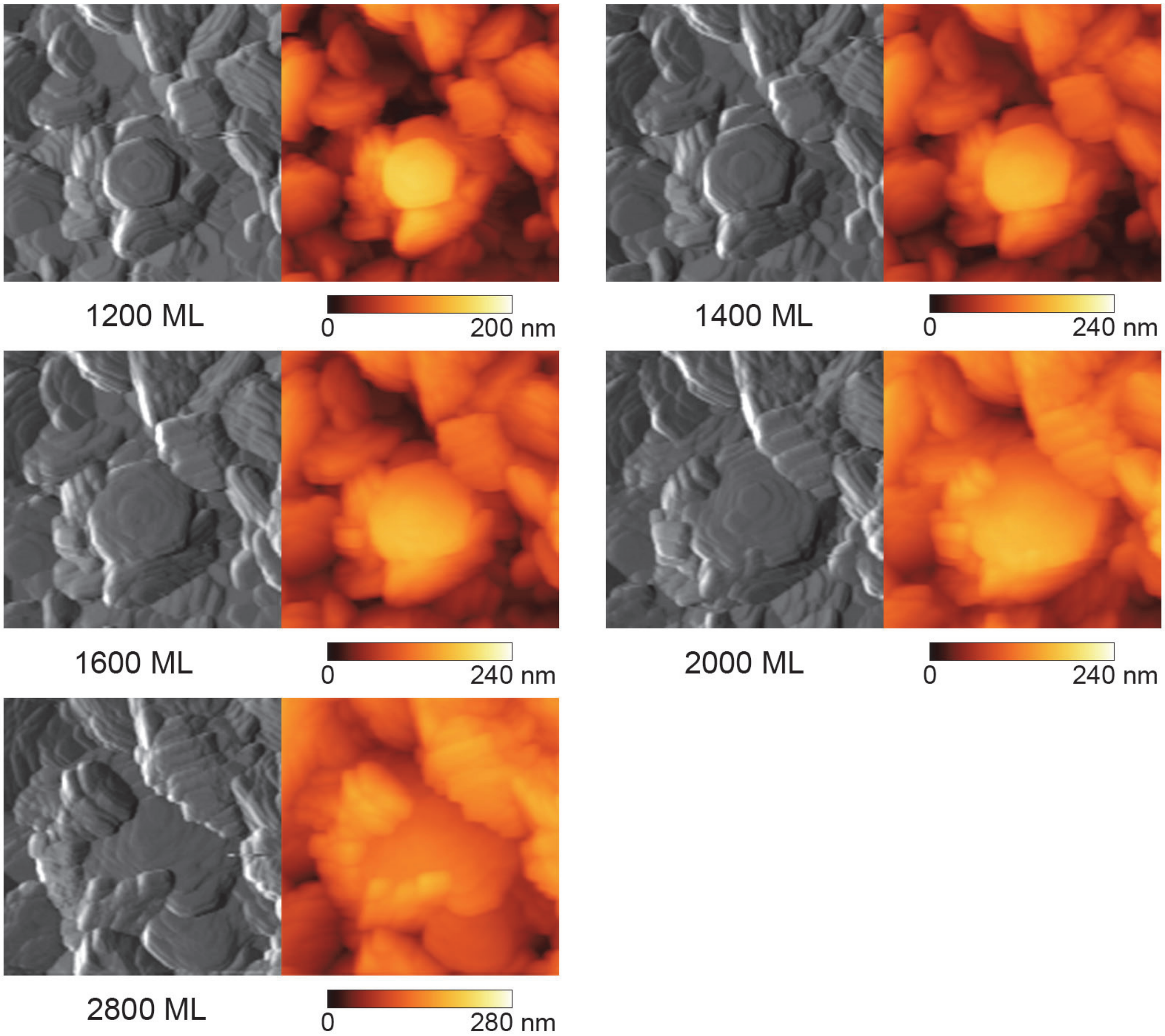

Figure 4.26. AFM image from both the deflection and height data following the growth of the Zn crystal oriented with its basal plane oriented parallel to the substrate. Charge passed is noted in ideal Zn monolayers (ML). Deposition at -400 mV versus Zn/Zn(II) reference with an electrolyte concentration of 0.34 mol kg^{-1} Zn(OTf)$_2$/BMIm OTf. Images are 1 μm × 1 μm.

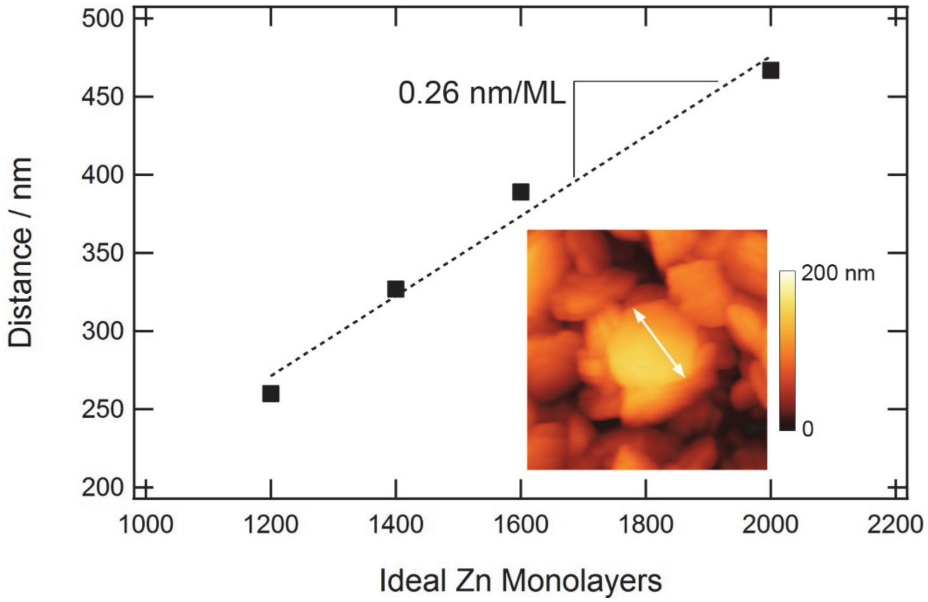

Figure 4.27. Measured width of a Zn crystal oriented with its basal plane oriented parallel to the substrate as a function of the amount of charge passed in ideal Zn monolayers (ML). The width to height aspect ratio is plotted against the right axis. The AFM image shows where the measurement was obtained and the image is 1 µm × 1 µm.

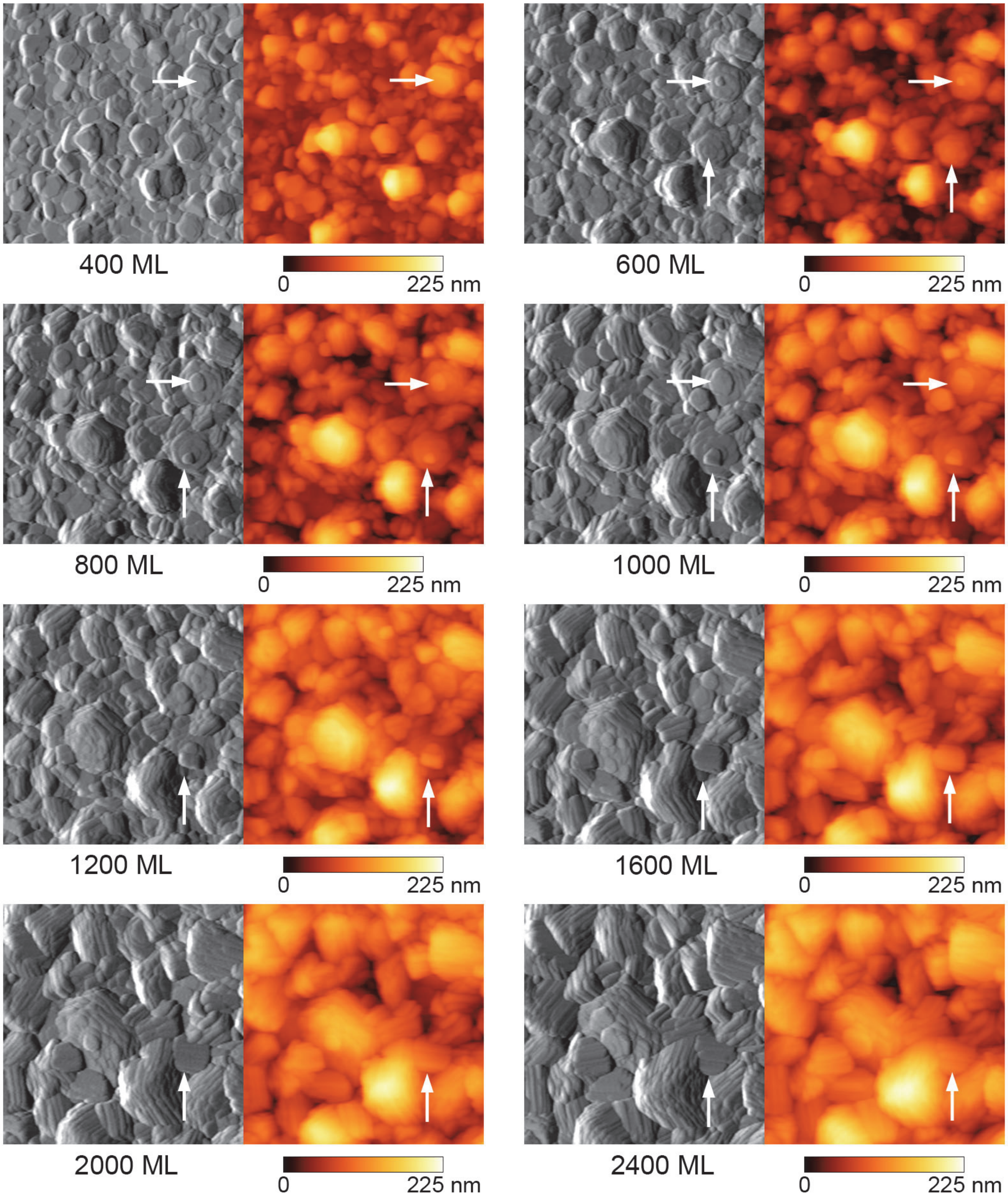

Figure 4.28. Deflection and corresponding height AFM images following the progression in Zn deposition morphology by the amount of charge passed in ideal Zn monolayers (ML). Deposition was at -500 mV versus Zn/Zn(II) reference with an electrolyte concentration of 0.34 mol kg^{-1} Zn(OTf)$_2$/BMIm OTf. Images are 1.5 µm × 1.5 µm.

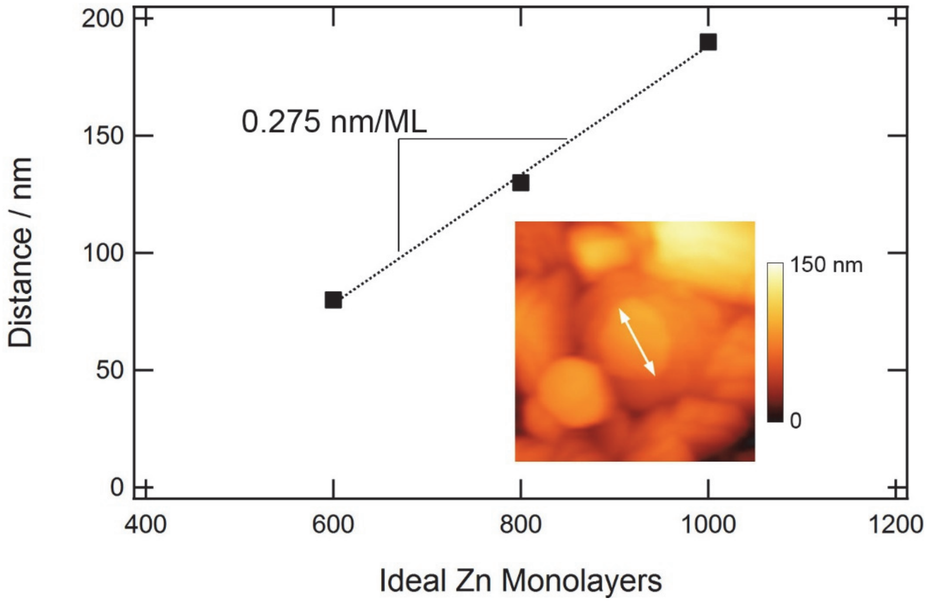

Figure 4.29. Measured width of a Zn crystal that nucleated on top of a parent crystal as a function of the amount of charge passed in ideal Zn monolayers (ML). The AFM image shows where the measurement was obtained the image is 500 nm × 500 nm.

C. Development of Surface Instabilities

The AFM images of the zinc deposition at -600 mV versus Zn/Zn(II) within the 0.1 mol kg^{-1} Zn(OTf)$_2$ concentration are shown in Figure 4.30. Surface instabilities developed quickly during this in-situ analysis and by 600 monolayers of ideal Zn monolayers, the surface exhibited large islands. These islands measured over 300 nm in height by 600 monolayers of charge passed. The arrows in Figure 4.30 highlights the progression of two islands. At 200 monolayers, the precursor zinc grains to the islands appeared to exhibit similar sizes to neighboring grains. After 400 monolayers, the features grew noticeably larger than the neighboring grains. The sharp features of the islands were beyond the capability of the AFM tip to resolve fully. Furthermore, the smearing observed from the AFM data of the island features points to the fact that these features were not firmly attached to the substrate. The island features appeared to consist of small, randomly oriented zinc crystals that formed an agglomerate.

Figure 4.31 shows a similar development of instabilities that was observed during zinc deposition at -700 mV versus Zn/Zn(I) within the 0.34 mol kg^{-1} Zn(OTf)$_2$ concentration. As with the previous experiment, high features were observed after 400 ML that measured over 200 nm in height and these features grew rapidly after 600 and 800 monolayers of charge passed. By 800 monolayers, the features measured 500 nm in height. In addition, the islands were composed of an agglomerate of small, randomly oriented Zn grains.

The surface instabilities observed with these two in-situ experiments may be the result of the high deposition overpotential. This high overpotential may have compounded edge effects locally on the Zn grains. Zinc grains that exhibited a slightly higher height than their neighboring grains may have experienced a different potential gradient that allowed for localized nucleation and growth at these locations. As the islands grew, these potential gradients enhanced resulting in faster islands growth. It was hypothesized that these island features could be the precursor of dendritic structures if the deposition was allowed to continue.

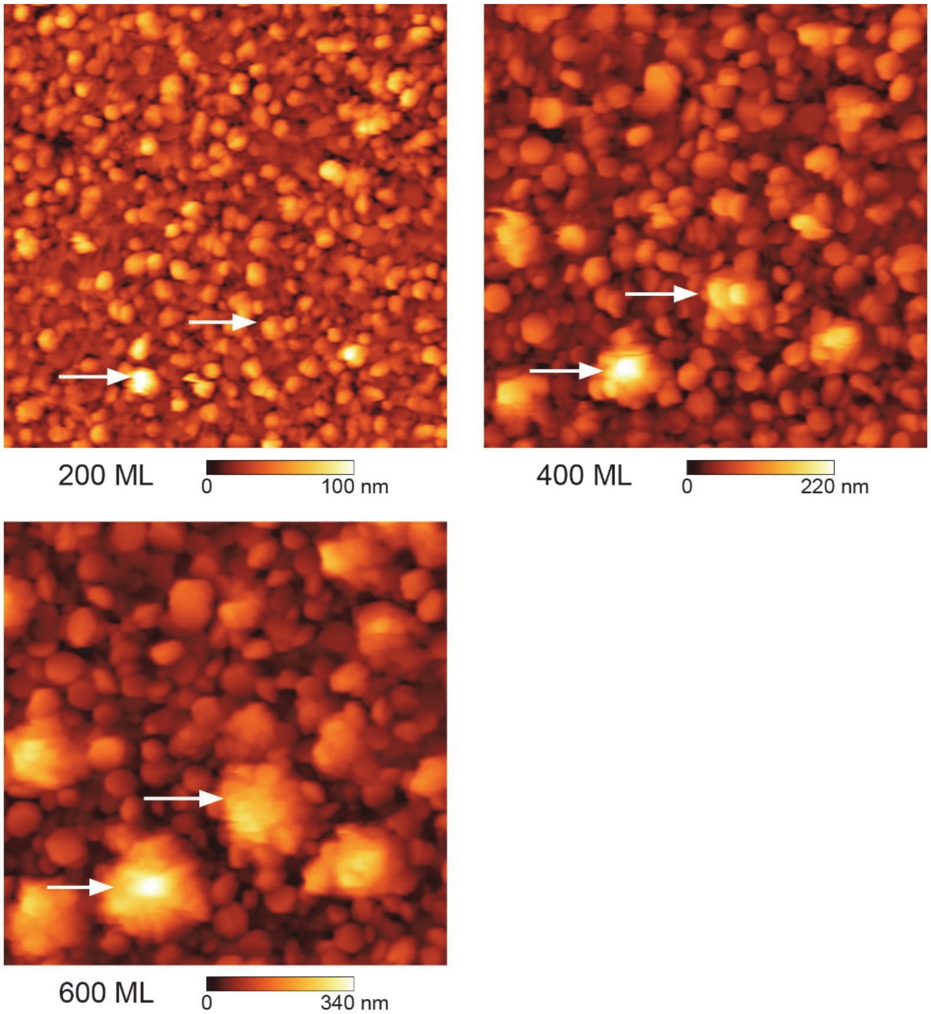

Figure 4.30. Sequential AFM images of the Zn deposition at -600 mV versus Zn/Zn(II) reference within 0.1 mol kg^{-1} $Zn(OTf)_2$/BMIm OTf after 200, 400, and 600 ideal Zn monolayers (ML) of charge passed. Arrows show the progression of features with continued deposition. Images are 2 μm × 2 μm.

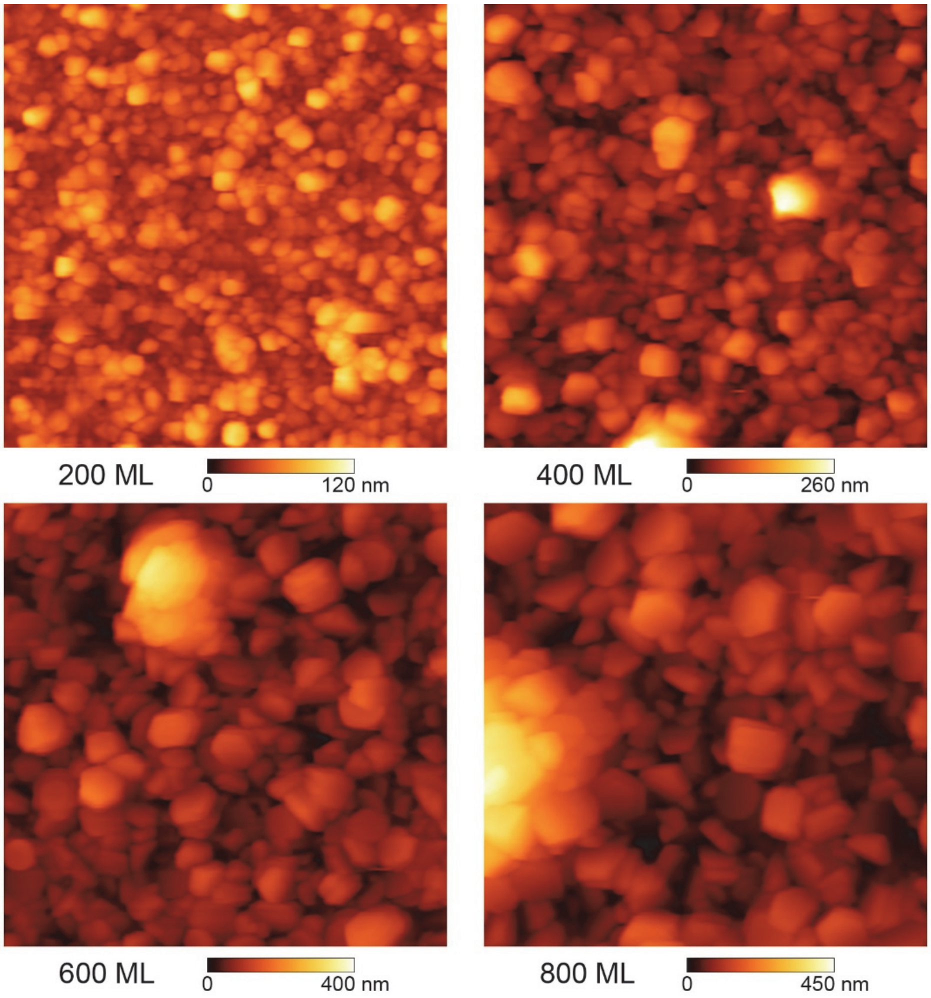

Figure 4.31. Sequential AFM images of the Zn deposition at -700 mV versus Zn/Zn(II) reference within 0.34 mol kg^{-1} Zn(OTf)$_2$/BMIm OTf after 200, 400, 600, and 800 ideal Zn monolayers (ML) of charge passed. Arrows show the progression of features with continued deposition. Images are 2 μm × 2 μm.

D. Comparison of Deposition Morphologies

Figure 4.32 shows the comparison of all six in-situ investigations after a charge passed corresponding to 400 monolayers of Zn. For this deposition, there appeared to be little difference among the various deposition conditions. The Zn grains appeared to exhibit a similar size for each condition. The grains were randomly oriented for each condition and some grains exhibited faceting.

Figure 4.33 compares the different deposition conditions after 1200 monolayers of deposition. There was a noticeable difference between the depositions conducted within the 0.1 mol kg^{-1} concentration compared to the three other depositions at 0.34 mol kg^{-1}. The deposition at 0.1 mol kg^{-1} exhibited a boulder like morphology. Each of the depositions within the 0.34 mol kg^{-1} concentration exhibited both large grains, but also small features were observed. These smaller Zn morphologies appeared to fill in the voids between the larger grains.

Figure 4.34 shows the Zn morphology for these same deposition conditions after 2000 monolayers of charge passed. In contrast to Figure 4.33, the morphological differences between the depositions within the 0.1 mol kg^{-1} concentration compared to the depositions within 0.34 mol kg^{-1} concentrations were more pronounced. The 0.1 mol kg^{-1} exhibited large boulders that were randomly oriented. The depositions conducted within the 0.34 mol kg^{-1} concentration all exhibited both large grains along with small features in between the small grains. It appeared that the growth of the smaller features (either from the preferred growth direction or from the continued nucleation of Zn), allowed a more even surface topography to develop and grow.

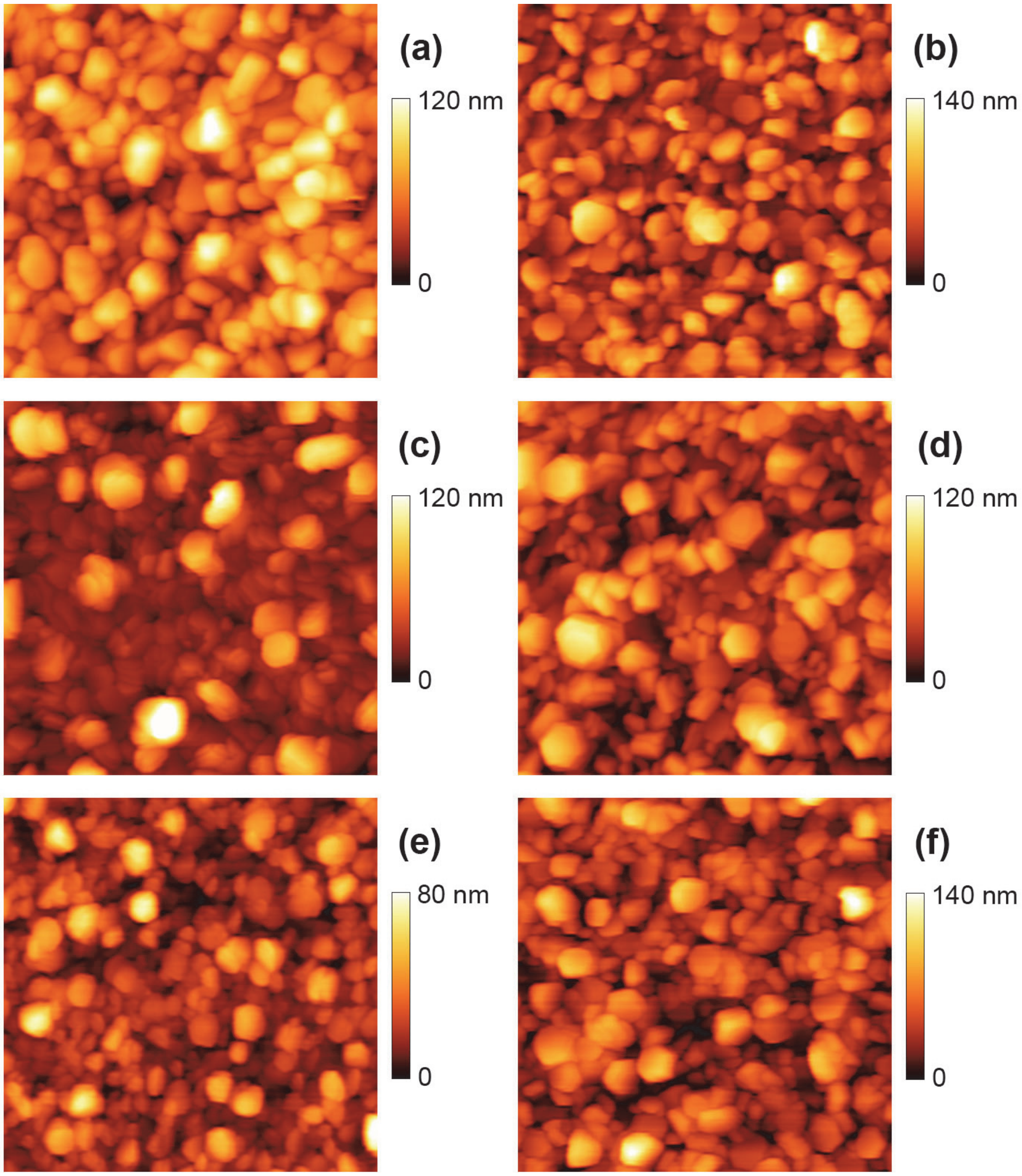

Figure 4.32. AFM height images after 400 Zn monolayers of charge passed. Images (a) and (b) were deposited within 0.1 mol kg^{-1} Zn(OTf)$_2$/BMIm OTf at -430 mV and -600 mV vs. Zn/Zn(II) respectively. Images (c), (d), (e), (f) were deposited within 0.34 mol kg^{-1} Zn(OTf)$_2$/BMIm OTf at -400 mV, -500 mV, -650 mV, and -700 mV vs. Zn/Zn(II) respectively. Images are 1.5 μm × 1.5 μm.

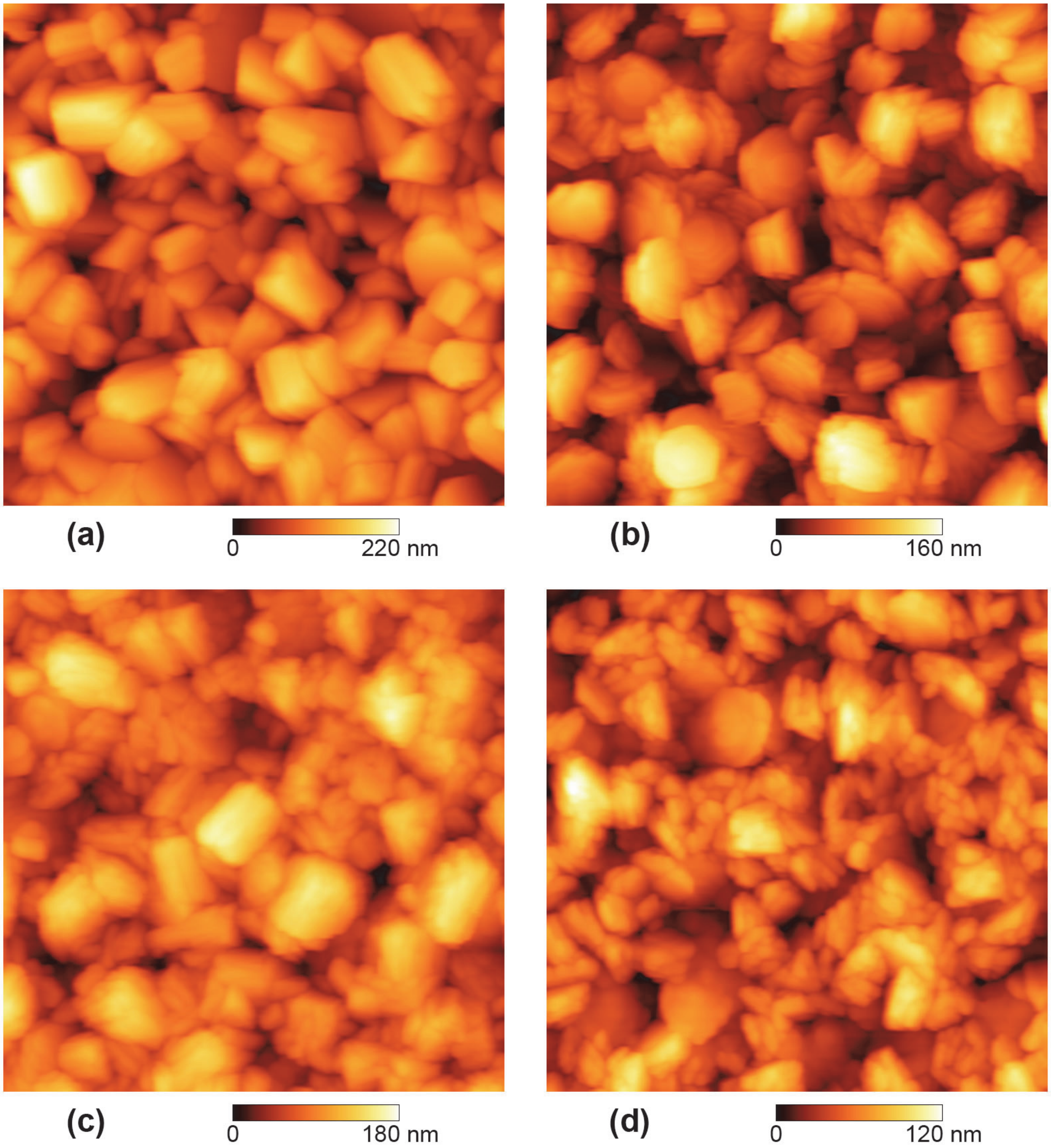

Figure 4.33. AFM height images after 1200 Zn monolayers of charge passed. Image (a) was deposited within 0.1 mol kg^{-1} Zn(OTf)$_2$/BMIm OTf at -430 mV vs. Zn/Zn(II). Images (b), (c), and (d) were deposited within 0.34 mol kg^{-1} Zn(OTf)$_2$/BMIm OTf at -430 mV, -500 mV, and -650 mV vs. Zn/Zn(II) respectively. Images are 2 µm × 2 µm.

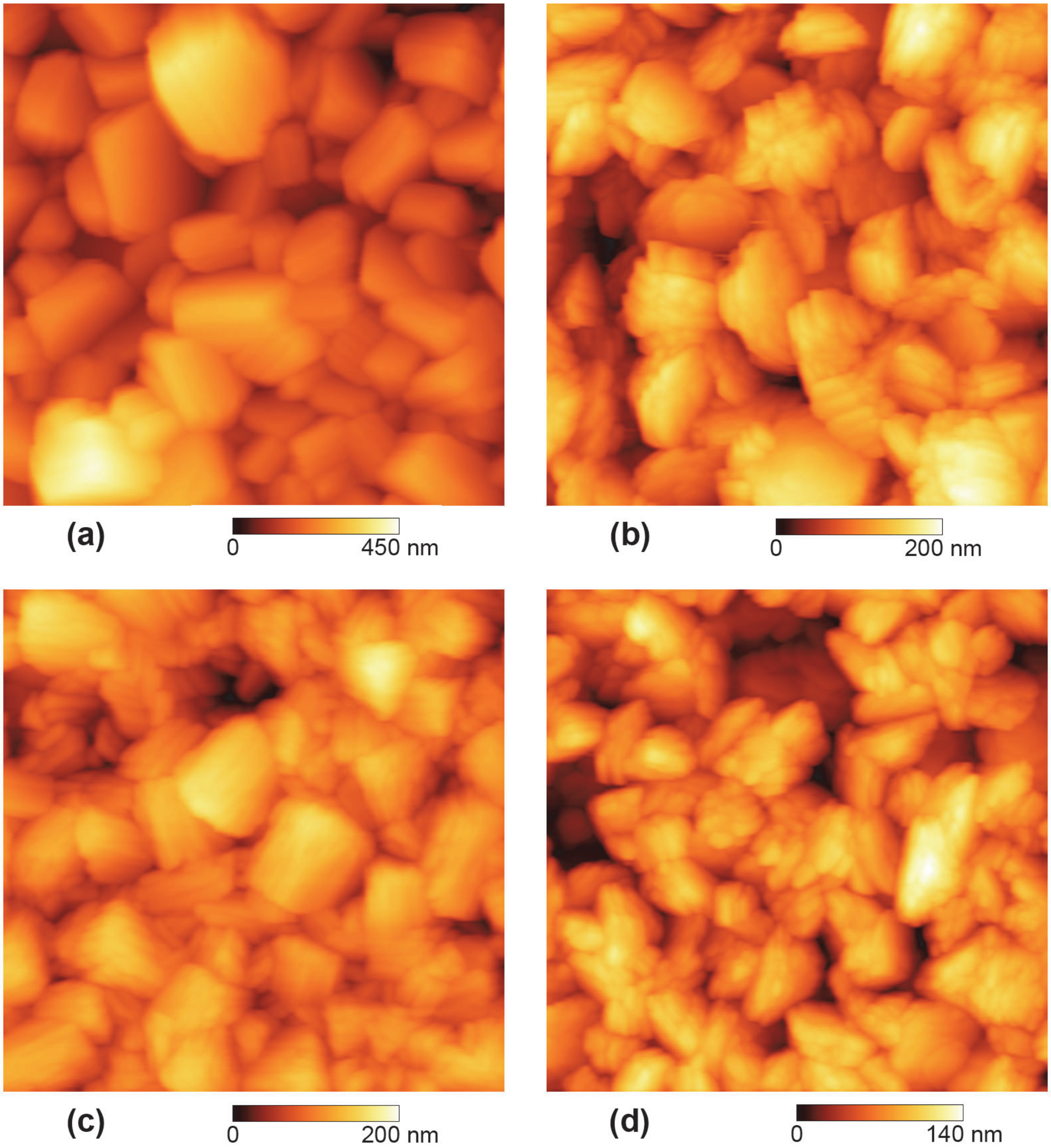

Figure 4.34. AFM height images after 2000 Zn monolayers of charge passed. Image (a) was deposited within 0.1 mol kg^{-1} Zn(OTf)$_2$/BMIm OTf at -430 mV vs. Zn/Zn(II). Images (b), (c), and (d) were deposited within 0.34 mol kg^{-1} Zn(OTf)$_2$/BMIm OTf at -430 mV, -500 mV, and -650 mV vs. Zn/Zn(II) respectively. Images are 2 µm × 2 µm.

4.4.4. Ex-Situ Electron Microscopy

Selected samples were removed after deposition of 2800 Zn monolayers of charge passed for ex-situ analysis by SEM. Figure 4.35 compares the SEM image obtained ex-situ to the AFM image obtained in-situ for the Zn deposition within 0.34 mol kg^{-1} Zn(OTf)$_2$/BMIm OTf at -500 mV versus Zn/Zn(II) after 2800 Zn monolayers of charge passed. The morphology observed by the AFM appeared to exhibit similar morphologies as observed by ex-situ SEM. This confirmed that the AFM was able to resolve the zinc morphology correctly with minimal tip convolution. The small tip convolution that existed appeared to round off the corners of the grain edges slightly as compared to grain edges shown in the SEM image. In addition, the AFM tip appeared to be able to correctly resolve deep features.

The deposition behavior observed by ex-situ SEM was homogenous across the electrode surface. Figure 4.36 shows a zoom out of the Zn morphology as observed by the SEM to show the homogenous deposition morphology over a larger field of view. Furthermore, large instabilities or dendritic structures were not observed on the surface.

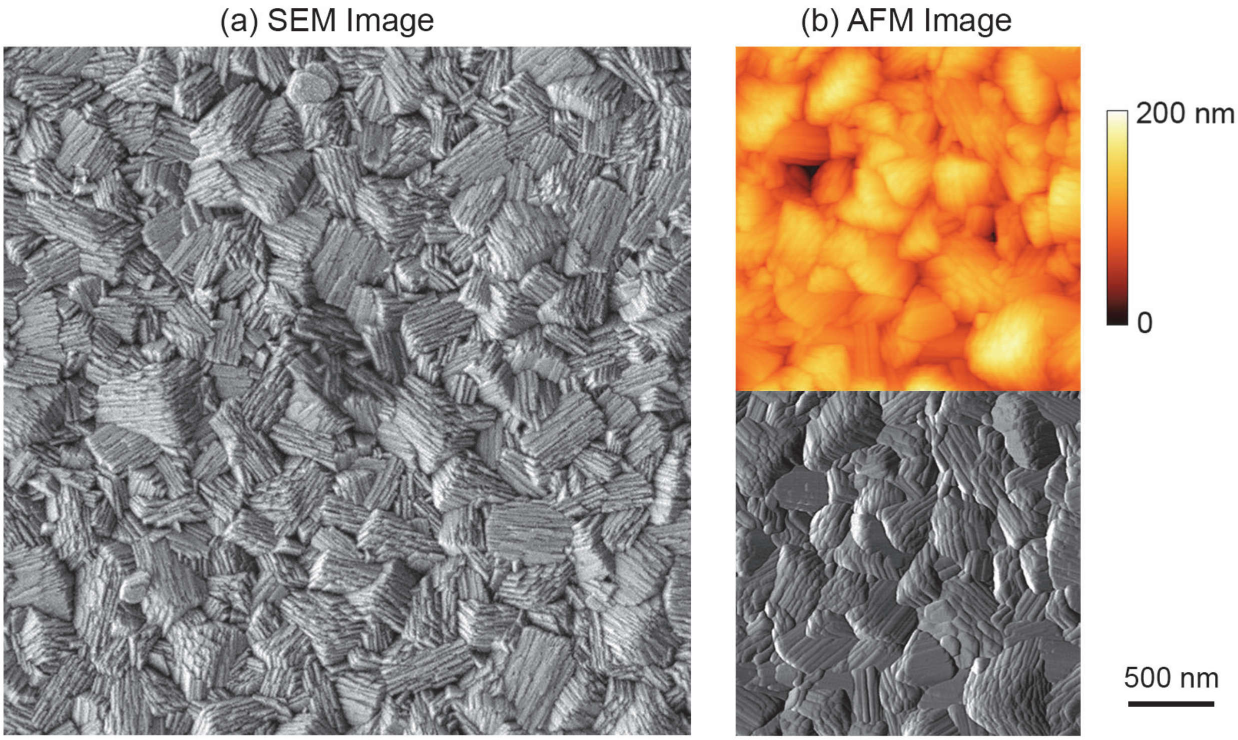

Figure 4.35. SEM image (a) obtained ex-situ compared to the AFM image (b) obtained in-situ from both the height and deflection data after deposition within 0.34 mol kg^{-1} Zn(OTf)$_2$/BMIm OTf at -500 mV versus Zn/Zn(II) for 2800 Zn monolayers. AFM images are 2 µm × 2 µm.

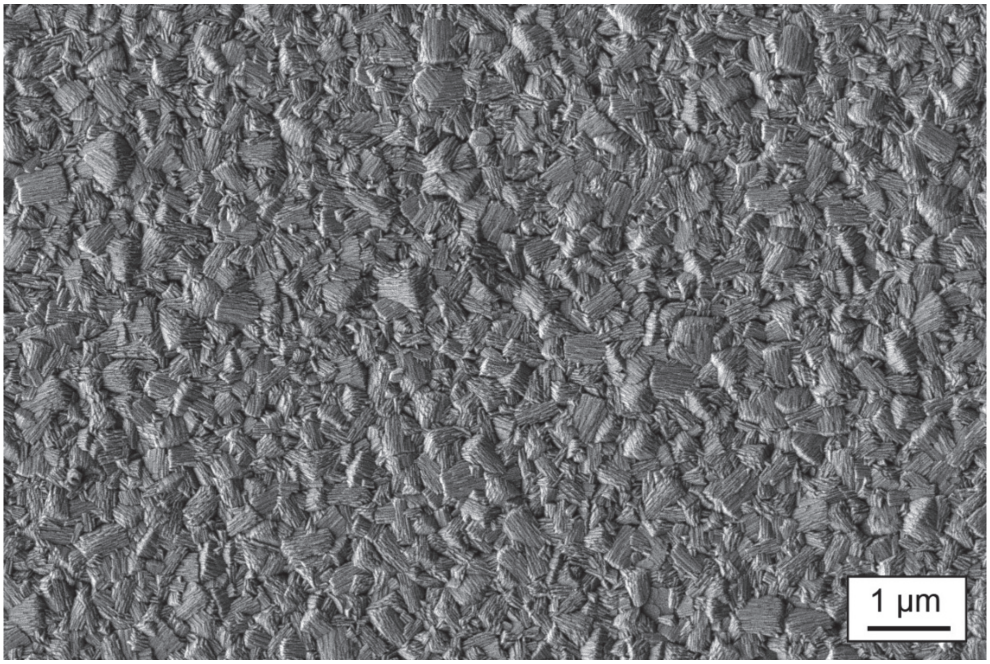

Figure 4.36. SEM image obtained ex-situ of the Zn deposition after 2800 Zn monolayers of charge passed within 0.34 mol kg^{-1} $Zn(OTf)_2$/BMIm OTf at -500 mV versus Zn/Zn(II).

4.4.5. Data Analysis

This section discusses the data analysis of the AFM data obtained after various amounts of charge passed in terms of ideal Zn monolayers for each of the conditions analyzed. Data analysis was conducted on the following deposition trials:

- A → -430 mV versus Zn/Zn(II) within 0.1 mol kg^{-1} $Zn(OTf)_2$/BMIm OTf
- C → -400 mV versus Zn/Zn(II) within 0.34 mol kg^{-1} $Zn(OTf)_2$/BMIm OTf
- D → -500 mV versus Zn/Zn(II) within 0.34 mol kg^{-1} $Zn(OTf)_2$/BMIm OTf
- E → -650mV versus Zn/Zn(II) within 0.34 mol kg^{-1} $Zn(OTf)_2$/BMIm OTf

The first section discusses how the RMS roughness changed with the amount of charge passed. The second section details the analysis utilizing the height difference correlation function. Finally, the third section compares height difference correlation behavior to electrodeposition behaviors observed by other investigations.

A. RMS Roughness

The surface roughness RMS during the in-situ deposition of zinc was calculated from the AFM data obtained. Figure 4.37 plots the RMS values for the various deposition conditions analyzed against the amount of charge passed in terms of ideal Zn monolayers. The deposition within 0.1 mol kg^{-1} $Zn(OTf)_2$ concentration at -430 mV versus Zn/Zn(II) resulted in a continually increasing roughness from a RMS value of 17 nm after 200 monolayers of deposition to a RMS of 71 nm after 2000 monolayers of deposition. The deposition conducted within the 0.34 mol kg^{-1} Zn(OTf)$_2$ concentration exhibited slower increases in the RMS roughness. The deposition conducted at -500 mV versus Zn/Zn(II) reached a maximum RMS roughness of 28 nm at 1200 monolayers and the RMS remained constant up to 2800 monolayers. Deposition at -400 mV versus Zn/Zn(II) also appeared to reach a maximum RMS roughness of 39 nm after 2400 monolayers of deposition and the roughness slightly decreased to 37 nm after 2800 monolayers. Deposition within 0.34 mol kg^{-1} concentration at -650 mV versus Zn/Zn(II) appeared to continuously increase in roughness but at a slower rate than the other conditions. The RMS roughness was measured at 9 nm after 200 monolayers and it increased to 30 nm after 2800 monolayers of deposition.

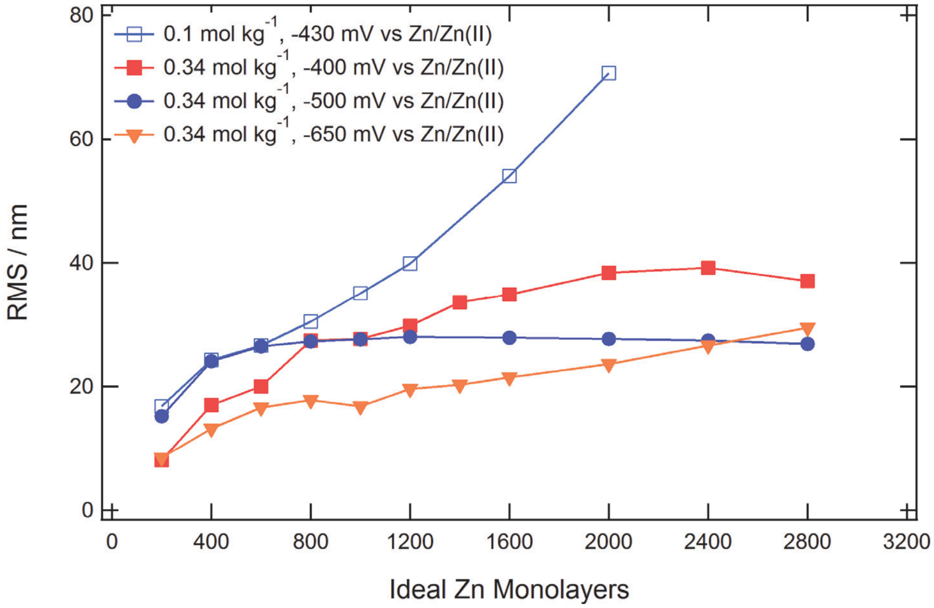

Figure 4.37. Roughness surface measurements (RMS) measured in-situ by AFM analysis for the various deposition trials versus the amount of charge passed in terms of Zn monolayers.

B. Height Difference Correlation Function

The height difference correlation obtained from the AFM data during Zn deposition within the 0.1 mol kg^{-1} Zn(OTf)$_2$ concentration at -430 mV versus Zn/Zn(II) after various amounts of charge passed (Zn monolayers) is shown in Figure 4.38. For each deposition, the height difference correlation dependence was nearly constant for large distances, x. For small x, the log of the correlation exhibits a linear dependence to the log of x and indicates that the surface scales with x^H. The Hurst exponent, H, was constant within the measurement error with a value of 0.9.

During deposition, the system appeared to follow normal scaling as shown in Figure 4.39. The correlation for small distances (local height correlation at 40 nm) remained constant with increasing Zn deposition. Within the saturated region, the root mean square difference of the saturated surface increased with the amount of deposition. From the slope of the best fit line, the saturated σ increased at a rate of 0.03 nm per monolayer

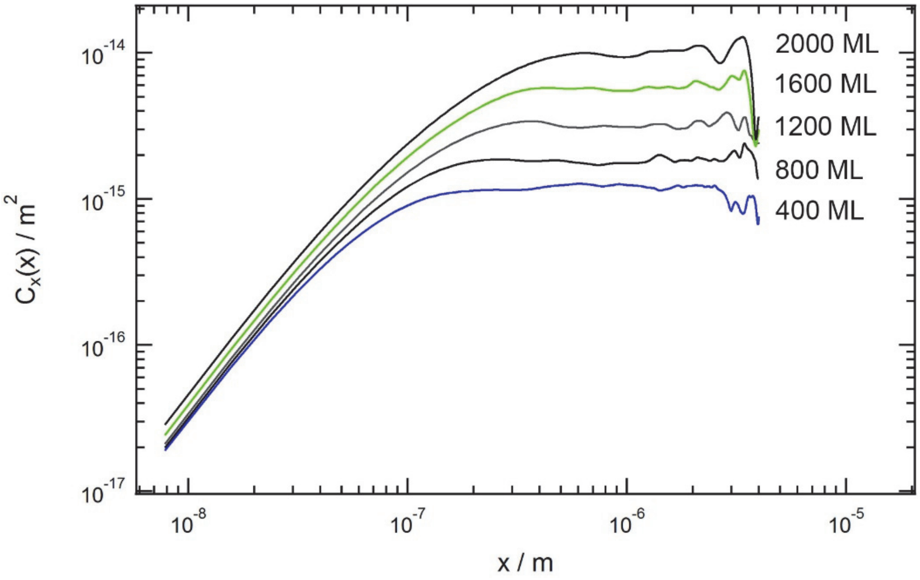

Figure 4.38. Selected height difference correlations measured from AFM data obtained during the deposition of Zn within 0.1 mol kg^{-1} Zn(OTf)$_2$/BMIm OTf at -430 mV versus Zn/Zn(II).

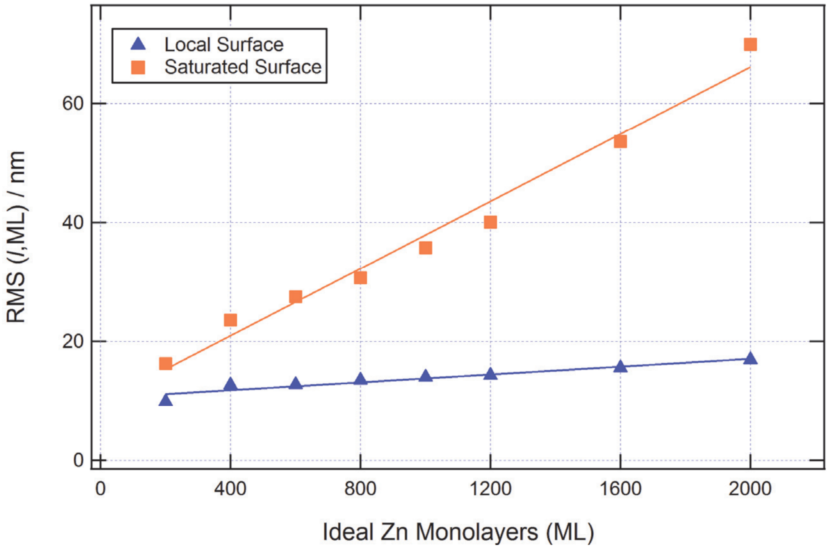

Figure 4.39. Local surface height difference correlation (for x = 40 nm) and the saturated surface height difference correlation versus the amount of charge passed in terms of ideal Zn monolayers for deposition of Zn within 0.1 mol kg^{-1} Zn(OTf)$_2$/BMIm OTf at -430 mV versus Zn/Zn(II).

The height difference correlation obtained at the higher concentration of 0.34 mol kg^{-1} Zn(OTf)$_2$ at a deposition potential of -400 mV versus Zn/Zn(II) is shown in Figure 4.40. The height difference correlation initially increased after 400 monolayers of deposition and then it appeared to remain constant up to 2800 monolayers. The scaling behavior for the small x was similar to the scaling behavior measured from the 0.1 mol kg^{-1} concentration with an average value of 0.9. The saturated correlation for high x, however, appeared to remain nearly constant with continued deposition.

The behavior of the local surface and saturated surface correlation during deposition is shown in Figure 4.41. Within the saturated region, the root mean square of the height difference initially increases with the amount of charge passed up to 1600 monolayers. The correlation at the local scale, however, remained constant with continued deposition. The system can be described as following anomalous scaling up to 800 monolayers of charge passed. Between 800 and 1600 monolayers of charge passed, the system appeared to follow normal scaling. From 2000 to 2800 monolayers of charge passed, however, the system appeared to reach a steady state despite continued Zn deposition. Both the local and saturated correlations remained constant with continued deposition after 2000 monolayers of charge passed.

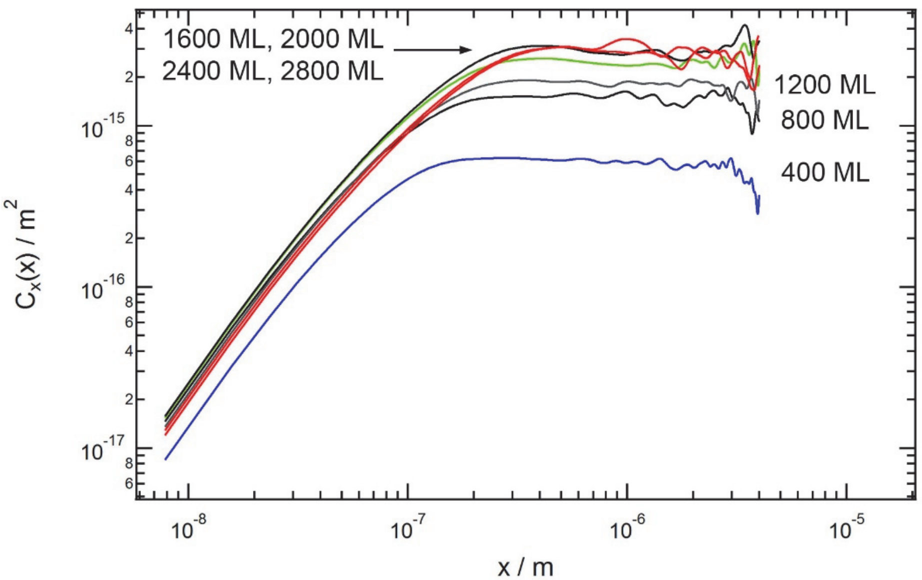

Figure 4.40. Selected height difference correlations measured from AFM data obtained during the deposition of Zn within 0.34 mol kg^{-1} Zn(OTf)$_2$/BMIm OTf at -400 mV versus Zn/Zn(II).

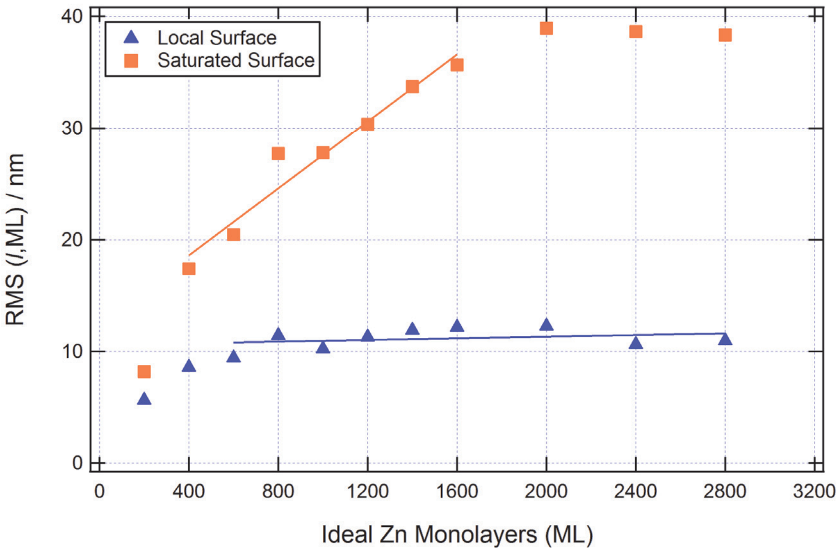

Figure 4.41. Local surface height difference correlation (for x = 40 nm) and the saturated surface height difference correlation versus the amount of charge passed in terms of ideal Zn monolayers for deposition of Zn within 0.34 mol kg^{-1} Zn(OTf)$_2$/BMIm OTf at -400 mV versus Zn/Zn(II).

Figure 4.42 shows the height difference correlation obtained from deposition within 0.34 mol kg^{-1} Zn(OTf)$_2$ at -500 mV versus Zn/Zn(II) shown. For this deposition condition, all the correlation curves except the 400 monolayers of deposition exhibited similar behavior up to 2800 monolayers. The Hurst exponent averaged at 0.9 for deposition up to 1600 monolayers, the exponent decreased slightly to 0.78 after 1600 monolayers of charge passed.

Figure 4.43 shows a plot of the root mean square of the height deviation for both the local and saturated conditions plotted against the amount of charge passed. Both the saturated and local values remained constant or slightly decreased after 600 monolayers of deposition. As with the deposition at -400 mV after 2000 monolayers of charge passed, this behavior cannot be described by either normal scaling or anomalous scaling. Instead it points to a system that has obtained a steady state by around 600 monolayers of charge passed.

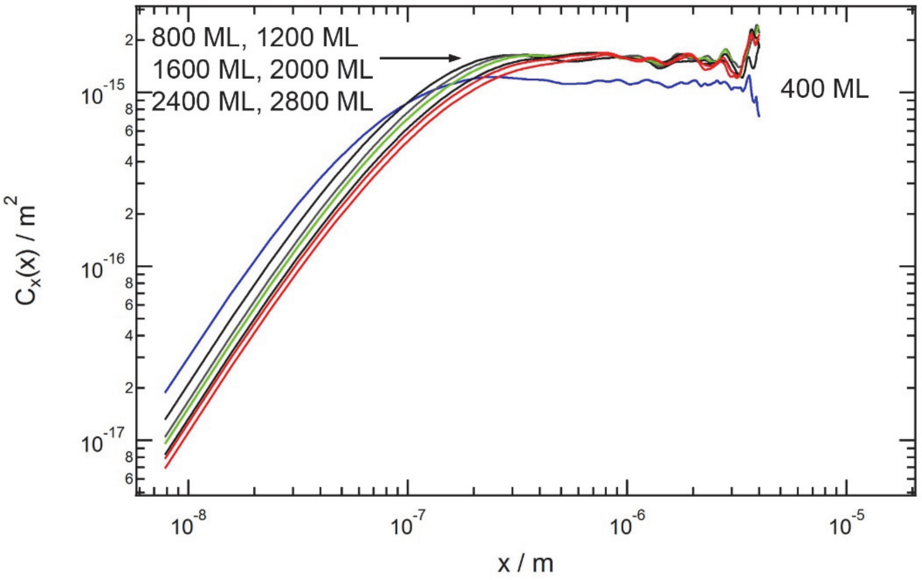

Figure 4.42. Selected height difference correlations measured from AFM data obtained during the deposition of Zn within 0.34 mol kg^{-1} $Zn(OTf)_2$/BMIm OTf at -500 mV versus Zn/Zn(II).

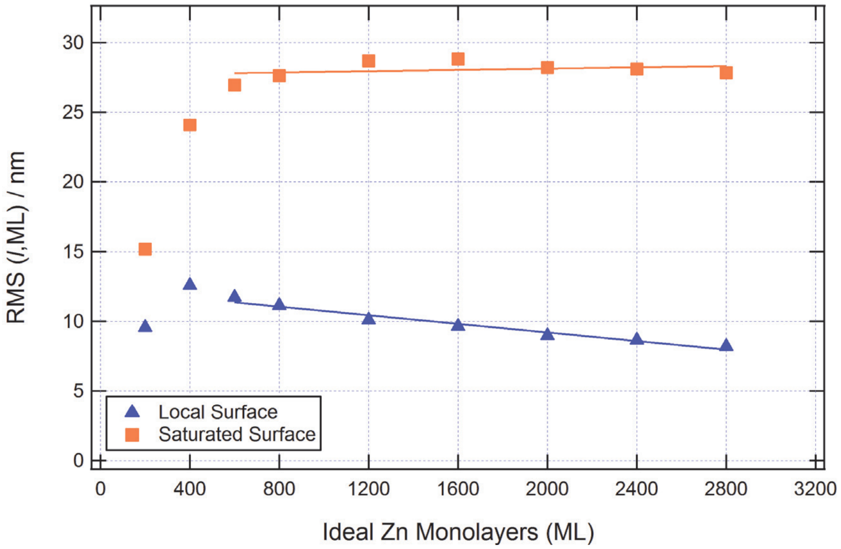

Figure 4.43. Local surface height difference correlation (for x = 40 nm) and the saturated surface height difference correlation versus the amount of charge passed in terms of ideal Zn monolayers for deposition of Zn within 0.34 mol kg^{-1} $Zn(OTf)_2$/BMIm OTf at -500 mV versus Zn/Zn(II).

Figure 4.44 plots the height difference correlation versus distance from the AFM data obtained during deposition within 0.34 mol kg^{-1} Zn(OTf)$_2$ at a constant potential of -650 mV versus Zn/Zn(II). With continued deposition, the system appeared to exhibit normal scaling throughout the deposition of Zn up to 2800 monolayers of charge passed. At low x, the height difference correlation and the Hurst exponent remained nearly constant with continued deposition at 0.9. For high x, the saturated height difference correlation appeared to increase with increasing deposition.

Figure 4.45 shows the root mean square of the height deviation for both the local and saturated conditions plotted against the amount of charge passed. Anomalous scaling was observed up to 600 monolayers of charge passed. After 600 monolayers, the saturated and local height difference correlation appeared to follow normal scaling behavior. From the slope of a best fit line to the saturated root mean square of the height deviation increased at a rate of 0.006 nm per monolayer. For comparison, this increase was about 5 times lower than the increase in σ observed during deposition in the low Zn(OTf)$_2$ concentration of 0.1 mol kg^{-1} at -430 mV versus Zn/Zn(II).

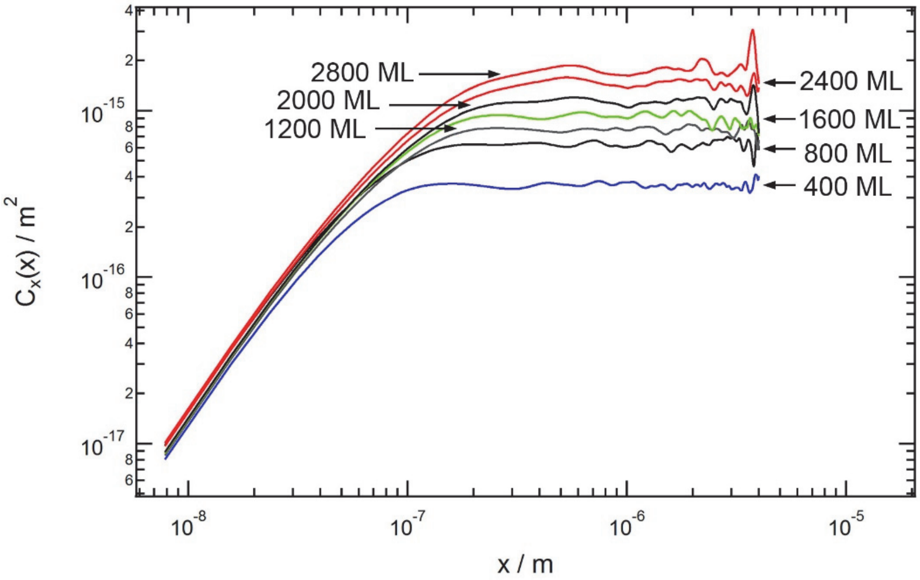

Figure 4.44. Selected height difference correlations measured from AFM data obtained during the deposition of Zn within 0.34 mol kg^{-1} Zn(OTf)$_2$/BMIm OTf at -650 mV versus Zn/Zn(II).

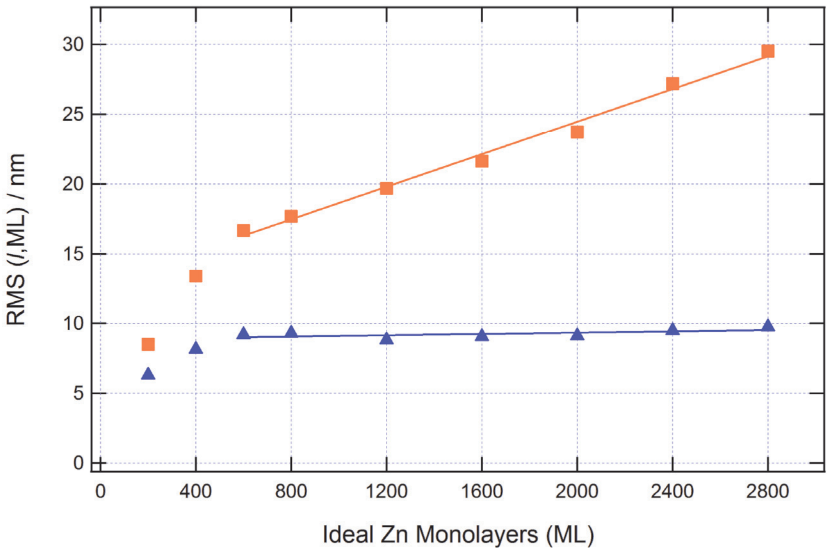

Figure 4.45. Local surface height difference correlation (for x = 40 nm) and the saturated surface height difference correlation versus the amount of charge passed in terms of ideal Zn monolayers for deposition of Zn within 0.34 mol kg^{-1} Zn(OTf)$_2$/BMIm OTf at -650 mV versus Zn/Zn(II).

In summary, the surface scaling behavior observed from the height difference correlation analysis for the different deposition trials included normal scaling, anomalous scaling and steady state (no scaling). Typically, each system exhibited anomalous scaling initially for the first 600 to 800 Zn monolayers of charge passed. For the initial deposition, this anomalous scaling indicates that Zn grains formed and grew on the Pt substrate in both height and perimeter. At around 800 monolayers of charge passed, all the deposition trials exhibited either normal scaling or steady state. The change from anomalous scaling indicates that the Zn grains have coalesced. For normal scaling, the coalesced Zn grains were growing in the height direction and the growth resulted in higher surface roughness values. When the system was exhibiting steady state growth, the surface was no longer scaling with continued deposition. Instead, the saturated surface roughness remained constant despite continued Zn growth in the height direction.

C. Correlation Length

The correlation length, L_x, calculated from the height difference correlation of the AFM data for each of the deposition conditions plotted against the amount of charge passed (Zn monolayers) is shown in Figure 4.46. The correlation length can be interpreted as the characteristic length of the system and the correlation is analogous to the average Zn grain size [39]. For each deposition condition analyzed, the correlation length increased with continued Zn deposition. This increase in length is expected since the AFM images showed that smaller grains were being covered by larger neighboring grains during deposition.

Deposition at the higher potentials resulted in similar correlation length values from 200 to 1200 monolayers of deposition. For all three depositions at the high potentials of -400, -430 and -500 mV versus Zn/Zn(II), the correlation length increased from a value of 60 nm at 200 monolayers of charge passed to a value of 130 nm after 1200 monolayers of charge passed. With continued deposition beyond 1200 monolayers, the correlation length obtained from Zn deposition within the 0.1 mol kg^{-1} increased at a significantly higher rate to a value of 230 nm after 2000 monolayers of charge passed. In contrast, the correlation length increased at the same rate for deposition within 0.34 mol kg^{-1} concentration at both -400 and -500 mV versus Zn/Zn(II).

The deposition at the lowest potential analyzed of -650 mV versus Zn/Zn(II) resulted in the smallest correlation lengths for a given amount of charge passed of all the deposition trials. It also exhibited a nearly linear growth rate with the amount of charge passed. After 200 monolayers of deposition, the correlation length was 43 nm and the correlation length increased to 150 nm after 2800 monolayers of deposition. The smaller correlation lengths measured within the -650 mV system may be the result of a higher nucleation density as predicted by the Scharifker and Hills model for electrodeposition at a higher overpotential (refer to the results presented in Section 3.3.2.)

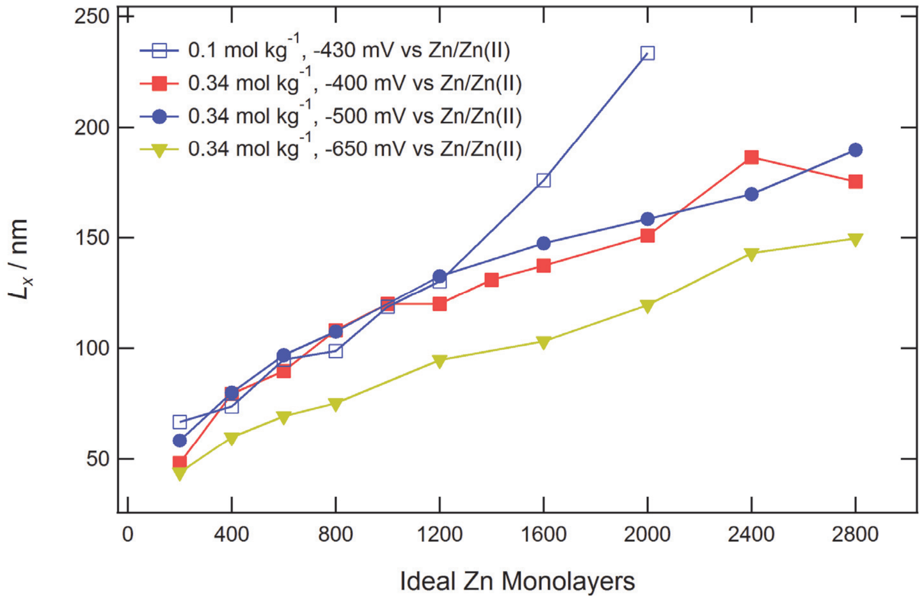

Figure 4.46. The measured correlation length, L_x, for the deposition trials as a function of the amount of charge passed in terms of Zn monolayers.

4.4.6. Comparison to Electrodeposition within KOH

Keist et al. analyzed the deposition behavior of zinc within KOH electrotypes by in-situ AFM within a similar electrochemical setup as used in this investigation. For the electrodeposition within an aqueous electrolyte, zinc deposition was conducted on a Cu substrate that was vapor deposited on a mica film to obtain a flat, polycrystalline surface. Electrodeposition was conducted within an 8.9 M KOH solution with 0.3 M ZnO. Deposition was conducted galvanostatically with a constant current of 10 mA cm^{-2}. The potential measured during deposition varied between -25 to -35 mV versus Zn/Zn(II). Deposition was conducted with galvanostatic pulses for a total charge passed of 52.3 mC cm^{-2} corresponding to 100 Zn monolayers [46].

Figure 4.47 shows the growth of Zn within the 8.9 M KOH with 0.3 M ZnO solution after various amounts of charge passed [46]. As observed with the ionic liquid deposition, after the initial deposition of 400 Zn monolayers, the zinc grains were small and appeared randomly oriented. By 1000 Zn monolayers, the Zn deposition exhibited layer-like and boulder morphology. After 3600 monolayers, the boulders dominated the morphology and the boulder sizes were over 2 μm in diameter. This type of morphology appeared to exhibit a similar morphology that is designated as boulder type by Wang et al. [13].

The deposition within the KOH electrolyte exhibited larger features with a higher change in topography than obtained within the ionic liquid electrolyte. By 2400 monolayers of charge passed, the peak to valley height of the surface topography was near 1 μm for the KOH deposition compared to about 200 nm for the ionic liquid deposition conducted at -500 mV versus Zn/Zn(II) in the 0.34 mol kg^{-1} Zn(OTf)$_2$ concentration. In addition, all grains appeared to grow at a similar rate within the KOH solution and the system did not exhibit a favored grain orientation. Similar to the grain growth observed within ionic liquid electrolyte, grain growth appeared to occur with larger grains covering the smaller neighboring grains.

Figure 4.48 shows the height difference correlation of the AFM data obtained from the Zn deposition trial within KOH [46]. The growth of the deposition appeared to follow normal scaling behavior. The Hurst exponent remained around 0.9 during the deposition. Normal scaling was also observed within the Zn deposition in the ionic liquid electrolyte at the 0.1 mol kg^{-1} Zn(OTf)$_2$ concentration. Normal scaling suggests that the local surface roughness remains constant with continued growth and the saturated surface roughness increases with continued growth. The behavior observed within the KOH deposition did not appear to reach a steady state condition as was observed with the Zn deposition in the ionic liquid at the lower potentials within the 0.34 mol kg^{-1} Zn(OTf)$_2$ concentration.

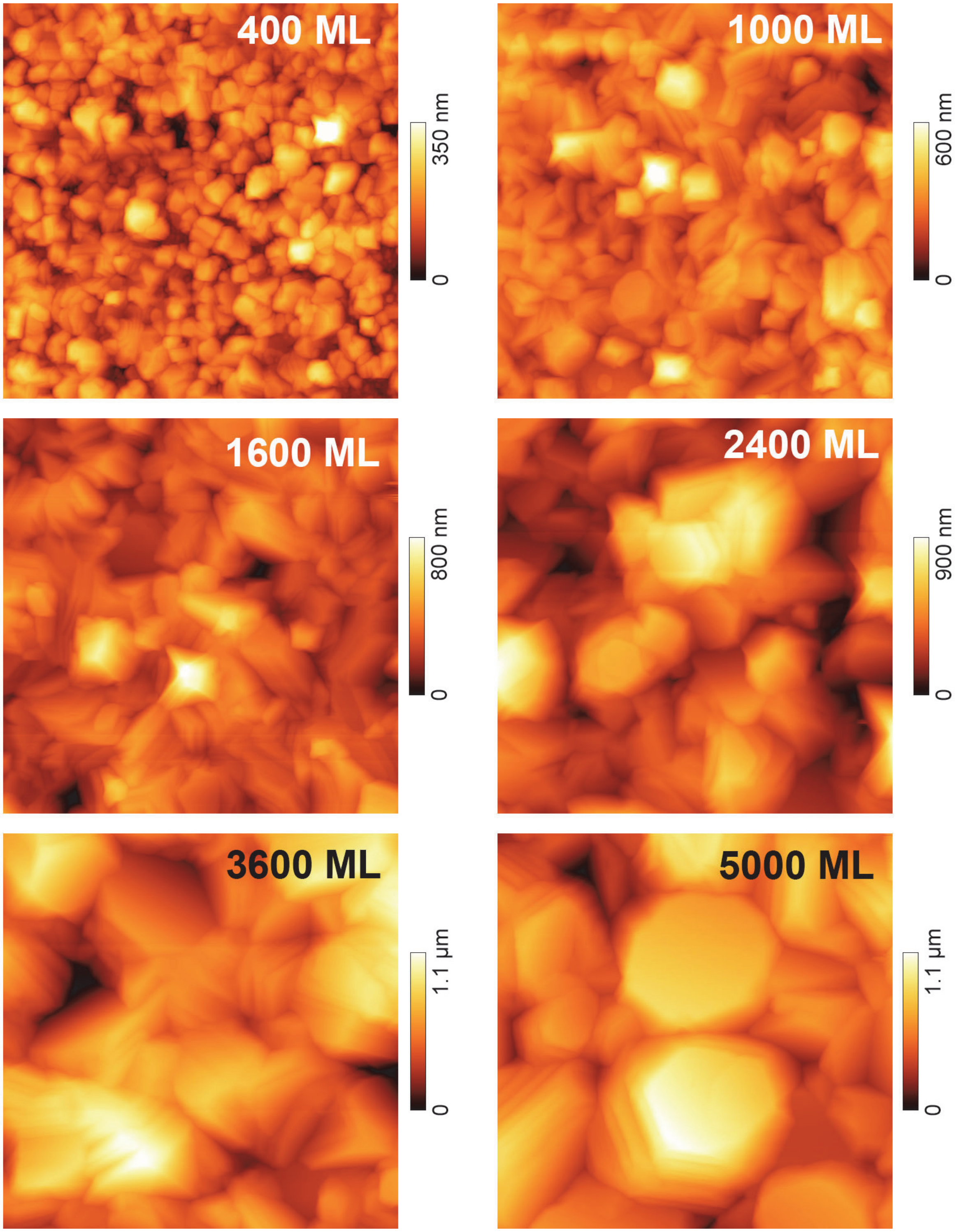

Figure 4.47. Sequential AFM images of the Zn deposition conducted galvanostatically at 10 mA cm^{-2} within 8.9 M KOH with 0.3 M ZnO after various amounts of charge passed corresponding to the ideal Zn monolayers (ML). Images are 5 µm × 5 µm [46].

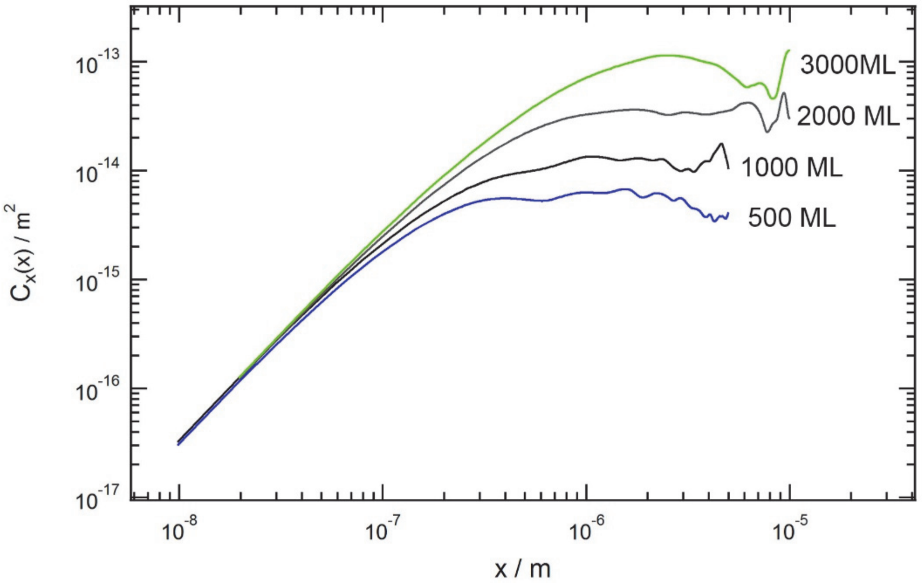

Figure 4.48. Height difference correlation measured from AFM data obtained during the deposition of Zn within 8 M KOH with 0.3 M ZnO at 10 mA cm^{-2} [46].

4.5. Conclusions

From the AFM in-situ analysis, there were three main deposition behaviors observed. The in-situ deposition at -430 mV versus Zn/Zn(II) within the 0.1 mol kg^{-1} Zn(OTf)$_2$ concentration resulted in the development and growth of stepped boulder like morphology. The depositions conducted within a 0.34 mol kg^{-1} Zn(OTf)$_2$ concentration resulted in growth that was quickly dominated by favorably oriented grains. Finally, deposition at high overpotentials resulted in the development and growth of surface instabilities.

For the deposition at -430 mV versus Zn/Zn(II) at the low concentration of 0.1 mol kg^{-1} Zn(OTf)$_2$, the stepped boulder growth obtained Zn grains that reached a size of between 200 to 500 nm after 2800 ideal Zn monolayers of charge passed. Growth of the bolder morphology was measured faster on the prism planes with a measured rate about 30% faster than the rate measured on the basal planes. The aspect ratio of the Zn grains remained nearly constant during deposition. The average grain size continuously increased with increasing deposition. The increasing grain size was the result of smaller grains continually being covered by larger neighbors during deposition.

For deposition at 0.34 mol kg^{-1} Zn(OTf)$_2$ concentration at -400, -500 and -650 mV versus Zn/Zn(II), the morphological evolution of the Zn deposition appeared to be dominated by favorably oriented Zn grains. Zn grains with their basal plane oriented parallel to the substrate were quickly covered by neighboring grains with the basal planes oriented at an angle in relation to the substrate. It appeared that growth was dominated in the $\langle\bar{1}100\rangle$, $\langle\bar{1}\bar{1}20\rangle$, or $\langle 1\bar{2}10\rangle$ directions on the prism planes. Growth on the basal plane appeared to be slower with growth observed as step edge growth. Nucleation of new Zn grains on top of parent Zn grains was also observed during the in-situ analysis.

Deposition at the lower potentials of -600 mV versus Zn/Zn(II) within a 0.1 mol kg^{-1} $Zn(OTf)_2$ concentration and at -700 mV versus Zn/Zn(II) within the 0.34 mol kg^{-1} $Zn(OTf)_2$ concentration resulted in the development of surface instabilities. These surface instabilities manifested as large agglomerate islands that were composed of small, randomly oriented Zn grains.

The RMS roughness for the deposition conducted at -430 mV versus Zn/Zn(II) within the 0.1 mol kg^{-1} concentration continuously increased with increasing Zn deposition to a value of 70 nm after 2000 Zn monolayers of charge passed. The measured roughness for the deposition within the 0.1 mol kg^{-1} concentrations at -400, -500 and -700 mV versus Zn/Zn(II) increased at a slower rate than the deposition within the 0.1 mol kg^{-1} concentration. In addition, the roughness measurement at -400 and -500 mV versus Zn/Zn(II) appeared to reach a steady state with continued deposition. After 2800 Zn monolayers of charge passed, the RMS roughness for the three trials within the 0.34 mol kg^{-1} concentration was between 25 and 40 nm.

From the height difference correlation analyses, the scaling factor of the Zn deposition was nearly constant at 0.9 throughout the deposition for each of the in-situ trials. The scaling behavior, therefore, appeared to be not affected by either concentration or the deposition overpotential.

From the height difference correlation, anomalous scaling, normal scaling and steady state were observed for the Zn deposition growth. Anomalous scaling behavior was observed for each of the deposition trials for the first 200 to 800 Zn monolayers of charge passed. This indicated that the Zn grains have not coalesced and were growing in both height and perimeter. The anomalous scaling changed to either normal scaling or steady state. This change indicated that the Zn grains have coalesced. Coalescence occurred between 400 to 800 monolayers of charge passed for each of the deposition trials.

From the height difference correlation analysis, the deposition at -430 mV versus Zn/Zn(II) within the 0.1 mol kg^{-1} concentration exhibited normal scaling behavior with continued deposition after 400 monolayers of charge passed. For the -430 mV deposition, the saturated surface roughness continued to increase with increasing Zn deposition. In contrast, the local surface roughness remained constant with increasing Zn deposition. Similar normal scaling behavior was observed for deposition at -650 mV within the 0.34 mol kg^{-1} concentration. In contrast, the deposition at -400 mV and -500 mV within the 0.34 mol kg^{-1} reached a steady state condition during deposition.

From all the in-situ trials, the correlation length measured from the height difference correlation exhibited growth with continued Zn deposition. The correlation length grew at a faster rate for the depositions conducted at a higher potential of -400, -430, and -500 mV versus Zn/Zn(II) than measured at -650 mV versus Zn/Zn(II). After 1200 Zn monolayers of charge passed for deposition within the 0.1 mol kg^{-1} concentration, the correlation length increased at a rate that was twice as fast as measured for deposition up to 1200 Zn monolayers of charge passed.

Finally, the features sizes were significantly smaller for the Zn deposition within the ionic liquid electrolyte compared the morphologies obtained after deposition within an aqueous KOH electrolyte. In addition, the Zn deposition within the ionic liquid electrolyte exhibited steady state behavior where the saturated surface roughness remained constant with Zn growth under certain deposition conditions. A steady state behavior was not observed in the Zn growth within the KOH electrolyte [46]. Instead, this system exhibited normal scaling behavior where the saturated surface roughness continually increased with Zn growth.

5. In-Situ Electrochemical Ultra-Small-Angle X-Ray Scattering

In-situ analysis of zinc deposition by atomic force microscopy (AFM) has inherent disadvantages. Foremost, the AFM is only capable of scanning a small area of the substrate that is typically on the order of microns. Second, interactions between the AFM tip and the substrate surface may alter the deposition characteristics or physically damage the deposited material. The AFM tip can also shield the substrate surface from the electric field. Finally, AFM imaging is limited by the ability of the tip to follow the surface. Deep crevices, or complicated deposition morphologies with large height to width aspect ratios may not be correctly imaged by the AFM.

To help answer the drawbacks of in-situ AFM imaging, the ultra-small-angle X-ray scattering (USAXS) technique was used to analyze the deposition behavior of zinc within the ionic liquid electrolyte. The USAXS technique is capable of directly analyzing a larger surface area of the substrate on the order of square millimeters than is capable by AFM. The penetrating nature of X-rays also allows for analysis of various system characteristics including porosity, phase sizes, phase shape, and the phase to matrix interface characteristics. Furthermore, the USAXS technique is capable of analysis from inter-atomic size scales to micron size scales.

An in-situ USAXS analysis was conducted on the electrodeposition of zinc within an ionic liquid electrolyte. The resulting scattering data from the in-situ USAXS scans were modeled to obtain information on how the size of the deposited zinc changes during electrodeposition. In addition, the USAXS allowed for understanding the characteristics of the zinc to electrolyte interface. The information gained from the USAXS analysis allowed for a greater understanding of the deposition behavior of zinc within an ionic liquid electrolyte.

5.1. Characterization with Ultra-Small-Angle X-Ray Scattering (USAXS)

Ultra-small-angle X-ray scattering (USAXS) is a diffraction technique that can be used to obtain atomic-scale to micron scale information based on Bragg's law. Bragg's law relates the interplanar spacing, d, to the angle of incidence, θ, and the wavelength, λ, where

$$d = \frac{\lambda}{2\sin\theta} \tag{5.1}$$

In the X-ray diffraction (XRD) regime where $2\theta > 6°$, atomic scale information can be obtained from the sharp peaks that characterize high degrees of order such as found within crystals. Information from the nano-scale and micron scale can be obtained at the small-angle scattering (SAXS) regime where $2\theta \leq 6°$. A method termed ultra-small-angle X-ray scattering (USAXS), developed by Bonse and Hart, allowed for measuring scattering at angles approaching the primary beam ($2\theta \rightarrow 0°$) [47].

In the SAXS regime, the scattering of the X-rays is caused by spatial fluctuations of the electron density within the material. The scattering intensities from a SAXS experiment on a material with nano-scale and micro-scale features typically exhibit diffuse patterns. These diffuse patterns are the result of the low degrees of order at these size scales.

Determining the real space structure from SAXS and USAXS data requires fitting the scattering data to a model. Guinier discovered that structural information such as the size and the shape of the scattering features can be obtained from the diffuse scattering in the SAXS regime [48]. Porod also determined that the pore size and the surface area can be measured for a system consisting of two phases where each of the phases exhibits different scattering length densities [49].

A schematic of the USAXS instrument based on the Bonse-Harte double-crystal configuration is shown in Figure 5.1. The photons are obtained from a source that is typically white beam radiation from a modern synchrotron. The monochromator allows for selecting photons of the desired energy for the USAXS analysis. The multiple bounces of crystal diffraction within the monochromator and the analyzer help improve the signal-to-noise ratio of the sample scattering by reducing the tails of the instrumental rocking curve [50]. The scattered X-rays are collected for each angle by the detector. The USAXS curve is generated by rotating and translating the analyzer crystal through the desired range as shown in Figure 5.1.

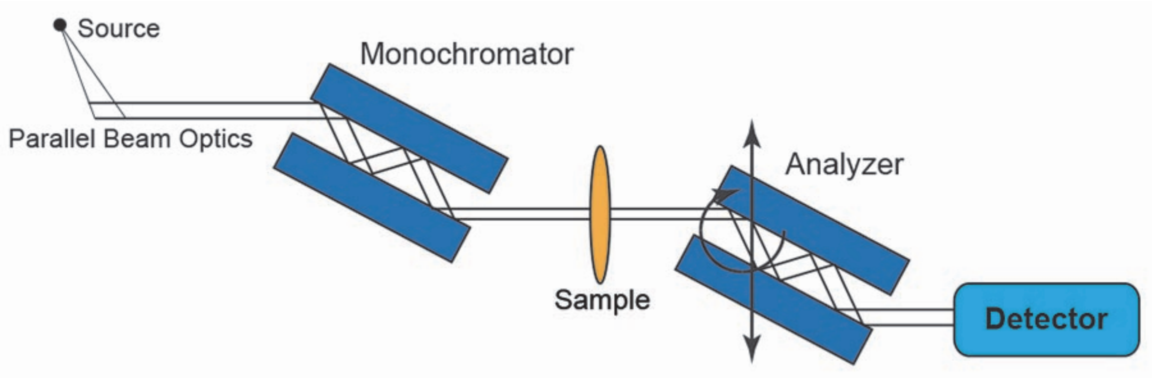

Figure 5.1. Schematic of an USAXS instrument based a Bonse-Hart double-crystal configuration.

The scattering vector, q, is defined as

$$q = (4\pi/\lambda)\sin\theta \tag{5.2}$$

where 2θ is the scattering angle and λ is the wavelength. The scattering intensity I_s in photons per second is

$$I_s = I_0 \varepsilon \Delta\Omega \frac{d\sigma}{d\Omega}(q) \tag{5.3}$$

Where I_0 is the incident of the X-ray intensity per unit area per unit time, ε is the detector efficiency, $\Delta\Omega$ is the solid angle of the detector and $d\sigma/d\Omega$ is the differential scattering cross-section per unit volume per unit solid angle.

Part of the incident X-ray beam is also absorbed within the sample. The transmitted intensity per unit area per second, I_T, is

$$I_T = I_0 e^{-\mu_l t_s} \tag{5.4}$$

where μ_l is the linear absorption coefficient and t_s is the sample thickness. The sample transmission, T_r, is the ratio of I_T to I_0. Therefore, the measured scattering intensity is

$$I_S = I_0 \varepsilon T_r \Delta\Omega A_s t_s \frac{d\Sigma}{d\Omega}(q) \tag{5.5}$$

where A_s is the cross section of the beam and $d\Sigma/d\Omega$ is the differential scattering cross section per unit volume. The term $d\Sigma/d\Omega$ contains the information about the structure of the sample over the q-range that was spanned during the experiment. In order to analyze the scattering data, one needs to first normalize the experimental data to $d\Sigma/d\Omega$ (from data reduction). The normalized I_S data is typically denoted as the differential scattering intensity $I(q)$ and the units of $I(q)$ are expressed in units of the reciprocal length [51].

Figure 5.2 shows a schematic of a one-dimensional scattering data as an example of the typical scattering data obtained from an USAXS experiment. In this figure, the scattering intensity is plotted against the scattering vector, q. Information that can be obtained from an USAXS experiment includes the size of the particles, size distribution, the shape of the particles, the surface structure (surface fractal dimension), the degree of crystallinity, and the crystal structure.

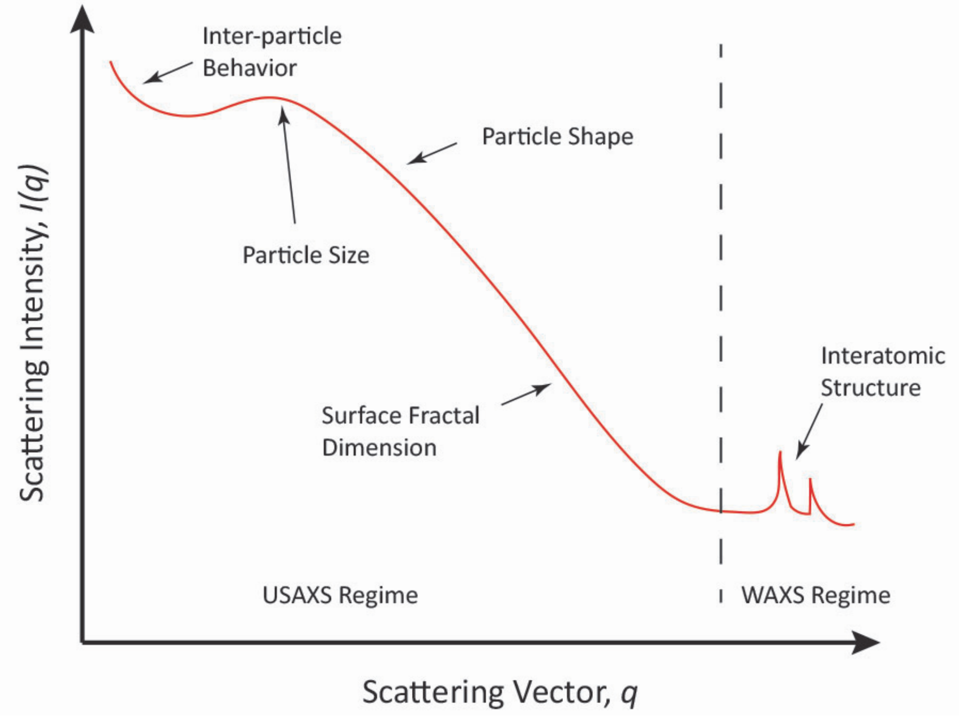

Figure 5.2. Example of a typical USAXS scattering plot that highlights how the scattering particles can be analyzed for various q-ranges.

5.1.1. Scattering Contrast

Small-angle scattering from a sample is the result of spatial fluctuations of the electron density. For a general case, the density, ρ, of a scattering entity is described by

$$\rho = \sum_i \varrho_i b_i \tag{5.6}$$

where ϱ_i is the density of the scatterers per unit volume and b_i is the scattering length of scatterers of type i. The density of scatterers can be calculated from the density and the atomic weight of a substance.

For X-ray scattering, the scattering length density is denoted as ρ_{e^-} to signify that the scattering length density is effectively the density of electrons within a substance. The scattering length of a single electron, r_{e^-}, is equal to its classical radius (Thomson radius),

$$r_{e^-} = \frac{e^2}{4\pi\varepsilon_0 mc^2} \tag{5.7}$$

where e is the electric charge of an electron (1.602×10^{-19} C), ε_0 is the permittivity of free space, m is the mass and c is the speed of light. The scattering length, r_{e^-}, has a value of 2.818×10^{-15}m. Therefore, the total effective scattering length of electrons of type i atom is

$$b_i = (r_e\text{-})f_i \tag{5.8}$$

where f_i is the scattering factor of atom of type i. By summing over the entire sample, where Z is the atomic number, the scattering length density is

$$\rho_{e^-} = (r_e\text{-}) \sum_Z \varrho_Z f_Z \tag{5.9}$$

Due to the complex nature of the scattering factor, f_Z, ρ_{e^-} is also a complex number. In order to allow for the separation of the scatterers from the matrix, the scattering contrast is used. The scattering contrast is denoted as $|\Delta\rho|^2$ and it is a real number defined as

$$|\Delta\rho|^2 = \left|\rho_{e^-,\phi_1} - \rho_{e^-,\phi_2}\right|^2 \tag{5.10}$$

where ρ_{e^-,ϕ_1} and ρ_{e^-,ϕ_2} is the scattering length density of phases ϕ_1 and ϕ_2. Combining with equation (5.9) yields

$$|\Delta\rho|^2 = \left|(r_e\text{-}) \sum_Z \Delta\varrho_Z f_Z\right|^2 \tag{5.11}$$

where

$$\Delta\varrho_Z = \varrho_{Z,\phi_1} - \varrho_{Z,\phi_2} \tag{5.12}$$

The scattering contrast, $|\Delta\rho|^2$, describes the fluctuations of the electron density that result in the small-angle scattering within a sample. The scattering contrast can also be used as a figure of merit to determine whether or not scattering will be observable between two different phases [51].

5.1.2. Structural Analysis

A. Non-Interacting Particles (Colloidal Suspension)

The size of non-interacting particles regardless of their shape can be approximated in terms of the radius of gyration, R_G, using the Guinier law

$$I(q) = NV^2\Delta\rho^2 exp\left(\frac{-q^2{R_G}^2}{3}\right) \tag{5.13}$$

where N is the number of uniform particles per unit volume and V is the volume of a particle. This approximation is only valid where $qR_G < 1$. At the asymptotic limit ($qR_G \gg 1$) where the intensity decay rate remains constant with increasing q, the scattering is dominated by the interface of the particles [51]. If the particles are homogenous with an average surface area of S, the scattering intensity follows the Porod behavior where

$$I(q) = 2\pi N\Delta\rho^2 S q^{-4} \tag{5.14}$$

In the Porod regime, $I(q)$ is proportional to q^{-P} where P designates the power law exponent. The value of P can give insight into the interface structure between the particle and the matrix. The interface structure for both compact and fractal morphologies are summarized as [51]

- $P = 4$ → Sharp interface
- $3 \leq P \leq 4$ → Surface fractal
- $P < 3$ → Mass fractal
- $P \approx 2$ → Gaussian polymer chain

(5.15)

A sharp interface indicates that the system exhibits a locally smooth interface between the different phases. A power law exponent between 3 and 4 indicates that the surface is not locally smooth within the q-range but exhibits structure of a fractal nature. Finally, a power law exponent of lower than 3 is found in disordered polymer systems. For these disordered polymer systems, a power law approaching 3 indicates that the system exhibits mass-fractal morphologies within the disordered polymer matrix. An example of a mass fractal system is a polymeric system with a distribution of polymer coils [52].

B. Unified Scattering Model

For a system that consists of many structural levels (or hierarchical levels), the system will display a structurally limited power law region that consists of intervening Guinier regions [51]. For systems consisting of hierarchical structure, the unified scattering function can be used to describe the local scattering laws and their crossover for each of the structural levels [52, 53]. The unified scattering function is

$$I(q) = G \exp\left(-\frac{q^2 R_G^2}{3}\right) + B \left\{\frac{\left[erf\left(\frac{qR_G}{\sqrt{6}}\right)\right]^3}{q}\right\}^P \tag{5.16}$$

where $G = N\Delta\rho^2 V^2$, $B = 2\pi N\Delta\rho^2 S$, and erf is the error function. The first term of equation (5.16) is the form factor for local scattering found within the Guinier region and the second term is the local power law. Note that the unified scattering function relies on just four parameters, G, B, R_G, and P that are used to fit the model to the local scattering data. Fitting the model to n structural layers is simply done by adding the corresponding number of terms for each structural level and making the cut-off for the power law in the high q-region of the local scattering by the form factor of the preceding structural level [53].

After fitting the unified scattering function to $I(q)$, one can estimate the size of the scattering features for each hierarchical Guinier region described by the first term of equation (5.16) [51, 53]. In addition, the power law term, P, can give insight into local structure. For a sharp interface that is locally flat (termed a Porod surface), the decay rate of the local intensity should follow $I(q) \propto q^{-4}$. If $I(q)$ shows a lower decay rate, then the surface is no longer a Porod surface but it is exhibiting local structure [51-53]. This structure can be interpreted by the decay rate where $I(q) \propto q^{-P}$ as summarized in the previous section (refer to equation (5.15)).

C. Porod Invariant

For non-particulate systems such as porous materials and semi-crystalline polymers, the scattering intensity $I(q)$ can be expressed in terms of the correlation function of the scattering length density fluctuations, $\gamma(r)$,

$$I(q) = 4\pi \int_0^\infty \gamma(r) \frac{\sin(qr)}{qr} r^2 dr \tag{5.17}$$

where r is the distance between two points that are being correlated. The scattering length density fluctuations described by $\gamma(r)$ varies from the scattering contrast, $|\Delta\rho|$, to 0 as r increases from 0 to ∞ [51].

The Porod invariant, Q_P, is a parameter that comes out of the inverse transform of equation (5.17). For a two phase system, the Porod invariant, Q_P, is the integration of the total scattered intensity over all of q, and its expression is

$$Q_P = \int_0^\infty I(q) q^2 dq = 2\pi^2 |\Delta\rho|^2 V_f \tag{5.18}$$

where V_f is the volume fraction of the scatterers [51].

The Porod invariant is proportional to the mean square of the scattering contrast (fluctuation of electron density) and it is independent of the shape or size of the particles. Note that the volume fraction, V_f, is

$$V_f = \phi_1(1 - \phi_1) \tag{5.19}$$

where ϕ_1 is the volume fraction of one phase and therefore V_f is limited within the range of $0 < V_f < 0.25$.

The Porod invariant is useful for analysis of two phase systems since it allows one to follow the phase transformations and it allows for normalizing the data when the unit of $I(q)$ is uncertain [51].

5.2. USAXS Experimental

This section overviews the experimental procedure for the USAXS analysis of zinc deposition within an ionic liquid electrolyte. Details on the design of the in-situ electrochemical cell, the USAXS analysis parameters, and the electrochemical deposition procedure are overviewed. In addition, this section discusses how the scattering data were reduced and how the scattering intensity was normalized.

5.2.1. Ionic Liquid Electrolyte Preparation

The electrolyte was prepared following a similar procedure as outlined in Chapter 3 section 3.2.1. The electrolyte was prepared by dissolving a measured amount of zinc trifluoromethanesulfonate ($Zn(OTf)_2$, Sigma-Aldrich, 98%) into 1-butyl-3-methyl-imidazolium trifluoromethanesulfonate (BMIm OTf, Ionic Liquid Technologies, Inc., >99%) at an elevated temperature of 80ºC. The resulting electrolyte mixture was clear with a slight amber color. The ionic liquid electrolyte preparation followed the guidelines of Gnahm and Kolb [23] to remove residual water from the system. This procedure included adding 3 Ångstrom molecular sieves to the electrolyte at roughly a 1 to 5 mass ratio. In addition, the electrolyte was dried within a vacuum oven at 100°C under a vacuum of 25 mm Hg for at least 24 hours prior to testing.

The targeted $Zn(OTf)_2$ concentration was 0.34 molal (mol kg^{-1}). The measured molality for the electrolyte by mass balance was 0.3362 +/- 0.001 mol kg^{-1}. Note that $Zn(OTf)_2$ concentrations are given as molal quantities (mol kg^{-1}) throughout this chapter.

5.2.2. In-situ USAXS Electrochemical Cell

The electrochemical experiments within the USAXS instrument were conducted within a polyether ether ketone (PEEK) enclosed cell utilizing a design by El-Bassem et al. [54]. Figure 5.3 shows photographs of the in-situ electrochemical cell. The substrate was positioned normal to the incident beam within the beam window section of the cell. An electrolyte reservoir was connected to the beam window area by four 2 mm diameter channels. These channels were also used to thread the counter and reference electrodes to the beam window section. The total volume of the reservoir and the beam window section was approximately 8 milliliters.

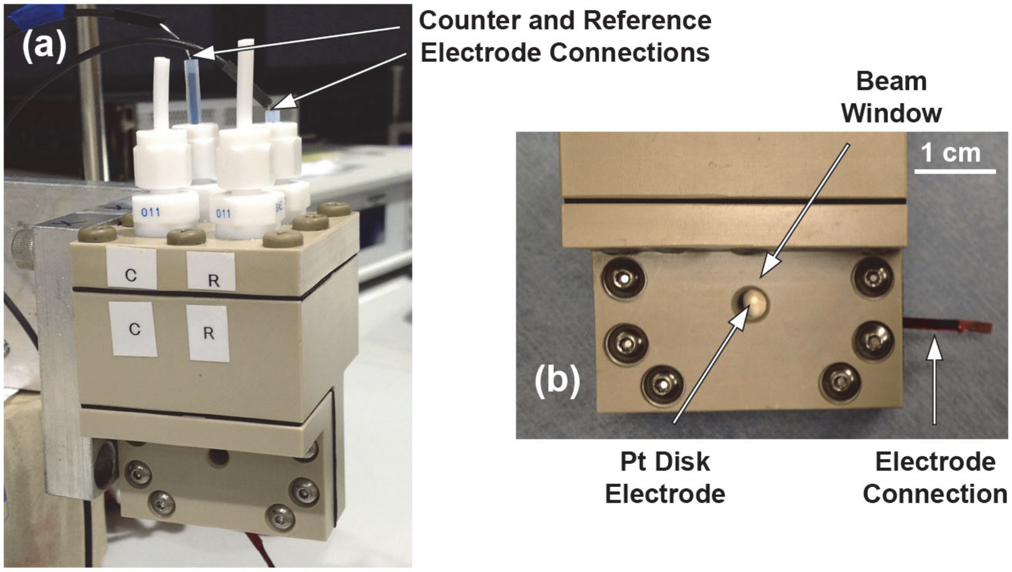

Figure 5.3. Photographs showing the in-situ electrochemical cell used for USAXS analysis. Photograph (a) shows a cell mounted on the bracket for positioning within the USAXS chamber. Photograph (b) shows a close up of the beam window and the location of the Pt disk electrode.

The substrate consisted of a 2 mm diameter platinum disk that was sputter deposited on a 0.5 mm thick glass wafer. The thickness of the platinum disk was about 600 nm and the surface roughness was measured to be 2 to 3 nm RMS (from AFM measurements). For electrodeposition, there was approximately a 1 mm layer of electrolyte above the platinum substrate. A schematic of the beam window section is shown in Figure 5.4. The electrical connection to the platinum substrate was obtained by a 0.1 mm wide 6 mm long and 600 nm thick Pt leg that was also sputter deposited. The Pt leg was connected to a 0.20 mm thick copper foil with silver epoxy. The platinum leg, copper foil, and epoxy connection were coated with enamel for insulation from the electrolyte. The copper foil extended out of the cell for electrical connection. Finally, the cell was sealed with Viton gaskets.

The counter and reference electrodes were a Zn wire (Alfa Aesar, 99.995%). The potentials were referenced to the Zn/Zn(II) of the reference electrode. The working electrode, 2 mm diameter Pt disk, had an area of 0.0314 cm^2. Prior to attaching the copper foil to the leg of the Pt electrode, the Pt electrode was cleaned by submerging within 1M H_2SO_4 for 5 minutes and washed with Millipore water. The cleaning process was repeated once to assure that most contaminants were removed from the Pt surface.

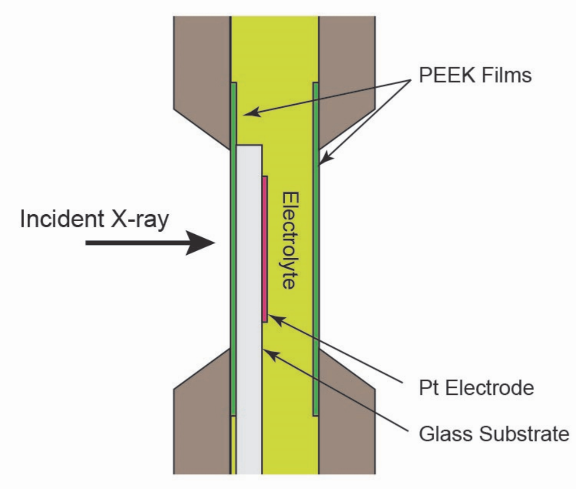

Figure 5.4. Schematic of the in-situ electrochemical cell's cross-section at the beam window area used for USAXS analysis. The counter and reference electrodes are located outside of the plane of view for this figure.

The USAXS experiments were conducted within shop air that could allow the ionic liquid electrolyte to absorb moisture. It was attempted, however, to limit the exposure of the ionic liquid to the shop air by enclosing the electrochemical cell and minimizing the time from removing ionic liquid out of the vacuum oven to the start of USAXS testing (roughly 10 minutes).

5.2.2. USAXS Instrumentation and Procedure

A. USAXS Instrument

The experiments were conducted on the USAXS instrument in sector 15 (ChemMat CARS) at the Advanced Photon Source (APS) located at Argonne National Laboratory, Illinois, USA. This USAXS instrument was combined with a two-dimensional wide-angle X-ray scattering (WAXS) detector and a two-dimensional small-angle X-ray scattering SAXS detector (pinSAXS) allowing for analysis from the micron size range down to the crystal structure of the sample. The USAXS instrument is capable of measuring within a q-range from 10^{-4} Å^{-1} to 1 Å^{-1}. With the SAXS and WAXS instruments the q-range can be extended to 5.24 Å^{-1}. Detailed information on the design and the capabilities of the USAXS instrument can be found in relevant papers [50, 55, 56].

The beam energy used for the USAXS analysis was 17.0 keV ($\lambda = 0.72932$ Å). The area of the Pt substrate illuminated by the X-ray beam was 0.8 × 1.5 mm (0.012 cm^2) or roughly 40% of the entire surface area of the Pt substrate. For the in-situ electrodeposition experiment, the USAXS was conducted in the one-dimensional collimated mode.

B. X-Ray Damage

Although analysis of the X-ray scattering allows for analysis of the electrodeposited Zn structure, the sample and electrolyte can be damaged from the high energy of the penetrating X-rays. The organic nature of ionic liquids may make them easily susceptible to X-ray beam damage, therefore, it is critical to minimize the absorbed photon energy. How radiation damages occurs is not fully understood but it is generally accepted that radiation damage manifests in formation of radicals [51]. These radicals may form new structures or compounds within the sample.

To lower the X-ray dose experienced by the sample, both Al and Ti filters were inserted in the incident beam that effectively decreased the number of photons per unit of time of the incident beam by 96.26%. In addition, during zinc deposition, additional filters were inserted into the beam to effectively decrease the number of photons striking the sample from the incident beam by nearly 100%. The total time the system was exposed to X-rays for the in-situ USAXS analysis was about 45 minutes.

The total photon energy per unit volume per second that was experienced by the ionic liquid electrolyte was estimated using the Anomalous Scattering Calculator within Irena [57] for a beam energy of 17 keV. The incident beam first hits the PEEK window followed by the glass substrate and the Pt electrode prior to the ionic liquid electrolyte (refer to Figure 5.4). The estimate for the percentage of photon energy transmitted and absorbed by each material within the experimental setup are listed in Table 5.1.

Table 5.1. List of calculated X-ray transmissions and subsequent absorption characteristics of each component of the experimental setup. The total absorption multiplies the absorption for each component moving downstream following the incident X-ray beam.

Material / Component	X-ray Transmission (%)	X-ray Absorption (%)	Total Absorption (%)
Al and Ti filters	3.74	96.26	96.26
PEEK window	98.83	1.17	96.30
Glass substrate	62.63	37.37	97.69
Pt electrode	88.80	11.20	97.94
Ionic liquid electrolyte	79.56	20.44	98.36

The total X-ray absorption up to the ionic liquid electrolyte layer was estimated to be 98.36% or roughly 1.64% of the incident beam encounters the ionic liquid electrolyte. Of the 1.64% transmitted to the ionic liquid, roughly 20.44% is absorbed by the ionic liquid. Therefore, a total of 0.34% of the incident beam is absorbed by the ionic liquid.

WAXS and SAXS images were obtained without Al or Ti filters to allow for adequate exposure. Since obtaining these images would significantly increase the dosage experienced by the ionic liquid electrolyte, the WAXS and SAXS images were obtained only after the final electrodeposition of zinc and on the “blank” Pt substrate.

C. Ex-Situ Electron Microscopy

For electron microscopy, Zn was deposited on a Pt substrate within the USAXS cell under the same electrochemical conditions as was conducted for the in-situ USAXS analysis (refer to Section 5.2.3). Electron microscopy was conducted on the final Zn deposition morphology after 3600 Zn monolayers of charge passed. The electron microscopy was conducted on a JEOL JSM-7401F FESEM scanning electron microscope. Images were obtained using the lower secondary electron detector (LEI mode) that allowed for better imaging of the Zn deposition topography.

5.2.3. Electrochemical Procedure

The USAXS measurements were conducted in-situ for the zinc deposition on a Pt substrate undergoing pulses of constant potential of -700 mV versus the Zn/Zn(II) reference. Deposition pulses at constant potential were conducted for a total charge passed of 209.2 mC cm^{-2}. This value corresponds to an ideal zinc thickness of near 100 nm and 400 monolayers of zinc assuming a 100% zinc deposition efficiency. USAXS scanning was conducted between pulses. During USAXS scanning, the substrate was held at a slightly reducing potential of a deposition overpotential of -5 mV. The total time required for a single USAXS scan (initial beam calibration and 200 measurements at different vectors) was about 9 minutes.

Although the radiation dosage was lowered by utilizing Al and Ti filters, it was feared that the radicals that are produced by the X-rays within the ionic liquid electrolyte could impede the initial Zn deposition on the Pt substrate. Therefore, two USAXS scans were conducted on two different Pt substrates within the ionic liquid electrolyte to obtain a “blank” scan. These blank USAXS scans were used in the data reduction of the USAXS scans obtained during zinc deposition. Scans on two different substrates were conducted to check for consistency. A fresh Pt substrate was then used for the actual zinc deposition analysis. Therefore, the first zinc deposition pulse was conducted before illuminating the sample and the ionic liquid electrolyte by the X-ray beam.

The resting potential for the system after zinc was deposited on the Pt substrate was estimated to be approximately -220 ± 10 mV versus the Zn/Zn(II) reference. Therefore, the total deposition overpotential for this zinc deposition experiment was approximately -480 mV. A total of five USAXS scans were conducted after various amounts of charge passed listed in Table 5.2.

Table 5.2. List of total charge passed for each USAXS scan conducted in-situ during the electrodeposition of Zn. The ideal thickness of the deposited Zn assumed 100% deposition efficiency.

USAXS Scan	Total Charge Passed (mC cm^{-2})	Ideal Thickness (nm)	Ideal Thickness (Zn monolayers)
1	209.2	99.2	400
2	627.6	297.6	1200
3	1046.0	496.0	2000
4	1464.4	674.4	2800
5	1882.8	892.8	3600

5.2.4. Data Reduction

Each USAXS scan records data that include the stage angle, the photodiode counts for each range, the measurement time in seconds for each point, and the X-ray beam monitor counts for each point. For the q-range analyzed, a total of 200 measurements were obtained. The data reduction was conducted within the Indra2 package [50] within Igor Pro (version 6.22A). First, a rocking curve was created from the blank sample. The blank sample for this analysis was a Pt substrate within the ionic liquid electrolyte. From the blank sample, the stage angle and the photodiode counts with the range information were used to generate q values for the intensity in the counts. Next, a rocking curve was generated from these values to find the beam center. At the beam center, q was set to zero.

The next step in the data reduction was subtracting the blank sample from the USAXS data obtained during the zinc deposition experiments. Since the blank included the platinum substrate, any changes in the intensity profile within the q-range should be the result of the growth of zinc on the platinum substrate. Because filters were used for scanning, the data exhibited a high level of noise at the high q-range. To ensure that all the data in the high q-range was obtained after data reduction, the intensity within the high q-range was slightly increased. This increase in the intensity at the high q-range did not affect the data analysis.

5.2.5. Normalizing the Scattering Intensity

To correctly normalize the scattering intensity, $I(q)$, the thickness of the Zn deposition is required [50]. Since the zinc deposition was analyzed in-situ, however, the deposition thickness could not be measured directly. The zinc deposition thickness for each USAXS scan was estimated using the thickness measurements obtained from the AFM analysis under similar electrochemical conditions (refer to Chapter 4). From the AFM analysis, it was estimated that the actual thickness of the Zn deposition layer was around 90% of the ideal thickness.

The data reduction presented in this chapter was conducted with deposition thickness values at 90% of the ideal deposition value. Since the deposition thickness was unknown, however, the USAXS data were also reduced using a low thickness value of 50% ideal and a high thickness value of 130% ideal. A standard error was then calculated from the measured values obtained for each of the models for the three different thicknesses. The total standard error was then obtained by adding the standard error obtained from the various thicknesses to the standard error of the model fit. The three thicknesses used to normalize the scattering intensity for each of the USAXS scans is listed in Table 5.3.

Table 5.3. Ideal thickness for each USAXS scan and the thicknesses used for normalizing the scattering intensity (50%, 90% and 130% of the ideal thickness).

USAXS Scan	Ideal Thickness (monolayers)	Ideal Thickness (nm)	50% of Ideal (nm)	90% of Ideal (nm)	130% of Ideal (nm)
1	400	99.2	50	90	130
2	1200	297.6	150	270	390
3	2000	496.0	250	450	640
4	2800	674.4	340	610	880
5	3600	892.8	450	800	1160

5.2.6. Uncertainty in USAXS Analysis

Since the true thickness of the zinc deposition is not known, it places uncertainty on the data analysis for the parameters that are intensity dependent. These parameters include the scattering particle volume, V, and the scattering particle surface area, S, and the number of scatterers, N (refer to equation (5.16)). The Porod invariant is also intensity dependent since it is the sum of the intensity measured over all of q (refer to equation (5.18). Parameters that are q dependent, however, such as the radius of gyration, R_G, will not be affected by this uncertainty. In addition, the power law exponent, P, is calculated from the slope of the intensity decay versus q but even if there was a large error in the estimated thickness, the calculated value of the power law exponent would not significantly change.

5.3. USAXS Results and Discussion

This sections overviews the results obtained from the WAXS imaging and the USAXS scattering data. This section discusses how the unified fit model was used to characterize the Zn deposition. Finally, the structure of the Zn deposition is discussed with the information obtained from the unified model of the scattering data.

5.3.1. Wide-Angle X-ray Scattering (WAXS)

The WAXS was used to ensure that zinc was being deposited after the electrodeposition experiments and that no other compounds were being formed. WAXS was conducted on the blank samples (Pt substrate without Zn deposition) and on the final USAXS scan (USAXS scan 5). Figure 5.5 shows the WAXS image obtained on a Pt substrate and on a Pt substrate after Zn deposition. The WAXS image exhibited diffraction rings pointing to a polycrystalline Zn deposition where the Zn crystals were randomly oriented.

The graph in Figure 5.6 plots the intensity measured by the WAXS versus q for the platinum without zinc deposition and for the substrate after zinc deposition. The platinum substrate without zinc deposition exhibited three main peaks of intensity corresponding to the (111), (200), and (220) hkl planes. After deposition, six new peaks emerge that correspond to various incidence planes of the zinc crystal structure. Table 5.4 lists the designations for each intensity peak observed after Zn deposition along with the calculated d-spacing, the published d-spacing and the percentage difference. The calculated d-spacing for the incidence planes of zinc exhibited good agreement with the published values (within 2%). Furthermore, zinc oxide was not observed from the WAXS analysis. The highest intensity peaks for zinc oxide would be expected at a d-spacing of 2.476, 2.602, and 2.816 Å. These value corresponds to a q of 2.538, 2.415, and 2.231 $Å^{-1}$ and these peaks were not observed in the q-range (within the q-range below the peak observed for the Zn(002)).

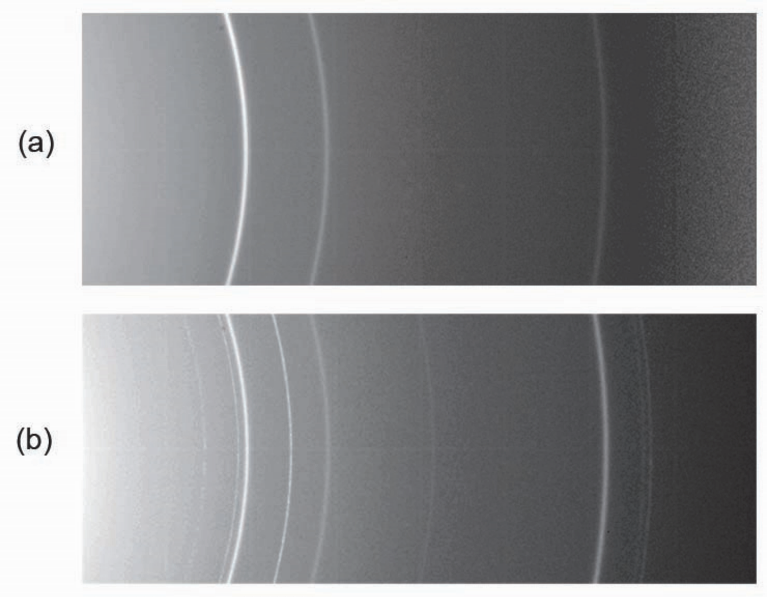

Figure 5.5. WAXS images obtained on a Pt substrate without Zn deposition (a) and on a Pt substrate after Zn deposition (b).

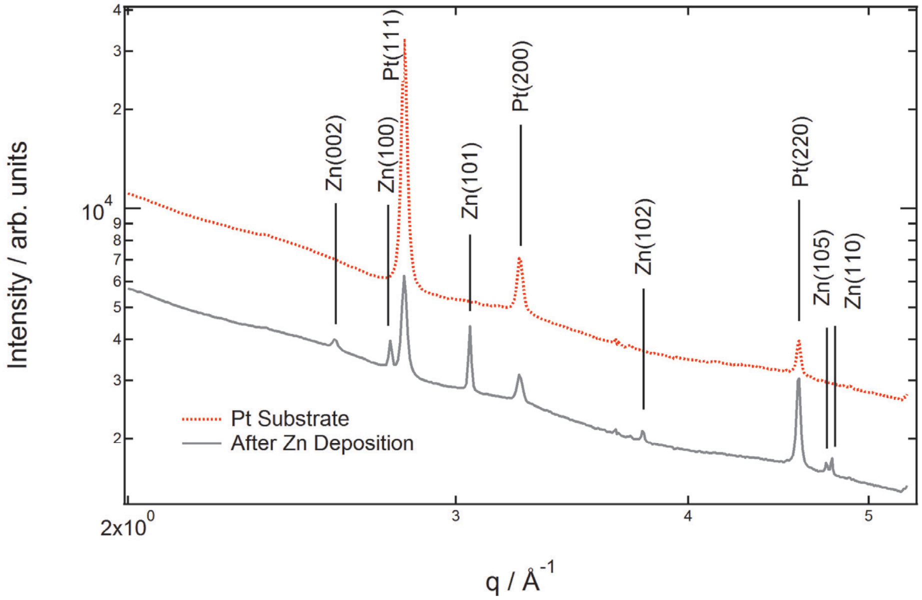

Figure 5.6. Scattering intensity of a Pt substrate without Zn deposition and a Pt substrate after Zn deposition. Designation of scattering peaks are noted within the graph. The curves have been offset for clarity along the intensity axis.

Table 5.4. Designation of the intensity peaks observed by WAXS along with the calculated d-spacing, published values for the d-spacing [58], and the percentage difference.

Designation (*hkl*)	***q*** **($Å^{-1}$)**	**Calculated d-spacing (Å)**	**Published d-spacing (Å)**	**Difference (%)**
Zn (002)	2.5812	2.434	2.437	0.12
Zn (100)	2.7661	2.271	2.308	1.58
Pt (111)	2.814	2.233	2.265	1.42
Zn (101)	3.0536	2.058	2.091	1.60
Pt (200)	3.2542	1.931	1.962	1.57
Zn (102)	3.7792	1.663	1.687	1.44
Pt (220)	4.587	1.368	1.388	1.26
Zn (105)	4.7444	1.324	1.342	1.32
Zn (110)	4.7786	1.315	1.332	1.29

5.3.2. Scattering Intensity

During zinc deposition at a constant potential of -700 mV versus the Zn/Zn(II) reference, five USAXS scans were obtained at 400, 1200, 2000, 2800, and 3600 ideal Zn monolayers. The ideal Zn monolayers corresponds to the amount of charge required for deposition of an electrodeposition of Zn film assuming 100% efficiency (refer to Table 5.2). The calculated intensity after data reduction for the five USAXS scans is shown in Figure 5.7. In the high q region ($q > 0.06$), there was a high level of background noise for the scans and this background noise did not allow for resolving structural data. The high background noise was the result of the Al and Ti filters used to minimize the beam damage to the ionic liquid. In the mid q-range ($0.003 < q < 0.06$), the intensity for each of the data sets decays at roughly the same slope. This region is roughly within the Porod region and it suggests that the interface structure between the two phases (Zn and the ionic liquid electrolyte) doesn't change throughout the deposition analysis. Within the low q-range ($q < 0.003$), Guinier regions were observed where the intensity exhibits a knee as the scattering intensity behavior transfers from the Porod power law scaling regime. The location of this knee appeared to occur at lower q values with increasing deposition thickness. This suggests that the average size of the Guinier scatting entities is increasing with increasing deposition thickness.

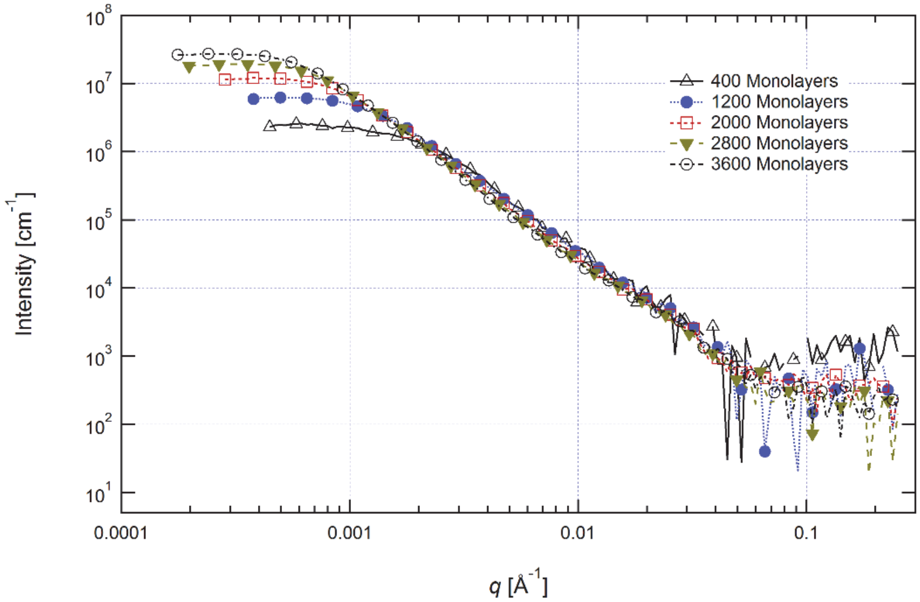

Figure 5.7. Log-log plot of the normalized intensity versus the scattering vector, q, obtained from in-situ USAXS scans for various ideal Zn electrodeposition thicknesses (Zn monolayers).

5.3.3. Unified Fit Analysis

A unified fit model was developed for each of the USAXS scans utilizing the Irena2 package within Igor Pro [57]. This model uses the unified fit approach developed by Beaucage [52, 53]. For the unified fit model, the parameters G, R_G, B and P were fitted to the scattering data by the least squares method.

Figure 5.8 and Figure 5.9 show the resulting one level unified fit model for the scattering data obtained after the amount of charge passed corresponding to 400 and 1200 Zn monolayers. From the standardized residual analysis, the one level model appeared to adequately describe the scattering data obtained from these Zn depositions.

Figure 5.10 shows the resulting one level unified fit model for the scattering data obtained after the amount of charge passed corresponding to 2000 Zn monolayers. With one level, the standardized residuals exhibited periodicity that may be the result of underlying structure. A two level analysis was conducted and the resulting model is shown in Figure 5.11. The two level model resulted in a better description of the scattering data as shown in the standardized residuals. The values for B and P of the substructure, designated B_{sub} and P_{sub}, were not fitted since the background noise did not allow for these parameters to be resolved. Instead, the model fit was conducted with these parameters held constant with values that were obtained from measuring the slope in the high q region (B_{sub} = 0.005 and P_{sub} = 3.6).

As with the one level unified fit for the 2000 monolayer deposition, the one level unified fit for the 2800 monolayer deposition also exhibited a high standardized residual as shown in Figure 5.12. A two level unified model was fitted to the intensity data and the results with the standardized residuals are shown in Figure 5.13. For fitting the two level model, the parameters B_{sub} and P_{sub} were held constant (B_{sub} = 0.016 and P_{sub} = 3.4).

Figure 5.14 shows the one level unified fit for the zinc deposition after 3600 monolayers. As found with the previous data for the 2000 and 2800, the one level unified fit exhibited a poor fit to the scattering data. The residual fit was improved by using two levels as shown in Figure 5.15. As with the fitting for the 2000 and 2800 data, the parameters B_{sub} and P_{sub} were held constant (B_{sub} = 0.016, and P_{sub} = 3.4).

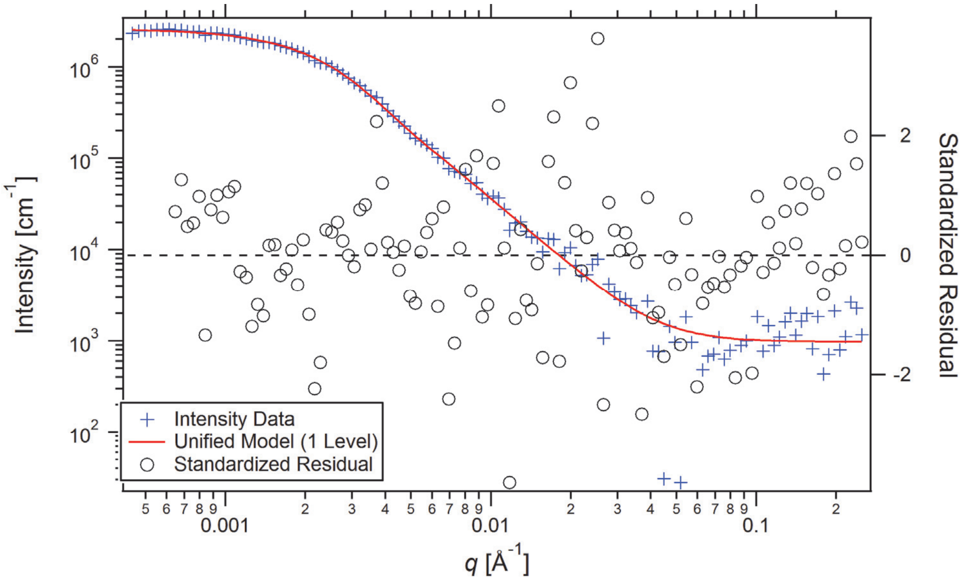

Figure 5.8. Log-log plot of a one level unified fit model (solid line) obtained for the 400 Zn monolayer scattering data. The standardized residuals of the unified fit model to the intensity data are plotted against the right axis. Fitted parameters are $G = 3.21 \times 10^7$, R_G = 734.9 Å, $B = 1.68 \times 10^{-2}$, and P = 3.41.

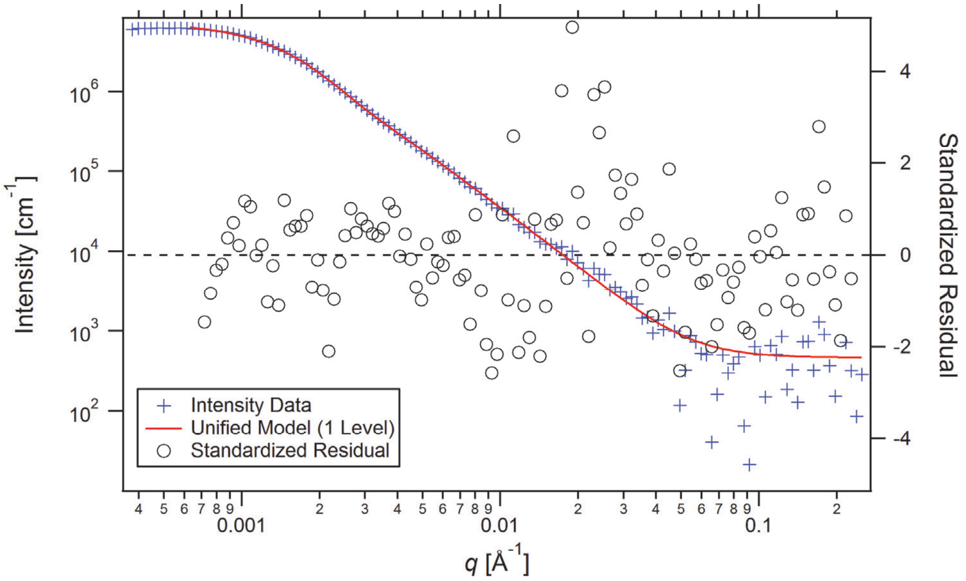

Figure 5.9. Log-log plot of a one level unified fit model (solid line) obtained for the 1200 Zn monolayer scattering data. The standardized residuals of the unified fit model to the intensity data are plotted against the right axis. Fitted parameters are $G = 1.52 \times 10^8$, $R_G = 1197$ Å, $B = 2.11 \times 10^{-2}$, and $P = 3.36$.

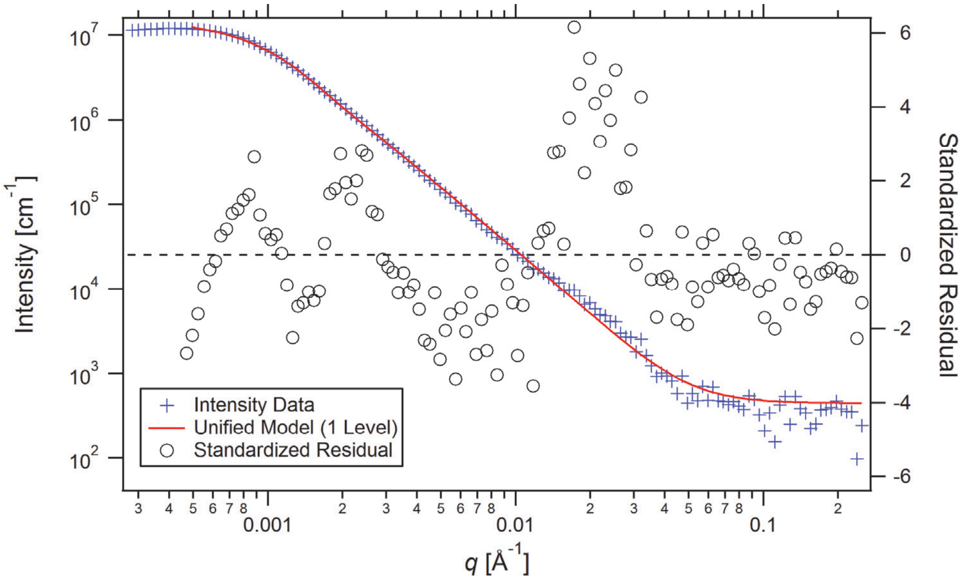

Figure 5.10. Log-log plot of a one level unified fit model (solid line) obtained for the 2000 Zn monolayer scattering data. The standardized residuals of the unified fit model to the intensity data are plotted against the right axis.

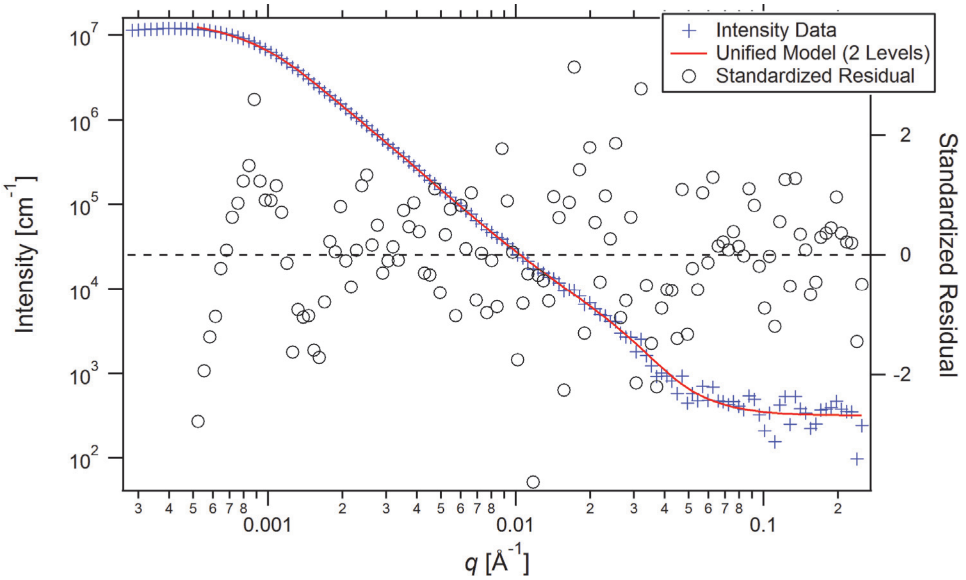

Figure 5.11. Log-log plot of a two level unified fit model (solid line) obtained for the 2000 Zn monolayer scattering data. The standardized residuals of the unified fit model to the intensity data are plotted against the right axis. Fitted parameters are $G = 4.86 \times 10^8$, $R_G = 1825$ Å, $B = 5.25 \times 10^{-3}$, and $P = 3.58$; fitted parameters for the sub-structure are $G_{\text{sub}} = 7.75 \times 10^3$, $R_{G,\text{sub}} = 76.8$ Å.

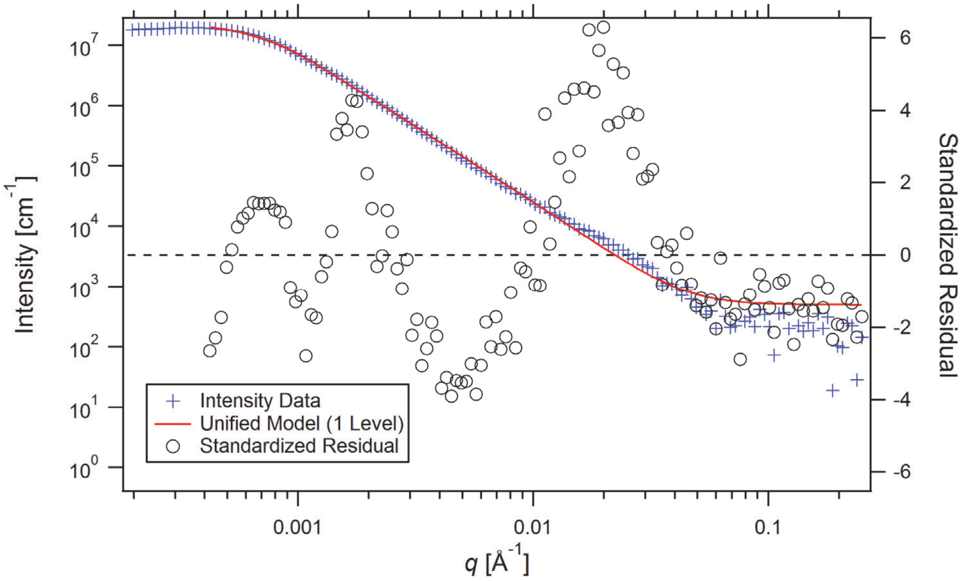

Figure 5.12. Log-log plot of a one level unified fit model (solid line) obtained for the 2800 Zn monolayer scattering data. The standardized residuals of the unified fit model to the intensity data are plotted against the right axis.

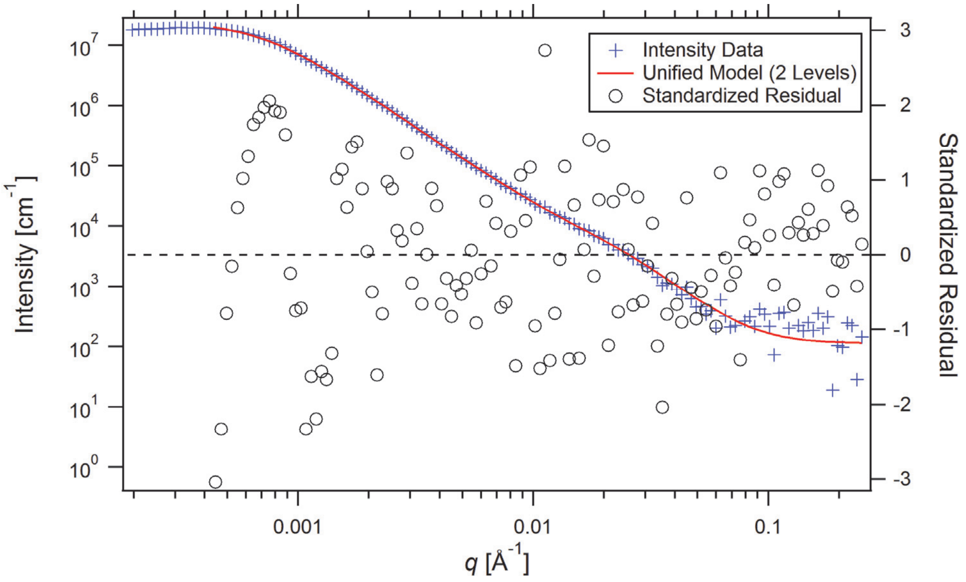

Figure 5.13. Log-log plot of a two level unified fit model (solid line) obtained for the 2800 Zn monolayer scattering data. The standardized residuals of the unified fit model to the intensity data are plotted against the right axis. Fitted parameters are $G = 1.02 \times 10^9$, $R_G = 2325$ Å, $B = 3.36 \times 10^{-3}$, and $P = 3.65$; fitted parameters for the sub-structure are $G_{\text{sub}} = 8.88 \times 10^3$, $R_{G,\text{sub}} = 78.8$ Å.

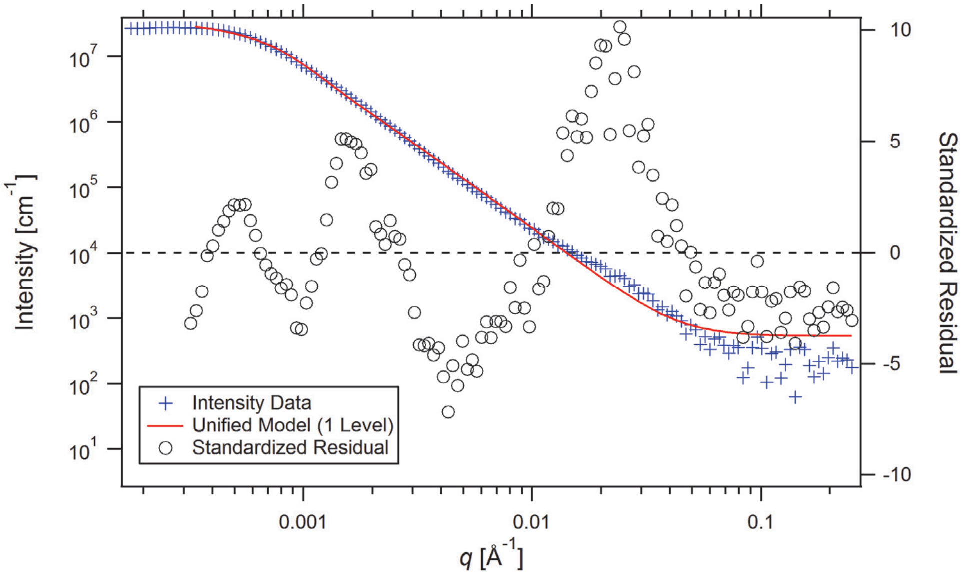

Figure 5.14. Log-log plot of a one level unified fit model (solid line) obtained for the 3600 Zn monolayer scattering data. The standardized residuals of the unified fit model to the intensity data are plotted against the right axis.

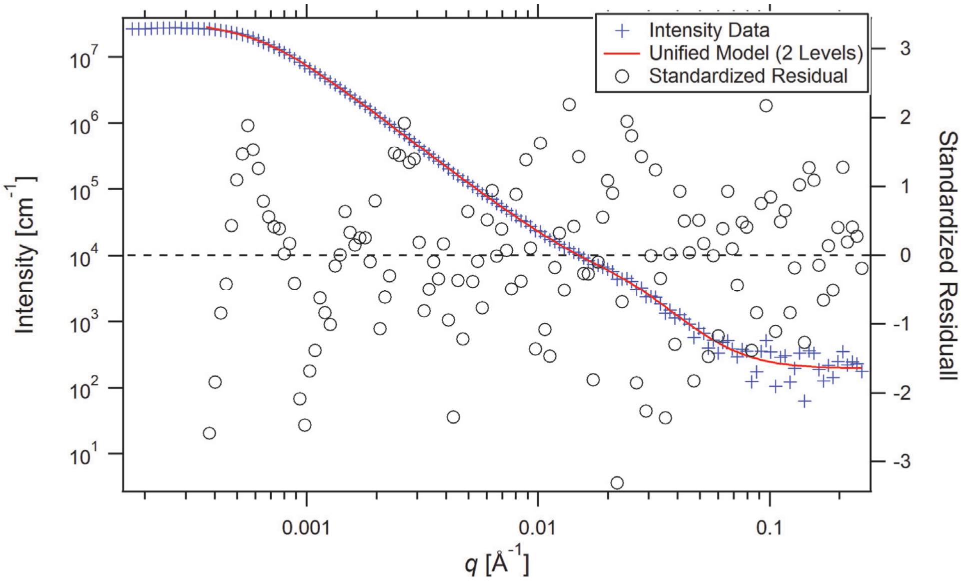

Figure 5.15. Log-log plot of a two level unified fit model (solid line) obtained for the 3600 monolayer scattering data. The standardized residuals of the unified fit model to the intensity data are plotted against the right axis. Fitted parameters are G = 1.61 × 10^9, R_G = 2649 Å, B = 2.55 × 10^{-3}, and P = 3.68; fitted parameters for the sub-structure are G_{sub} = 8.49 × 10^3, $R_{G,\text{sub}}$ = 70.1 Å.

5.3.4. Structure Analysis

The results obtained for G, R_G, B, P, G_{sub} and $R_{G,\mathrm{sub}}$ from the unified fit of the USAXS scans are listed in Table 5.5. The data were obtained with the scattering data reduced using a deposition thickness at 90% of the ideal thickness. G is the exponential prefactor ($G = N\Delta\rho^2V^2$), R_G is the radius of gyration for the scattering particle, B is the constant prefactor to the power-law scattering ($B = 2\pi N\Delta\rho^2S$), and P is the power law exponent for the Porod regime.

Table 5.5. Fitted parameters from the unified model of the scattering data obtained from the in-situ USAXS scans for various ideal Zn electrodeposition thicknesses (Zn monolayers).

USAXS Scan (Zn Monolayers)	G	R_G (Å)	B	P	G_{sub}	$R_{G,\mathrm{sub}}$ (Å)
400	3.21×10^{7}	734.9	1.68×10^{-2}	3.41	—	—
1200	1.52×10^{8}	1197	2.11×10^{-2}	3.36	—	—
2000	4.86×10^{8}	1825	5.25×10^{-3}	3.58	7.75×10^{3}	76.8
2800	1.02×10^{9}	2325	3.36×10^{-3}	3.65	8.88×10^{3}	78.8
3600	1.61×10^{9}	2649	2.55×10^{-3}	3.68	8.49×10^{3}	70.1

The Porod factor, P, obtained from the unified fit model remained nearly constant with values between 3.4 to 3.7. With the Porod factor between 3 and 4, the model suggests that the Zn and ionic liquid electrolyte interface exhibits a surface fractal structure [51, 53]. The interface does not exhibit a locally sharp interface (refer to equation (5.15)). Furthermore, the nature of the interface does not appear to change during the electrodeposition of Zn from 400 to 3600 Zn monolayers of charge passed.

The prefactors G and B can be used to obtain the number of scatters, the volume of the scatterers, and the surface area of the scatters if the system exhibited Porod behavior ($P = 4$). Since the Zn deposition did not exhibit Porod behavior ($P \approx 3.5$), one cannot conduct a valid analysis of the prefactors G and B. Furthermore, these parameters are intensity dependent and the intensity was not normalized against the true thickness since the true thickness was unknown. General observations, however, were made from the parameters assuming that the intensity was normalized correctly. First, G increases with increasing deposition thickness. This parameter is most influenced by the volume of the scatterers, V, suggesting that the volume of the scatterers within this Guinier range was increasing with increasing deposition thickness. The parameter B decreased with increasing thickness. This parameter is proportional to the surface area of the scatterers, S, and the number of the scatterers, N. This could suggest that the surface area of the scatterers decreases with increasing thickness. It could also suggest that the number of scatterers decreases with increasing thickness or a combination of both.

The radius of gyration parameters, R_G and $R_{G,\mathrm{sub}}$, obtained from the unified fit model were used to obtain a real space correlation length of the two-phase system. Figure 5.16 plots the radius of gyration, R_G, from the main Guinier region against the amount of charge passed in terms of Zn monolayers. The radius of gyration increased from 73.5 nm to 265 nm from the amount of charge passed of 400 Zn monolayers to 3600 Zn monolayers. The increase in the radius of gyration suggests that the average size of the scattering entities were continually increasing during the Zn deposition. Furthermore, the radius of gyration appeared to exhibit a linear dependence on the amount of charge passed.

The total standard error from the model fit and deposition thickness uncertainty is also shown in Figure 5.16. The standard error range was small and confirms that the radius of gyration is largely independent to the thickness used for the scattering data reduction. Therefore, despite the uncertainty of the actual deposition thickness from this in-situ analysis, the values obtained for the radius of gyration appeared valid.

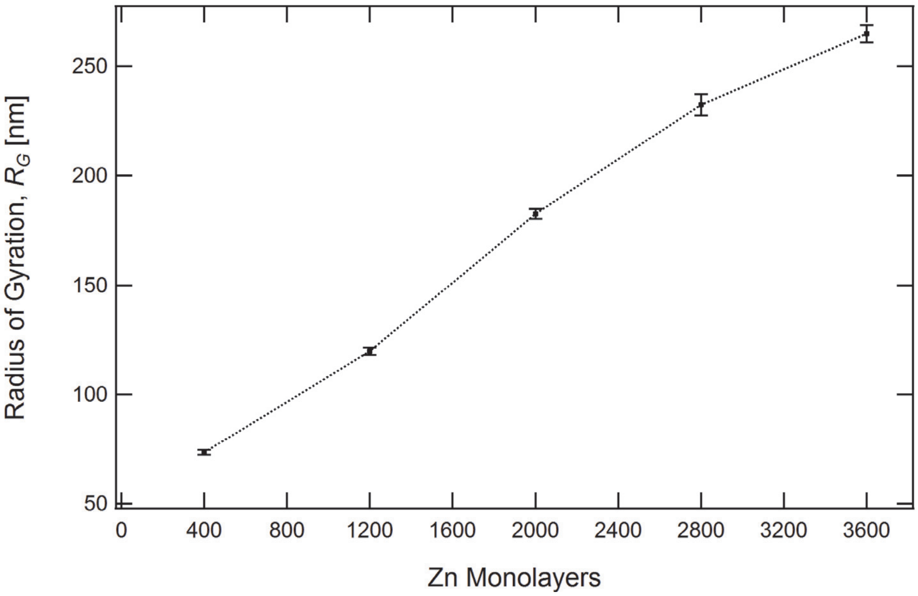

Figure 5.16. Radius of gyration obtained from the unified model versus the ideal Zn deposition thickness in monolayers. The standard error (horizontal markers) was obtained from the scattering data reduced at 50%, 90%, and 130% of the ideal Zn thickness and from the model fit.

A sub-structure appeared within the scattering data after 2000 Zn monolayers of charge passed. Figure 5.17 plots the radius of gyration of the substructure, $R_{G,\mathrm{sub}}$, against the amount of charge passed in terms of Zn monolayers. The figure also shows the total standard error. For the substructure, the radius of gyration remained nearly constant between 7 to 8 nm. This suggests that a substructure developed between 1200 and 2000 Zn monolayers of charge passed and the size of this sub-structure remained constant despite continued deposition and growth of the main scattering entities.

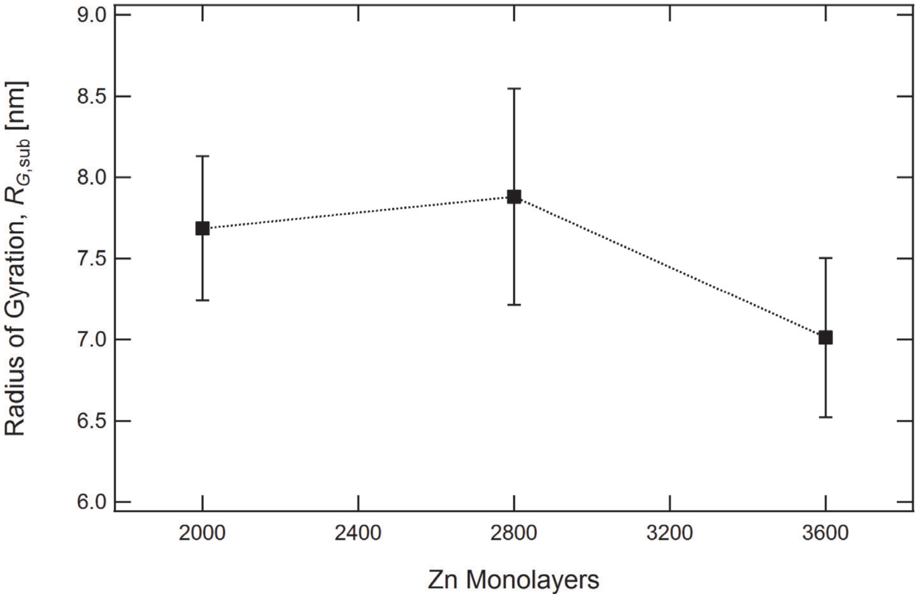

Figure 5.17. Radius of gyration for the sub-structure and the error obtained from the unified model versus the ideal Zn deposition thickness in monolayers. The standard error (horizontal markers) was obtained from the scattering data reduced at 50%, 90%, and 130% of the ideal Zn thickness and from the model fit.

5.3.5. Ex-Situ Electron Microscopy

A second Pt substrate sample underwent the same electrochemical Zn deposition procedure within the USAXS electrochemical cell for ex-situ SEM analysis. Figure 5.18 shows the resulting SEM image of the Zn morphology after 3600 Zn monolayers of charge passed. The amount of charge passed for the in-situ USAXS analysis was higher than investigated by in-situ AFM, however, the resulting Zn morphology was similar to that observed from in-situ AFM under similar conditions (refer to Figure 4.24). The Zn surface was largely dominated by Zn grains oriented at an angle in relation to the substrate. Individual Zn grains measure around 400 to 700 nm in size and they exhibit a layered structure. The 400 to 700 nm size of the Zn grains observed by ex-situ SEM analysis correlates well to the measured radius of gyration of 265 nm obtained from the scattering model.

As observed from the in-situ AFM analysis, the Zn grains exhibited a layered structure along the prism planes. From the SEM analysis, each layer within the Zn grains measured from 20 to 50 nm in thickness. It is hypothesized that the layered structure the Zn grains observed from the SEM analysis resulted in the sub-structure scatter that was observed from the USAXS analysis after 1200 Zn monolayers of charge passed.

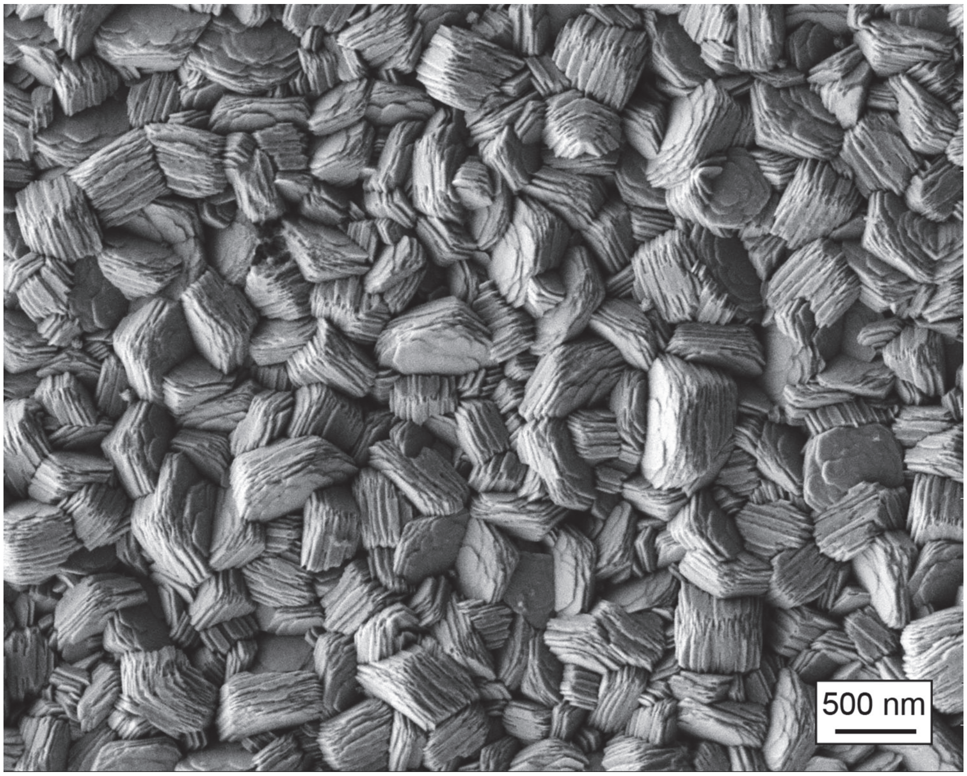

Figure 5.18. SEM image of the Zn deposition within 0.34 mol kg^{-1} $Zn(OTf)_2$/BMIm OTf at -700 mV versus Zn/Zn(II) for 3600 Zn monolayers.

5.4. Conclusions

- The calculated radius of gyration, R_G, obtained from the main Guinier region from the unified fit model to the scattering data increased with increasing Zn deposition. The increase in R_G was linearly dependent on the amount of charge passed (ideal Zn monolayers). The radius of gyration was around 73 nm after 400 Zn monolayers of charge passed and increased to 265 nm after 3600 Zn monolayers of charge passed.
- A substructure was observed in the scattering data after 2000 Zn monolayers of charge passed. This substructure exhibited a radius of gyration, $R_{G,\mathrm{sub}}$, between 7 to 8 nm. The radius of gyration for the substructure remained constant with increasing Zn deposition.

This points to a substructure that remains the same size despite the fact that the main scattering structure continued to increase in size with continued deposition.

- From the intensity decay within the Porod regime (P ≈ 3.5), the Zn/electrolyte interface exhibited a surface fractal structure. Furthermore, the interface structure remained constant throughout the Zn deposition from 400 to 3600 Zn monolayers of charge passed.
- Since the true thickness of the Zn deposition was unknown, the scattering intensity could not be correctly normalized. This puts a level of uncertainty on parameters that are dependent on intensity such as the volume of the scattering phase, surface area, and number of scatterers. General observations of the parameters, however, points to an increase in volume of the scattering phase with increase Zn deposition. Analysis of the scattering data also suggested that the number of scatterers decreased with continued deposition.

6. Intersections of the In-Situ Techniques

This investigation employed three different in-situ techniques to investigate the electrodeposition behavior of Zn within an ionic liquid electrolyte. From the electrochemical analysis, the system's degree of irreversibility was analyzed, diffusion coefficients were measured, and the nucleation behavior was analyzed. From the AFM analysis, zinc deposition morphologies were compared, crystal growth rates were measured, and the characteristic length (correlation length) of the Zn deposition was obtained. From the USASX investigation, the characteristic length (radius of gyration) of the Zn deposition was obtained, the hierarchical relation of the Zn deposition was analyzed, and the nature of the interface between the Zn and the electrolyte was investigated. Each of these investigations gave insight into the deposition behavior of Zn within an ionic liquid electrolyte. In addition, certain parameters can be compared between the in-situ techniques for verification and this chapter discusses these comparisons.

6.1. Nucleation Behavior

From the electrochemical analysis, deposition within 0.34 mol kg^{-1} $Zn(OTf)_2$ resulted in behavior that most closely follows instantaneous nucleation. Fitting the theoretical model relating the current density to time allowed for estimating the nucleation density that the system underwent during the initial deposition on the Pt substrate. The nucleation density is a parameter that can be measured by AFM. The Pt substrate used in this analysis was not smooth enough to allow for direct measurement of the nucleation density. The nucleation density, however, was inferred by analyzing the relation of the correlation length to the amount of charge passed and extrapolating back to a condition where zero charge was passed.

From the AFM data, the linear relation of correlation length as a function of the amount of charge passed was obtained up to 1200 Zn monolayers. By extrapolating back to 0 charge passed, one can infer the correlation length between the nucleation sites. Using this distance between nucleation sites, the estimate nucleation density was calculated. The estimated nucleation densities for the -500 mV and -650 mV depositions are:

- 0.34 mol kg^{-1} concentration at -500 mV → 4.2×10^{10} cm^{-2}
- 0.34 mol kg^{-1} concentration at -650 mV → 5.5×10^{10} cm^{-2}

Comparing these results to the nucleation densities obtained from the electrochemical analysis conducted in Chapter 3 for deposition within the 0.34 mol kg^{-1} Zn concentration (referring to Figure 3.15), the estimated nucleation densities from the potential step analysis were (values obtained from interpolating the best fit curve):

- Theoretically calculated at -500 mV → 1.1×10^{6} cm^{-2}
- Theoretically calculated at -650 mV → 4.5×10^{6} cm^{-2}

The theoretically calculated nucleation densities were over 4 magnitudes lower than what was extrapolated from the AFM data. Therefore, it appeared that the theoretical model for calculating the nucleation density from the current transient during a potential step deposition does not apply to this system since the difference between the values is too large to be explained by incorrect measurement of the diffusion coefficient or the Zn ionic concentration within the electrolyte. Therefore, the assumptions used to obtain the theoretical model may not apply for this system.

The model for calculating the nucleation density relies on the Avarmi equation and assumes that nucleation occurs randomly and homogeneously. In addition, the diffusion field was simplified to a linear diffusion model for developing the current transient model [31]. These assumptions may not be valid for the ionic liquid system. Furthermore, the discrepancy between the AFM analysis and the theoretical nucleation analysis also puts into question the validity of using this model to determine whether or not the nucleation behavior follows instantaneous behavior or progressive behavior.

6.2. Checking Normalization of Scattering Intensity

For the USAXS analysis, to correctly normalize the scattering intensity, $I(q)$, one needs to know the thickness of the sample. The USAXS experiment was conducted in-situ, therefore, the actual thickness of the deposition was unknown. For the reduction of the scattering data, it was assumed that the thickness measured by direct measurement from the AFM experiments also applied for the USAXS. This assumption, however, is broad since the USAXS analysis was conducted under different electrochemical conditions on a different substrate geometry and within a different electrochemical cell. One method of double checking the validity of the thickness used for data reduction is by double checking the consistency of the Porod invariant (refer to equation (5.18)) utilizing volume fraction, V_f, measured from the AFM analysis.

If the sample thickness is unknown, it can be inferred from using the Porod invariant described by equation (5.18). If the scattering data is reduced using a fixed scattering thickness, denoted as t_f, the normalized scattering intensity from the data reduction using a fixed thickness, $I_f(q)$, is related to the true intensity, $I(q)$, by

$$I(q) = I_f(q)\frac{t_f}{t_s} \tag{6.1}$$

where t_s is the true sample thickness. Combining equation (6.1) with equation (5.18) and substituting Q_P with $Q_{P,f}$ where the subscript f denotes that the Porod invariant was obtained using a fixed thickness, t_f, yields

$$Q_{P,f} = \left(2\pi^2|\Delta\rho|^2 V_f\right)\frac{t_s}{t_f} \tag{6.2}$$

Rearrangement of the equation and solving for the sample thickness, t_s, yields

$$t_s = \frac{Q_{P,f} t_f}{2\pi^2 |\Delta\rho|^2 V_f} \tag{6.3}$$

The volume fraction, V_f, is still an unknown quantity. The volume fraction, however, can be obtained from the in-situ AFM data presented in Chapter 4.

The volume fraction from the AFM analysis was calculated for the deposition at -650 mV versus Zn/Zn(II). This deposition was selected since the experimental parameters of potential and the electrolyte concentration most closely followed the deposition parameters conducted for the USAXS analysis. The volume fraction from the AFM analysis was obtained from the cumulative height distribution and the measured values for the volume fraction are listed in Table 6.1 where ϕ_{Zn} is the volume fraction of the Zn phase and V_f is the volume fraction for the system. The calculated V_f from the in-situ AFM experiment ranged from 0.209 to 0.250 with an average of 0.239.

The Porod invariant for the scattering intensity normalized using the fixed sample thickness, $Q_{P,f}$, was calculated for each USAXS scan. The scattering contrast, $|\Delta\rho|^2$, between the Zn and ionic liquid electrolyte was 1.9576×10^{23} cm^{-4} (calculated using the Scattering Contrast Calculator within the Irena package for Igor Pro [57]). Using the average V_f calculated from the AFM experiments, the sample thickness for each USAXS scan was calculated and the results are shown in Table 6.2 along with the comparison to the ideal Zn thickness.

From the AFM analysis, the deposition thickness was around 90% of the ideal Zn thickness for a given amount of charge. The calculated thickness from the scattering data was around 50% of the ideal Zn thickness. This value is still within reason and it confirms that the Zn deposition within the USAXS experiment was of comparable thickness to the AFM experiments. Furthermore, the assumption that the AFM thickness was similar to the USAXS thickness appeared valid for the data reduction.

Table 6.1. Zn phase fraction, ϕ_{Zn} , and corresponding volume fraction, V_f, obtained from the AFM data for deposition at -650 mV vs. Zn/Zn(II) within 0.34 mol kg^{-1} Zn(OTf)$_2$/BMIm OTf.

Zn Monolayers	$\boldsymbol{\phi_{Zn}}$	$\boldsymbol{V_f = \phi_{Zn}(1-\phi_{Zn})}$
400	0.297	0.209
800	0.366	0.232
1200	0.427	0.245
1600	0.410	0.249
2000	0.471	0.242
2400	0.513	0.250
2800	0.541	0.248
Average	**0.432**	**0.239**

Table 6.2. Calculated thickness, t_s, of the deposition for each USAXS scan using the volume fraction obtained from the AFM analysis. For comparison, the ideal Zn thickness is given that corresponds to the amount of charge passed.

USAXS Scan (Zn Monolayers)	$\boldsymbol{t_s}$ **(nm)**	**Ideal Zn Thickness (nm)**
400	52	99
1200	136	298
2000	240	495
2800	345	693
3600	655	891

6.3. Characteristic Length of the Zn Deposition

From the AFM analysis, the correlation length, L_x, of the deposition was obtained assuming the system follows Gaussian behavior and fitting equation (4.3) to the height difference correlated data. The correlation length is analogous to the characteristic length of the system. The correlation length is obtained from real space data and is the length at which the root mean square of the height difference saturates. From the USAXS analysis, the radius of gyration, R_G, was calculated from the scattering behavior of the Zn deposition. Within real space terms, the radius of gyration is the characteristic length of the spatial differences within the plane parallel to the substrate. The correlation length, L_x, is a characteristic length obtained from the height data along the z-axis. If the system exhibits morphologies that have a width to height aspect ratio of near one, then the values of L_x amd R_G should be similar.

Figure 6.1 compares the radius of gyration obtained from the USAXS experiment to the correlation length obtained from the AFM deposition undergoing deposition under similar parameters. The correlation lengths from the AFM experiment were from the deposition at -650 mV versus Zn/Zn(II) within an electrolyte of 0.34 mol kg^{-1} concentration. The radius of gyration values obtained from the USAXS experiment were from deposition at -700 mV versus Zn/Zn(II) within an electrolyte of 0.34 mol kg^{-1} concentration. The characteristic lengths obtained by the two in-situ techniques were similar as shown in Figure 6.1. The radius of gyration values obtained from the USAXS experiment were about 1.5 times the correlation length values obtained from the AFM experiment. The USAXS analysis was obtained from the scattering data from a large substrate surface area of 1.2 mm^2 and these results help confirm the results obtained from the AFM analysis.

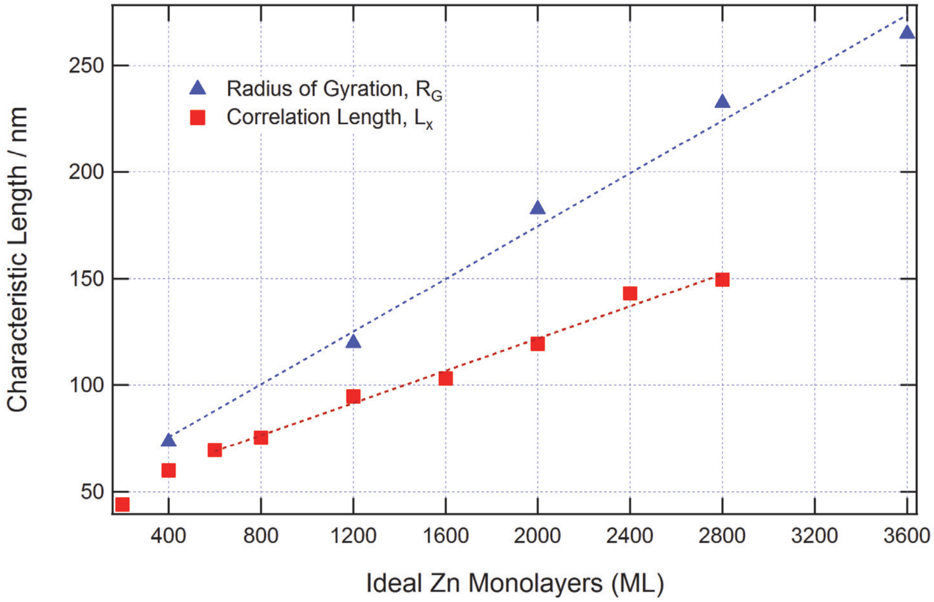

Figure 6.1. Characteristic length of the Zn deposition versus the amount of charge passed in terms of Zn monolayers. The correlation length is the characteristic length obtained from the AFM analysis and the radius of gyration is the characteristic length obtained from the USAXS analysis.

6.4. Identifying Sub-Structures within the Zn Deposition

From the USAXS analysis of the scattering data, a sub-structure developed within the Zn deposition between 1200 and 2000 Zn monolayers of charge passed. The size of this sub-structure remained constant despite the fact that the main scattering bodies continued to increase in size with continued deposition.

The USAXS analysis was conducted at -700 mV versus Zn/Zn(II) within 0.34 mol kg^{-1} $Zn(OTf)_2$/BMIm OTf. The calculated overpotential for Zn deposition within the USAXS trial was -530 ± 10 mV. The electrochemical parameters were closest to the AFM deposition trial at -650 mV versus Zn/Zn(II) within 0.34 mol kg^{-1} $Zn(OTf)_2$/BMIm OTf where Zn deposition was conducted at an overpotential of -520 ± 10 mV.

The evolution of the deposition morphology obtained from the AFM analysis at -650 mV versus Zn/Zn(II) is shown in Figure 6.2. From Chapter 4, this deposition was characterized by the domination of grains oriented with their basal plane at an angle in relation to the substrate. Growth was faster in the $\langle\bar{1}100\rangle$, $\langle\bar{1}\bar{1}20\rangle$, or $\langle 1\bar{2}10\rangle$ directions. Furthermore, the surface of the prism planes for the Zn grains started to exhibit a layered appearance by 1200 monolayers of charge passed. As deposition continued, this layered structure became more prominent and bulbous. By 2800 Zn monolayers of charge passed, each Zn grain exhibited a texture or sub-structure that resulted from the Zn layering. Furthermore, the size of the substructure appeared to not change with continued deposition and was measured to be between 40 to 50 nm between layers.

As observed from the USAXS analysis, the AFM morphology exhibited a hierarchical structure where the Zn grains exhibited a layered surface texture on the prism planes. The Zn grains continued to grow with increasing amounts of charge passed by adding Zn layers in the $\langle 0001\rangle$ direction, but the distance between the Zn layers that make up each grain remained the same. It is hypothesized that the sub-structure identified within the scattering data resulted from the development of the layered structure observed by the AFM.

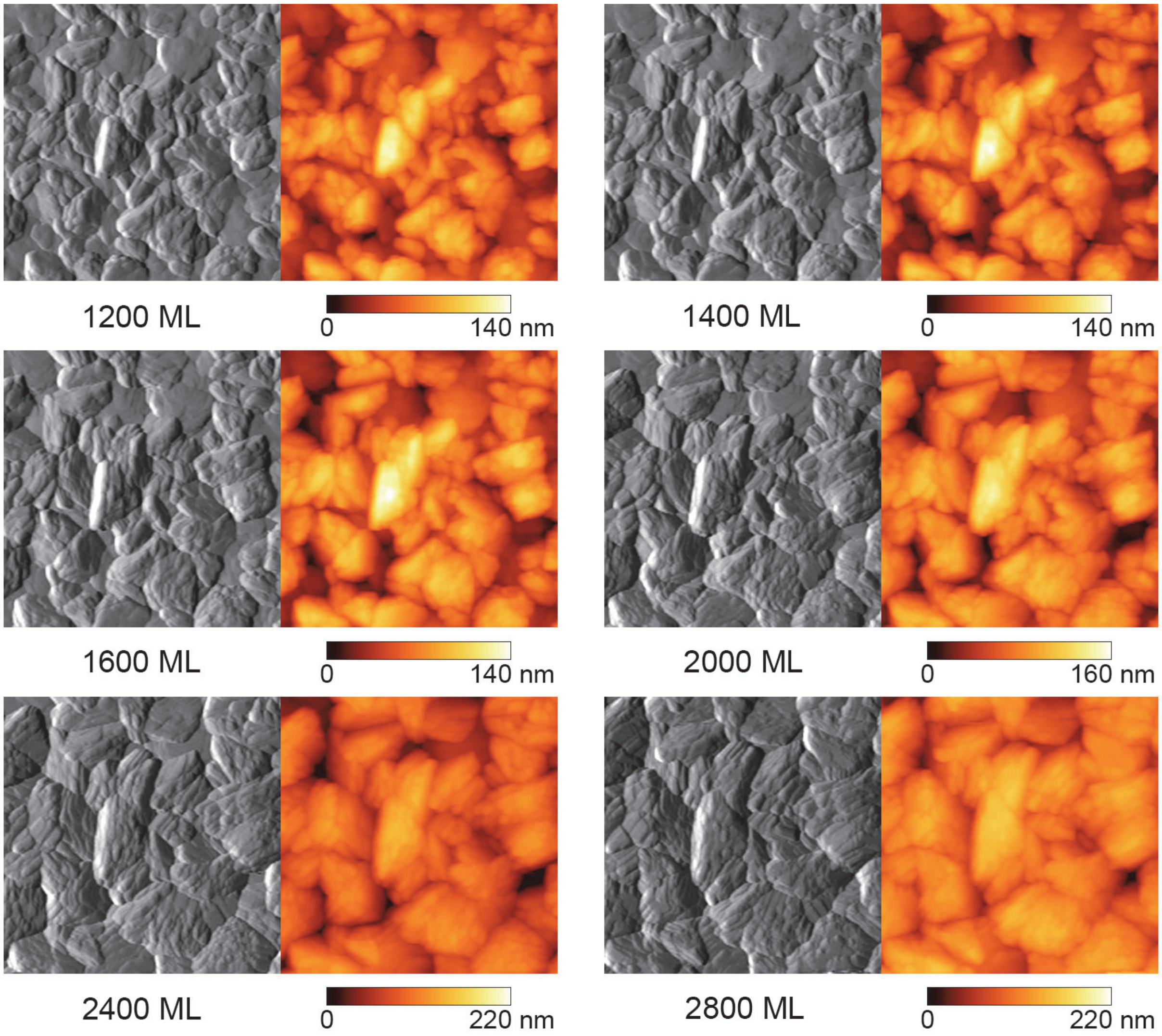

Figure 6.2. Deflection and corresponding height AFM images following the progression of Zn deposition morphology versus the amount of charge passed in terms of Zn monolayers (ML). Deposition was at -650 mV versus Zn/Zn(II) reference with an electrolyte concentration of 0.34 mol kg^{-1} $Zn(OTf)_2$/BMIm OTf. Images are 1.5 µm × 1.5 µm.

7. Summary and Conclusions

Zinc is an attractive material for chemical energy storage due to its non-toxicity, inexpensiveness, and recyclability. Flow batteries utilizing zinc for chemical energy storage have demonstrated the excellent energy storage capability of zinc. Outside of flow batteries, however, zinc has not been successfully used within a commercially available rechargeable battery system. The zinc electrode suffers from poor cyclability within conventional electrolyte systems.

From the electrochemical analysis it was observed that the electrodeposition of zinc within the ionic liquid electrolyte was highly irreversible. In addition, the total efficiency during cycling from zinc reduction to oxidation was around 90% for the electrolyte system containing 0.34 mol kg^{-1} $Zn(OTf)_2$. The cycling efficiency decreased with lower concentrations of $Zn(OTf)_2$. The diffusion coefficient at room temperature was measured to be 1.5×10^{-7} cm^2 s^{-1} and was within the range of similar investigations for imidazolium based ionic liquid electrolytes. In addition, the diffusion coefficient exhibited temperature dependent behavior. At a temperature of 55°C, the diffusion coefficient for zinc within the electrolyte was measured to be almost four times higher than at 25°C.

From the in-situ AFM analysis, three distinct morphological behaviors were observed. Deposition within an electrolyte with a the low concentration of 0.1 mol kg^{-1} at -430 mV versus Zn/Zn(II) resulted in a Zn deposition that was dominated by the growth of boulder like morphology. Deposition within an electrolyte at a high concentration was quickly dominated by favorably oriented Zn grains with continued deposition. Finally, deposition at the higher overpotentials of -600 mV versus Zn/Zn(II) within the 0.1 mol kg^{-1} concentration and -700 mV versus Zn/Zn(II) within the 0.34 mol kg^{-1} concentration resulted in surface instabilities that developed during Zn deposition. These surface instabilities consisted of agglomerate islands that grew rapidly during the first 600 to 800 Zn monolayers of charge passed.

From the height difference correlation analysis of the in-situ AFM data, the deposition within the 0.1 mol kg^{-1} concentration that resulted in boulder like morphology exhibited kinetic roughening behavior. The saturated surface roughness continuously increased with increasing Zn deposition. The local surface roughness, however, remained constant within increasing Zn deposition. In contrast, the deposition at -400 and -500 mV versus Zn/Zn(II) within the 0.34 mol kg^{-1} concentration quickly obtained a steady state behavior. From all the in-situ trials, the correlation length of the Zn deposition continued to increase with increasing amounts of charge passed (Zn monolayers).

From the in-situ USAXS analysis of Zn deposition, the characteristic length of the Zn deposition (radius of gyration) continued to increase with increasing Zn deposition. In addition, the Zn/electrolyte interface exhibited fractal like behavior. In addition, the structure of the Zn deposition became hierarchical after 1200 monolayers pointing to the development of a sub-structure with a characteristic length of between 7 to 8 nm and the characteristic length of the sub-structure remained constant with continued deposition.

The in-situ USAXS results helped confirm the results observed by the AFM analysis. The characteristic length of the Zn deposition measured by the two techniques showed similar behavior exhibiting a linear increase to the amount of charge passed. In addition, the USAXS analysis confirmed the development of a hierarchical deposition structure that developed within the Zn deposition morphology where a large, growing structure was accompanied by a stable sub-structure. This is probably the result of the how the favorably oriented grains quickly dominated the Zn deposition surface as observed by the AFM analysis.

The deposition within the low concentration of 0.1 mol kg^{-1} $Zn(OTf)_2$ appeared to follow kinetic roughening that has been observed with systems using conventional electrolytes [39, 44] and this behavior would probably result in the eventual formation detrimental morphologies with cycling. The deposition within the 0.34 mol kg^{-1} $Zn(OTf)_2$, however, exhibited steady state behavior after a maximum surface roughness was obtained.

Viewing these results with an eye towards applications within rechargeable batteries, it is promising that a steady state was obtained under certain deposition conditions. A major problem with the Zn electrode is its propensity of forming surface instabilities that manifest as detrimental morphologies (e.g. dendrites) and these morphologies lowered the cycling capability of the electrode. Currently, zinc based rechargeable battery systems with a non-stirred electrolyte achieves around 200 charge/discharge cycles prior to failure [7]. If the Zn/electrolyte interface can remain stable during electrodeposition (during the charging cycle), then it will allow for improved cycling performance. This improved cycling performance may allow a system with a non-stirred electrolyte to approach the cycling behavior obtained by Zn based flow battery systems which currently obtain a cycling performance of over 1000 cycles.

8. Future Work

This dissertation should be considered as a springboard for more extensive investigations of the zinc deposition within ionic liquid electrolytes. The fact that a steady-state deposition behavior was observed in this investigation is promising in terms of utilizing ionic liquid electrolytes for energy storage applications.

From the conclusions obtained from this investigation, the deposition behavior was influenced by the applied overpotential and the $Zn(OTf)_2$ concentration. Also, increasing the temperature of the system significantly increased the diffusion behavior of Zn(II) within the electrolyte. Furthermore, increasing the temperature lowered the overpotential required for zinc deposition. Obtaining a system with better diffusion properties and lower overpotential will significantly increase the performance of the electrolyte system for rechargeable battery applications. Conducting an in-situ investigation on the deposition morphology and investigating the influence of temperature will help bring about a better understanding of the zinc deposition process. It may also point to the beneficial applicability of temperature to rechargeable battery systems utilizing ionic liquid electrolytes.

The role of additives as well as impurities is also largely unknown on the behavior of metal deposition within ionic liquid electrolytes. Other investigations have shown beneficial results for the performance of other ionic liquid systems by utilizing additives [24, 26]. An exhaustive analysis on the effect of additives on the morphological behavior of the deposition, however, has not been conducted to date. In addition, ionic liquid systems inherently contain impurities. In addition, ionic liquid systems inherently contain impurities. The level of impurities can be lowered but removing these impurities becomes more and more expensive to obtain higher and higher purities. The effect of certain impurities on the deposition behavior, however, is unknown. Some impurities may result in poorly performing electrolyte but other impurities may help improve deposition behavior. Understanding the role of various impurities to the deposition behavior of metals will help bring about a more targeted purity levels required for various applications.

On the analysis side of investigating the metal deposition behavior within ionic liquid electrolyte systems, the ability to “see” the evolution of the deposition process within this investigation greatly helped gain insight on how the deposition process was influenced by the various deposition parameters. Other tools that are capable of in-situ analysis may help obtain a better picture of the deposition process. For instance, using optical methods to analyze the deposition behavior of metals within ionic liquid systems has inherent advantages over the in-situ techniques used in this investigation. The foremost benefit is that a series of optical images can be obtained instantaneously allowing for analysis of fast kinetics. In addition, optical methods such as optical interferometry have been used to understand the diffusion gradients that develop within aqueous electrolyte systems [59]. Interferometry could be used for the analysis of diffusion gradients within ionic liquid systems. Other optical techniques used in aqueous deposition analysis such as a Hele-Shaw cell [60] may also prove valuable tools for understanding metal deposition within ionic liquid systems.

Ionic liquid electrolytes may contain inherently beneficial properties for energy storage applications. The ability to conduct metal deposition in a controlled manner that eliminates the risk of developing surface instabilities would greatly help the development of an inexpensive and high performing battery system. A better understanding of the underlying mechanisms, however, is still required before these electrolyte systems can be used at their full performance capability and in-situ investigations like the investigations conducted within this research should help prove valuable to gaining insight into such underlying mechanisms in battery systems.

References

1. Chen, H.S., et al., *Progress in electrical energy storage system: A critical review.* Progress in Natural Science, 2009. **19**(3): p. 291-312.
2. Yang, Z.G., et al., *Enabling renewable energy-and the future grid-with advanced electricity storage.* JOM, 2010. **62**(9): p. 14-23.
3. Wadia, C., P. Albertus, and V. Srinivasan, *Resource constraints on the battery energy storage potential for grid and transportation applications.* Journal of Power Sources, 2011. **196**(3): p. 1593-1598.
4. Ito, Y., et al., *Zinc morphology in zinc-nickel flow assisted batteries and impact on performance.* Journal of Power Sources, 2011. **196**(4): p. 2340-2345.
5. McLarnon, F.R. and E.J. Cairns, *The secondary alkaline zinc electrode.* Journal of the Electrochemical Society, 1991. **138**(2): p. 645-664.
6. Dell, R.M., *Batteries - fifty years of materials development.* Solid State Ionics, 2000. **134**(1-2): p. 139-158.
7. Beck, F. and P. Ruetschi, *Rechargeable batteries with aqueous electrolytes.* Electrochimica Acta, 2000. **45**: p. 2467-2482.
8. Poa, S.P. and C.H. Wu, *Quantitative study of shape change in zinc secondary electrodes.* Journal of Applied Electrochemistry, 1978. **8**(5): p. 427-436.
9. Baugh, L.M. and A. Higginson, *Passivation of zinc in concentrated alkaline-solution. 1. Characteristics of active dissolution prior to passivation.* Electrochimica Acta, 1985. **30**(9): p. 1163-1172.
10. Horn, Q.C. and Y. Shao-Horn, *Morphology and spatial distribution of ZnO formed in discharged alkaline Zn/MnO2 AA cells.* Journal of the Electrochemical Society, 2003. **150**(5): p. A652-A658.
11. Naybour, R.D., *Morphologies of zinc electrodeposited from zinc-saturated aqueous alkaline solution.* Electrochimica Acta, 1968. **13**(4): p. 763-&.
12. Diggle, J.W., R.J. Frederic, and A.C. Reimschu, *Crystallographic and morphological studies of electrolytic zinc dendrites grown from alkaline zincate solutions.* Journal of Materials Science, 1973. **8**(1): p. 79-87.
13. Wang, R.Y., D.W. Kirk, and G.X. Zhang, *Effects of deposition conditions on the morphology of zinc deposits from alkaline zincate solutions.* Journal of the Electrochemical Society, 2006. **153**(5): p. C357-C364.
14. Gallaway, J.W., et al., *A lateral microfluidic cell for imaging electrodeposited zinc near the shorting condition.* Journal of the Electrochemical Society, 2010. **157**(12): p. A1279-A1286.
15. Lopez, C.M. and K.S. Choi, *Electrochemical synthesis of dendritic zinc films composed of systematically varying motif crystals.* Langmuir, 2006. **22**(25): p. 10625-10629.

16. Keist, J., et al., *Real-time dynamics during recharging cycles*, in *Pacific Rim Meeting on Electrochemical and Solid-State Science*, R. Kostecki, T. Abe, and B. Liaw, Editors. 2012, The Electrochemical Society: Honolulu, Hawaii. p. 13-17.

17. Bockris, J.O.M., Z. Nagy, and D. Drazic, *On the morphology of zinc electrodeposition from alkaline solutions.* Journal of the Electrochemical Society, 1973. **120**(1): p. 30-41.

18. Pal, B.N. and D. Chakravorty, *Pattern formation of zinc nanoparticles in silica film by electrodeposition.* Journal of Physical Chemistry B, 2006. **110**(42): p. 20917-21.

19. Castner, E.W. and J.F. Wishart, *Spotlight on ionic liquids.* Journal of Chemical Physics, 2010. **132**(12).

20. Endres, F. and S.Z. El Abedin, *Air and water stable ionic liquids in physical chemistry.* Physical Chemistry Chemical Physics, 2006. **8**(18): p. 2101-2116.

21. Galinski, M., A. Lewandowski, and I. Stepniak, *Ionic liquids as electrolytes.* Electrochimica Acta, 2006. **51**(26): p. 5567-5580.

22. Endres, F., et al., *Electrodeposition from Ionic Liquids*. 2008: Wiley.

23. Gnahm, M. and D.M. Kolb, *The purification of an ionic liquid.* Journal of Electroanalytical Chemistry, 2011. **651**(2): p. 250-252.

24. Abbott, A.P., et al., *The effect of additives on zinc electrodeposition from deep eutectic solvents.* Electrochimica Acta, 2011. **56**(14): p. 5272-5279.

25. Ho, C.C., J.W. Evans, and P.K. Wright, *Direct write dispenser printing of a zinc microbattery with an ionic liquid gel electrolyte.* Journal of Micromechanics and Microengineering, 2010. **20**(10).

26. Abbott, A.P., J.C. Barron, and K.S. Ryder, *Electrolytic deposition of Zn coatings from ionic liquids based on choline chloride.* Transactions of the Institute of Metal Finishing, 2009. **87**(4): p. 201-207.

27. Gou, S.-P. and I.W. Sun, *Electrodeposition behavior of nickel and nickel–zinc alloys from the zinc chloride-1-ethyl-3-methylimidazolium chloride low temperature molten salt.* Electrochimica Acta, 2008. **53**(5): p. 2538-2544.

28. Ispas, A., et al., *Electrochemical deposition of silver from 1-ethyl-3-methylimidazolium trifluoromethanesulfonate.* Electrochimica Acta, 2011. **56**(28): p. 10332-10339.

29. Bard, A.J. and L.R. Faulkner, *Electrochemical Methods: Fundamentals and Applications*. 2000: Wiley.

30. Aoki, K. and J. Osteryoung, *Diffusion-controlled current at the stationary finite disk electrode: Theory.* Journal of Electroanalytical Chemistry and Interfacial Electrochemistry, 1981. **122**(0): p. 19-35.

31. Scharifker, B. and G. Hills, *Theoretical and experimental studies of multiple nucleation.* Electrochimica Acta, 1983. **28**(7): p. 879-889.

32. Pitner, W.R. and C.L. Hussey, *Electrodeposition of zinc from the Lewis acidic aluminum chloride-1-methyl-3-ethylimidazolium chloride room temperature molten salt.* Journal of the Electrochemical Society, 1997. **144**(9): p. 3095-3103.

33. Roušar, I., K. Micka, and A. Kimla, *Electrochemical Engineering*. 1986: Elsevier.

34. McBreen, J. and E.J. Cairns, *The Zinc Electrode, in: Advances in Electrochemistry and Electrochemical Engineering*, ed. H. Gerischer and C.W. Tobias. Vol. 11. 1978, New York, New York: Willey.

35. Fannin, A.A., et al., *Properties of 1,3-dialkylimidazolium chloride aluminum-chloride ionic liquids. 2. Phase-transitions, densities, electrical conductivities, and viscosities.* Journal of Physical Chemistry, 1984. **88**(12): p. 2614-2621.

36. Moshtev, R.V. and P. Zlatilova, *Kinetics of growth of zinc dendrite precursors in zincate solutions.* Journal of Applied Electrochemistry, 1978. **8**: p. 213-222.

37. Zhu, Y.L., et al., *Electrochemical behavior of Ni(II)/Ni in a hydrophobic amide-type room-temperature ionic liquid.* Electrochimica Acta, 2009. **54**(28): p. 7502-7506.

38. Eaton, P. and P. West, *Atomic Force Microscopy*. 2010: Oxford University Press.

39. Meakin, P., *Fractals, Scaling and Growth Far from Equilibrium*. 1997: Cambridge University Press.

40. Tong, W.M. and R.S. Williams, *Kinetics of surface growth - phenomenology, scaling, and mechanisms of smoothening and roughening.* Annual Review of Physical Chemistry, 1994. **45**: p. 401-438.

41. Schug, C., et al., *Surface roughness of sputter-deposited gold films: a combined X-ray technique and AFM study.* Surface and Interface Analysis, 1999. **27**(7): p. 670-677.

42. Huo, S. and W. Schwarzacher, *Anomalous scaling of the surface width during Cu electrodeposition.* Physical Review Letters, 2001. **86**(2): p. 256-259.

43. Guo, L., et al., *Island growth in electrodeposition.* Journal of Physics D-Applied Physics, 2011. **44**(44).

44. Iwamoto, A., T. Yoshinobu, and H. Iwasaki, *Stable growth and kinetic roughening in electrochemical deposition.* Physical Review Letters, 1994. **72**(25): p. 4025-4028.

45. Nečas, D. and P. Klapetek, *Gwyddion: an open-source software for SPM data analysis.* Central European Journal of Physics, 2012. **10**(1): p. 181-188.

46. Keist, J., et al., *In-situ investigation of Zn depostion within KOH using small-angle scattering and atomic force microscopy*, in *To Be Submitted: Journal of Applied Crystallography*. 2013.

47. Bonse, U. and M. Hart, *Tailless X-ray single-crystal reflection curves obtained by multiple reflection - (Si Ge crystals - E/T).* Applied Physics Letters, 1965. **7**(9): p. 238-&.

48. Guinier, A., *The diffusion of x-rays under the extremely weak angles applied to the study of fine particles and colloidal suspension.* Comptes Rendus Hebdomadaires Des Seances De L Academie Des Sciences, 1938. **206**: p. 1374-1376.

49. Porod, G., *X-ray low angle scattering of dense colloid systems.* Kolloid-Zeitschrift und Zeitschrift fuer Polymere, 1953. **133**: p. 51.

50. Ilavsky, J., et al., *Ultra-small-angle X-ray scattering at the Advanced Photon Source.* Journal of Applied Crystallography, 2009. **42**: p. 469-479.

51. Brumberger, H., *Modern Aspects of Small-Angle Scattering*. 1994: Springer.

52. Beaucage, G., *Small-angle scattering from polymeric mass fractals of arbitrary mass-fractal dimension.* Journal of Applied Crystallography, 1996. **29**: p. 134-146.

53. Beaucage, G., *Approximations leading to a unified exponential/power-law approach to small-angle scattering.* Journal of Applied Crystallography, 1995. **28**(6): p. 717-728.

54. El-Dasher, B., S. Torres, and J. Ilavsky, *Design of an electrochemical cell for in-situ analysis by ultra-small-angle X-ray scattering.* To Be Submitted: Journal of the Electrochemical Society, 2013.

55. Ilavsky, J., et al., *Ultra-small-angle X-ray scattering instrument at the Advanced Photon Source: History, recent development, and current status.* Metallurgical and Materials Transactions a-Physical Metallurgy and Materials Science, 2013. **44A**(1): p. 68-76.

56. Ilavsky, J., et al., *High-energy ultra-small-angle X-ray scattering instrument at the Advanced Photon Source.* Journal of Applied Crystallography, 2012. **45**: p. 1318-1320.

57. Ilavsky, J. and P.R. Jemian, *Irena: tool suite for modeling and analysis of small-angle scattering.* Journal of Applied Crystallography, 2009. **42**: p. 347-353.

58. Swanson, H.E. and S. United, *Standard X-ray Diffraction Powder Patterns*. 1953, Washington, DC: U.S. Dept. of Commerce, National Bureau of Standards.

59. Léger, C., J. Elezgaray, and F. Argoul, *Probing interfacial dynamics by phase-shift interferometry in thin cell electrodeposition.* Journal of Electroanalytical Chemistry, 2000. **486**(2): p. 204-219.

60. Garik, P., et al., *Laplace-field-controlled and diffusion-field-controlled growth in electrochemical deposition.* Physical Review Letters, 1989. **62**(23): p. 2703-2706.